A Geochemical Study of the Mineralization at the Hopper Property, Yukon: A Case Study of an Atypical Copper Occurrence

by

Vered H. Blumenthal

A thesis
presented to the University of Waterloo
in fulfillment of the
thesis requirement for the degree of
Master of Science
in
Earth Sciences

Waterloo, Ontario, Canada, 2010

AUTHOR'S DECLARATION

I hereby declare that I am the sole author of this thesis. This is a true copy of the thesis, including any required final revisions, as accepted by my examiners.

I understand that my thesis may be made electronically available to the public.

Abstract

The Hopper property is located in the Yukon Tanana terrane in the southwestern Yukon. It is characterized by granodiorite-hosted copper and molybdenum mineralization that is related to propylitic alteration and shearing. The focus of this study is to develop a genetic model for the copper mineralization based on field, petrographic and geochemical analyses.

The mineralization zone is roughly 500 m long and 20 m wide and is hosted in a granodiorite of calc-alkaline affinity interpreted to be part of the Ruby Range batholith which intruded the Aishihik metamorphic suite. The intrusion took place during the late Cretaceous based on U and Pb analyses of zircons with laser ablation inductively-coupled plasma mass spectrometer, placing it in the same time frame as the intrusion hosting the Casino mineralization, the largest porphyry copper deposit in the Yukon. The mineralization consists of chalcopyrite and molybdenite found along fractures, as disseminations and on shearing surfaces. Sulphur isotopes from chalcopyrite and pyrite range from

-1.7 to -0.8 per mil suggesting it is ortho-magmatic in origin.

The chemical compositions of biotite and amphibole of the Hopper intrusion resemble mineral chemistry of known porphyry systems. Biotites from both Hopper and Casino exhibit Mg-Cl avoidance and have similar values of MnO, TiO_2, Al_2O_3, BaO, Na_2O and K_2O, and amphiboles range in composition between magnesio-hornblende and actinolite, similar to other porphyry copper type deposits.

There are two distinct populations of titanite in the Hopper intrusion, magmatic and hydrothermal. Magmatic titanites are euhedral and are in sharp, planar contact with other magmatic phases, whereas hydrothermal titanites are anhedral and are associated with alteration minerals and the mineralization. Both populations show substitution between Ti and Al+Fe+Nb+Zr+Ce+Y. The hydrothermal titanites are richer in Ti, Cu, and Cr compared to the magmatic ones that are more enriched in Mo suggesting the mineralization is ortho-magmatic in origin.

Sulphur isotopes analyses suggest Hopper could be a porphyry type mineralization. However, the mineralization was also found to be related with propylitic alteration, shearing and depletion in Si and K, indicating this is not a typical system. Therefore, two possible models can explain the copper occurrence at Hopper. According to the first model, the mineralization is ortho-magmatic and is part of a porphyry system, but it has been remobilized to the propylitic zone. A second model is that the mineralization is much younger than the intrusion and is related to shearing.

Acknowledgements

Table of Contents

List of Figures

List of Tables

Chapter 1
Introduction

1.1 General introduction

The Hopper property is located in southwestern Yukon, east of Aishihik and Hopkins lakes, in the Yukon Tanana terrane. Copper and molybdenum mineralization at the property was emplaced in a granodiorite that intruded into the metasedimentary rocks of the Aishihik metamorphic suite.

Most of the copper in the Yukon occurs in skarn and porphyry copper deposits. Skarn copper deposits are of Cretaceous age and are part of the Whitehorse copper belt from which the majority of the copper in the Yukon has historically been produced. Copper is also found in porphyry type deposits of Jurassic and Cretaceous ages, mostly in the Dawson Range in central Yukon and in the Carmacks copper belt (Selby and Nesbitt, 2000, Tafti and Mortensen, 2003 and Yukon Geological Survey, 2007). Minto, an operating mine with 1.81% grade copper, 0.57 gram/ton gold and 7.6 gram/ton silver, and Williams Creek deposit, a deposit with 1% copper, are examples of porphyry copper deposits of Jurassic age. Casino is the largest porphyry copper deposit in the Yukon with 675 million tones of 0.25% copper, 0.48 gram/ton gold and 0.024% molybdenum, and is Cretaceous in age (Selby and Nesbitt, 2000). Copper is also found in the Yukon in the form of VMS deposits, PGE deposits and in iron-oxide-copper gold deposits (Yukon Geological Survey, 2007).

The copper mineralization at the Hopper property appears to have a porphyry-type affinity. However, it is associated with a shear zone and propylitic alteration unlike other typical copper porphyry-type deposits which are normally characterized by feldspathic alteration in the core followed by propylitic and argillic alteration zones (Gustafson and Hunt, 1975). This raises the question whether or not the mineralization is ortho-magmatic in origin, i.e., whether or not this is a true porphyry system. The purpose of this study is to gain a better understanding of the nature of the copper mineralization at the Hopper property and to offer a genetic model for its occurrence.

1.2 Thesis objectives

The purpose of this study is to attain a better understanding of the copper occurrence at the Hopper property and to answer the question whether the mineralization is originated from magmatic fluids or

not. In order to develop a petrogenetic model for the mineralization and its controls, a few objectives were set:

1. Characterize the mineralization and the associated alteration spatially and petrographically.
2. Perform a mass balance analysis to compare between altered and least altered host rock for the mineralization
3. Study the magmatic minerals of the Hopper intrusion and the alteration minerals associated with the mineralization.
4. Characterize the fluids that emplaced the copper mineralization by analyzing the mineralization for S isotopes.
5. Age date the intrusion with titanites and zircons using U-Pb to characterize the age of the intrusion and the associated mineralization.

1.3 Thesis organization

This thesis contains five chapters. The first chapter is an introduction that presents background information and the objectives of this study, and chapters 2-4 address these goals. Chapters 2 and 4 are written as independent papers, each of them including overview, introduction, results, discussion, and conclusions. As such, some repetition of the background material is present. Chapter 3 presents the chemistry of minerals from the Hopper intrusion in comparison with other porphyry systems and chapter 5 presents the conclusions of this study. Appendices B to J are located in the back pocket CD and can be requested digitally by contacting the author at vhblumen@sciborg.uwaterloo.ca.

1.4 Previous work

The Hopper property has been explored since 1907. More recent sampling and data collection were completed by Mitsubishi Metal Mining Co in 1968 followed by exploration conducted in 1977 by Whitehorse Copper Mines Ltd. A soil sample survey of the Hopper property in 1968 by Mitsubishi yielded values of up to 660 ppm Cu. Diamond drill cores by Whitehorse Copper Mines in 1977 intersected an adjacent skarn occurrence which contained 1.94% copper over 18.59 m and 2.23% Cu over 6.48 m (Smith, 2007). Since 2006, Archer Cathro and Associates and Strategic Metals Ltd. have been exploring the property owned by Strategic Metals Ltd. Soil samples collected by Strategic Metals Ltd. in 2006 yielded copper anomalies between 500 and 1275 ppm in an area of 800 m long and 250 m wide. The highest value of copper obtained from a soil sample was 2810 ppm copper (Smith, 2007). Grab samples of rocks from the intrusion had copper values between 0.11 wt. % and

1.52 wt. %. The soil samples also yielded molybdenum values up to 95 ppm, zinc values of up to 296 ppm, lead values up to 37 ppm and gold values up to 465 ppb (Smith, 2007).

The area has been studied since the early 1900's. This region was initially mapped by Cockfield in 1927 (Mezger, 1997). Overviews of the geology of the Yukon including the area of the Hopper property are given by Templeman-Kluit (1981) and Wheeler and McFeely who published a map of the tectonic settings of the Canadian Cordillera in 1991. Studies about the metamorphic assemblages and the tectonic evolution of the area were published by Erdmer and Mortensen (1993), Johnston and Erdmer (1995), and Johnston et al. (1996). Johnston also wrote his PhD thesis about the geological evolution of the area in 1993. Mezger published studies and a PhD thesis about the metamorphic assemblages in the region in 1997 and recent mapping of the region was completed by Johnston and Timmerman in 1997.

1.5 Site description

The Hopper property owned by Strategic Metals Ltd. is located approximately 180 km northwest of Whitehorse, Yukon, in the Yukon Tanana terrane, 52 km north of the Otter Falls cutoff along the Ashihik Lake road. The property lies between 1000 and 1645 masl (meters above sea level) within the Kluane plateau and is characterized by subalpine vegetation. Below 500 m, glacial features such as small eskers, kames, kettles and assorted till deposits can be found (Smith, 2007).

The study was focused on the upperlands (above the 800 m level) where buckbrush cover, knolls, swamps and small lakes are common. A steep 30º slope separates the upper and lower land. Outcrops are located mostly on hilltops and along the slope (Smith, 2007).

1.6 Regional geology

The Hopper property is located in the Yukon Tanana Terrane between the Denali fault and the Tintina fault in southwest Yukon (Figure 1.1).

3
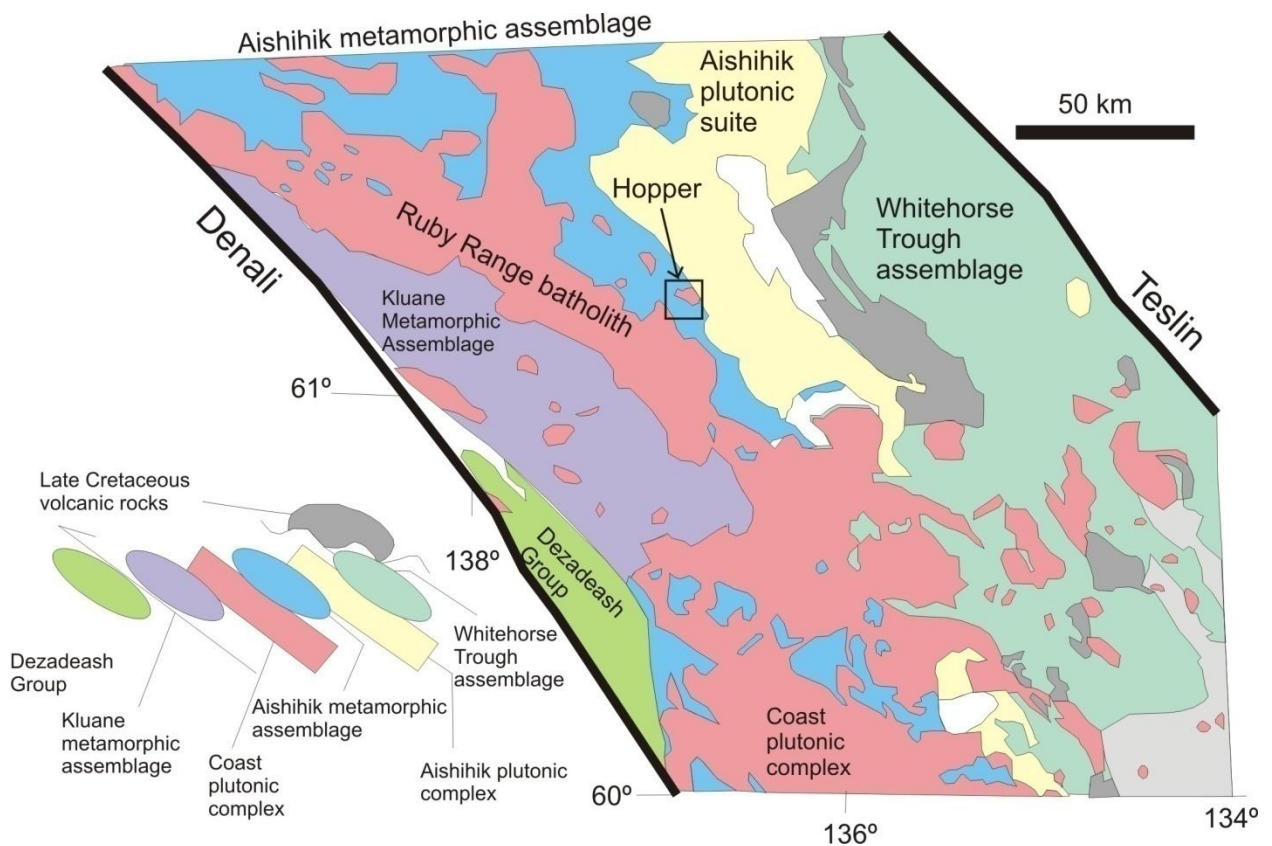
Figure 1.1: Regional geology map of southwest Yukon (modified from Johnston and Canil, 2007). The Hopper property consists of granodiorite interpreted to be part of the Ruby Range batholith which intruded the Aishihik metamorphic suite.

Yukon Tanana, the largest terrane in the Yukon, is a pericratonic terrane located in most of central and western Yukon and east central Alaska between the Denali and the Tintina faults in the northern Cordillera. The Yukon Tanana terrane surrounds Stikinia terrane, both of which make up the western part of the Intermontane belt (Mortensen, 1992, Colpron et al., 2006 and Johnston and Canil, 2007).

The Yukon Tanana terrane has been a source of confusion due to overprinting younger deformation and magmatic events, a lack of geochronological data and detailed mapping, poor exposure and numerous changes in nomenclature (Mortensen, 1992, Colpron, 2006). Therefore, Colpron et al. (2006) suggest a new tectonostratigraphic framework for the pericratonic terranes based on detailed mapping done as part of the Ancient Pacific Margin NATMAP (national mapping program) project.

Based on this project, the Yukon Tanana terrane has been divided into four assemblages according to their age, stratigraphic units and their depositional environments. These assemblages from oldest to

4

youngest are the Snowcap assemblage, the Finlayson assemblage, the Klinkit assemblage and the Klondike assemblage (Figure 1.2).
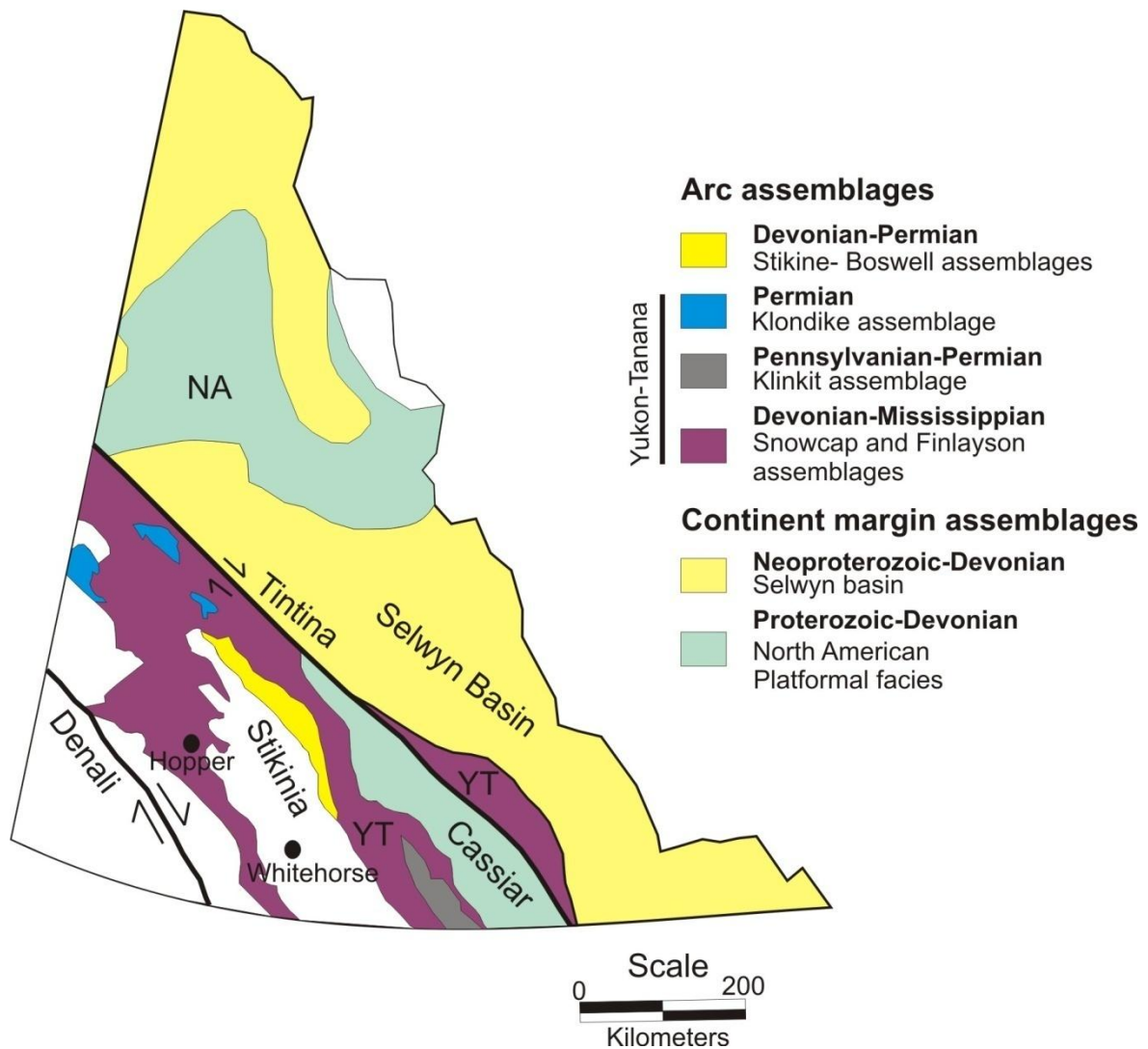
Figure 1.2: A regional geological map of assemblages of the Yukon Tanana terrane in the Yukon (modified from Colpron et al., 2006).

The Snowcap assemblage is characterized by mostly quartzite, pelitic and calc-silicate schists, marble, amphibolite and ultramafic rocks ranging in age between pre-late Devonian to late Devonian-early Mississippian. It is the oldest unit that comprises the basement of the Yukon Tanana terrane. The Hopper property consists of the Aishihik metamorphic suite that is part the Nisling assemblage, interpreted to be equivalent to the Snowcap assemblage (Colpron et al., 2006 and Johnston and Canil,

5

2007). The Nisling assemblage is characterized by mainly quartzofelspathic metasediments and minor chloritic schist, metagabbro and marble (Mortensen, 1992).

The upper Devonian to lower Mississippian age Finlayson assemblage lies on top of the Snowcap assemblage and consists of carbonaceous metasedimentary rocks, quartz-muscovite schist, and minor mafic metavolcanic, metagabbro, marble and pebble conglomerate. The Finlayson assemblage includes the Nasina assemblage that overlies the Nisling assemblage in the Aishihik metamorphic suite (Mortensen, 1992, Colpron et al., 2006, Johnston and Canil, 2007). Metaigneous rocks of the Nasina assemblage crystallized during the Mississippian between 351.5±2.0 and 343.8±0.8 Ma (Johnston et al., 1996).

The Klinkit assemblage, of middle Mississippian to early Permian age, includes intermediate to mafic volcaniclastic and volcanic rocks as well as limestone. This assemblage is less deformed and metamorphosed than the Snowcap and Finlayson assemblages. The mid to late Permian age Klondike assemblage includes calc-alkaline felsic rocks and minor mafic metavolcanic rocks interpreted to be a result of subduction.

These assemblages were followed by deposition of late Triassic clastic rocks including siltstone and shale and fragments of ultramafic rocks and metamorphic rocks from earlier units. Mafic and intermediate plutons of early Jurassic age and late Cretaceous quartz monzonite then intruded during the Mesozoic. During the late Cretaceous and/or early Tertiary periods volcanic flows and volcaniclastic rocks were deposited (Mortensen, 1992).

The main deformation in the Yukon Tanana terrane is a subhorizontally dipping foliation parallel to the compositional layering followed by thrust faulting events which occurred between late Triassic and mid Cretaceous times (Mortensen, 1992).

Chapter 2

Geochemical Analyses and Mass Balance Calculations of the Copper Mineralization at the Hopper Property, Yukon

2.1 Overview

The Hopper property in southwest Yukon is suspected to be a porphyry-style of mineralization similar to many other large copper occurrences in the Yukon. However, due to its association with a shear zone and propylitic alteration, the mineralization is potentially explained by a different model. The focus of this study is to develop a genetic model for the copper mineralization found in the Hopper property, based on field and petrographic observations as well as whole-rock geochemical and sulphur, uranium and lead isotopic analyses.

The main zone of mineralization at surface is roughly 500 m long and 20 m wide and is hosted in a granodiorite of calc-alkaline affinity, interpreted to be part of the Ruby Range batholith. The granodiorite intruded the Aishihik metamorphic suite and it is cut by younger mafic and felsic dykes. The mineralization consists of chalcopyrite and molybdenite. The mineralization occurs along fractures, as disseminations, and on shearing surfaces. Sulphur isotopes from chalcopyrite and pyrite range from -1.7 to -0.8 per mil and are similar to sulphur isotopes from skarn samples collected from an adjacent property. This suggests they are both likely to be of ortho-magmatic in origin. The mineralization at Hopper is associated with a propylitic alteration assemblage of chlorite, epidote-clinozoisite, carbonate and titanite. Forty three least altered and altered granodiorite samples were selected for whole rock analysis and mass balance calculations based on Gresens' and Grant's methods. Both methods show that altered granodiorite has lost SiO_2, Na_2O, K_2O, Ba, Rb, and Cr, and gained in addition to Cu and Mo, FeO, Fe_2O_3, MgO, and CaO, and V.

2.2 Introduction

The Yukon has been explored for precious metals such as gold and silver since the Klondike rush. A later exploration boom started with the development of the Alaska Highway, which allowed more accessibility to the region (Tempelman-Kluit, 1981). Copper is found in the Whitehorse trough, the Carmacks formations and the Dawson Range in different types of occurrences such as porphyry copper, skarn, and volcanogenic massive sulphide deposits, however the majority of copper in the

Yukon is found in porphyry copper deposits such as the Casino, Cash and Mt. Nansen porphyry deposits (Selby and Nesbitt, 2000). Minto is an operating copper and gold mine with 9 million tonnes ore of 1.73% copper grade that is likely porphyry related, although the origin for the Minto deposit is controversial (Tafti and Mortensen, 2003). The copper occurrence at the Hopper property is located roughly 200 km south of Casino porphyry copper deposit and 180 km northwest of Whitehorse. It has been suspected to be a porphyry type occurrence due to its location and style of mineralization, however, field work, petrographic analysis and mass balance calculations suggest differently. The purpose of this study is to develop a model for the granodiorite-hosted copper occurrence in the Hopper property and to answer the question whether or not the mineralization is a porphyry type mineralization, i.e a true ortho-magmatic model.

2.3 Local geology

The Hopper property contains copper and molybdenum mineralization that is hosted by granodiorite. The Hopper intrusion is interpreted by Johnston and Timmerman (1997) to be part of the Ruby Range batholith of the northern section of the coast plutonic complex (Figure 1.1). The granodiorite intruded the Aishihik metamorphic suite in the Yukon Tanana terrane. The Aishihik metamorphic suite is located west and north of the Aishihik batholith and east of the Ruby Range batholith.

The Aishihik metamorphic suite can be divided into lower and upper units. The lower unit of the suite is affiliated with the Snowcap assemblage previously named the Nisling assemblage and the upper unit is affiliated with the Finlayson assemblage previously named the Nasina assemblage (Mortensen 1992, Johnston et al., 1996 and Johnston and Canil, 2007). The transition between the two represents a shift in the depositional settings (Johnston et al., 1996).

The lower unit of the Snowcap assemblage consists mostly of quartzofeldspathic mica schist. It occurs as a continuous layer tens of meters thick and as discontinuous layers surrounded by quartzite that is generally micaceous. The unit also consists of marble horizons that vary in thickness and length. Interfoliated with the marble and mica schist is gneissic metagabbro. Another metaigneous rock in the Snowcap assemblage is metabasite.

The upper unit, the Finlayson assemblage, consists of a thick layer of marble interfoliated with metabasite. This unit becomes skarn adjacent to quartz feldspar porphyry dykes (QFP). Some of the skarn contains chalcopyrite and pyrite mineralization (Johnston, 1993). Other rock types related to this unit are biotite amphibolite schist, amphibolite and calc-silicate gneiss. A tan brown to black

carbonaceous and feldspathic quartzite and a quartzite mica schist with discontinuous lenses of marble and calc silicate lies above the thick layer of interfoliated marble and metabasite. The quartzite has color banding, graphitic and micaceous horizons and discontinuous lenses of marble and calc-silicate schist. The quartzite is interfoliated with metafelsite, metabasite, granite and diorite gneisses and schist (Johnston, 1993 and Johnston et al., 1996). Deformation and metamorphism mask primary stratigraphic relations. The metasediments at the Hopper property belong to the quartzite unit of the Finlayson assemblage based on similar lithologies. These metasediments consist of brown quartzite (Figure 2.1) dipping sub-horizontally to the north east as well as discontinuous lenses of marble and skarn.

Figure 2.1: Brown feldspathic quartzite of the Finlayson assemblage, part of the Aishihik metamorphic suite at the Hopper property.

The Aishihik metamorphic suite is cut by several intrusive events. During the Jurassic, the Aishihik batholith and plutonic suite composed of mostly granodiorite or quartz monzodiorite intruded at 186±2.8 Ma, followed by pink quartz monzonite of the Long Lake plutonic Suite at 185.6 +2.0/-2.4 Ma (Johnston et al., 1996). During the Cretaceous and Tertiary, volcanic rocks of the Carmacks group, the Ruby Range plutonic suite, plutons and dykes of the Nisling range alaskite and mount Creedon volcanic suite intruded the Aishihik metamorphic suite (Johnston et al., 1996).

9

The Hopper intrusion is granodiorite and diorite in composition and is interpreted to be part of the Ruby Range batholith, a 250 km long northeast dipping sill (Erdmer and Mortensen, 1993). The granodiorite is intruded by younger QFP and mafic and felsic dykes (Figure 2.2 and Figure 2.3). The age of the Hopper intrusion ranges between 76.0±1.1 Ma and 83.7±1.9 Ma based on U/Pb ratios in zircon. These ages are similar to ages found by Johnston (1993), where the margins of the north part of the Ruby Range batholith are 68-78 Ma, the south part of the batholith range between 69 Ma and 90 Ma and the core is 55.8±0.7 Ma based on U/Pb ratios in zircon. A geological map of the Hopper property is shown in Figure 2.3.
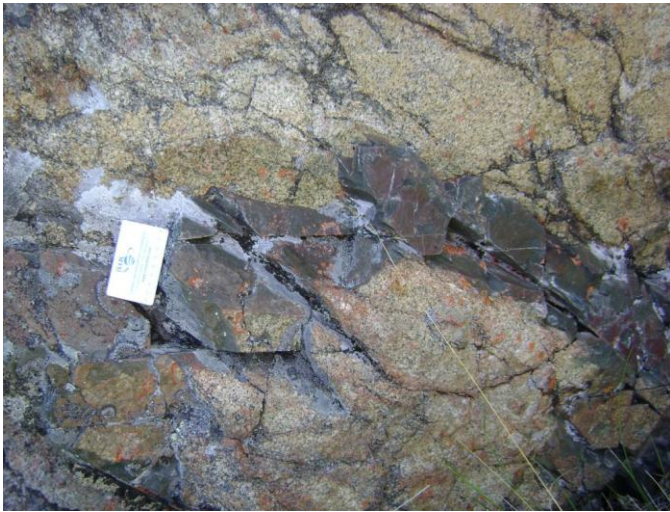
Figure 2.2: A mafic dyke cross cutting the Hopper granodiorite intrusion.

Figure 2.3: Geological map of the Hopper property (modified after Johnston and Timmerman, 1997). The property includes an intrusion of granodiorite composition (in pink) interpreted to

be part of the Ruby Range batholith. In the east part of the property the intrusion is of more dioritic composition. This granodiorite intruded the Aishihik metamorphic suite (in brown) which strikes northwest and dips subhorizontally to the east. The granodiorite and Aishihik metamorphic suite were both intruded by quartz feldspar porphyry dykes (QFP), and aplite and mafic dykes. The mineralization is associated with a shear zone trending northwest with a 79° dip to the east that was exposed by trenching.

2.4 Mineralogy

2.4.1 Aishihik metamorphic suite

The Aishihik metamorphic suite consists of quartzofeldspathic metasedimentary rocks that are composed of quartz, plagioclase, K-feldspar, biotite and muscovite. The foliation of the unit is defined by color banding and mica alignment (Figure 2.4A). The major minerals are quartz and plagioclase. Both of these minerals have a polygonal texture indicating re-crystallization and the grain size are up to 500 μm across. The quartz is anhedral and the plagioclase is subhedral. Minor minerals are K-feldspar, biotite, muscovite, chlorite, sericite, pyrite, pyrrhotite, chalcopyrite and magnetite. These minerals range in size from less than 100 μm to 300 μm across.

2.4.2 Diorite

Intrusive contacts between diorite and granodiorite were not observed and therefore a gradational change in composition of the same intrusion is assumed. The diorite is fresh, equigranular and consists mainly of randomly oriented plagioclase and biotite (Figure 2.46B). The plagioclase is euhedral, up to 1 mm across and the biotite is subhedral, up to 500 μm across. However, anhedral pyroxene up to 500 μm is present in contrast to amphibole, which is present in the granodiorite. Minor minerals are magnetite, quartz and amphibole as a replacing product of pyroxene.

2.4.3 Granodiorite

The granodiorite is medium to coarse grained, salt and pepper color intrusion with equigranular, randomly oriented grains (Figure 2.4C). The major minerals are plagioclase, amphibole and biotite. Plagioclase has an undulose extinction and occurs mostly as subhedral and euhedral laths up to 1 mm in length. Some plagioclase grains are zoned under cross polarized light. Most plagioclase grains are andesine based on electron microprobe analyses (see Chapter 3). However, one zoned plagioclase analyzed with the electron microprobe has a labradorite core. A few plagioclase grains also exhibit a

myrmekite texture (Figure 2.4D). The amphibole in the granodiorite is a green hornblende. Both the amphibole and biotite are subhedral to euhedral. The amphibole is up to 1.5 mm in length and the biotite is up to 1 mm in length. Some of the hornblende grains have inclusions of finer grained plagioclase, magnetite and biotite and locally hornblende is altered to actinolite.

Minor minerals are quartz, K-feldspar, magnetite with ilmenite exolutions and the accessory minerals are titanite, apatite and zircon. The quartz is up to 200 μm across and is anhedral with undulose extinction. The K-feldspar occurs as interstial anhedral grains up to 500 μm across. Some K-feldspar has planar contacts with plagioclase and is considered to be magmatic whereas other K-feldspar grains show replacement textures with plagioclase and are interpreted as an alteration product. Magnetite is euhedral, up to 500 μm and commonly contains ilmenite exolution lamellae. Titanite is up to 1 mm in length. Two populations of titanite are recognized. One population is characterized by euhedral crystals sharing planar boundaries with other magmatic phases and is interpreted to be magmatic. The second population is characterized by anhedral crystals associated with alteration minerals and is interpreted to be hydrothermal. Apatite and zircon both occur as euhedral crystals 100 μm across and both are interpreted to be magmatic. Secondary minerals include K-feldspar, carbonate, chlorite, sericite, epidote-clinozoisite, chalcopyrite, pyrite, pyrrhotite and titanite.

2.4.4 Aplite dykes

The aplite dykes in hand specimen are white with a sugary texture. They are composed of mainly quartz, K-feldspar, plagioclase and biotite with minor secondary sericite, chlorite, epidote-clinozoisite, titanite, magnetite, chalcopyrite and pyrite. Grain size ranges between 100 μm and 500 μm.

2.4.5 Quartz feldspar porphyry dykes

Quartz feldspar porphyry dykes are composed of a matrix of plagioclase, quartz, K-feldspar, magnetite, with accessory titanite and zircon (Figure 2.4E) grains that are less than 100 μm across. Phenocrysts minerals are up to 0.5 mm in size and consist of anhedral quartz and euhedral plagioclase, hornblende and biotite. Secondary minerals include K-feldspar, carbonate, chlorite, sericite, apatite, epidote-clinozoisite, chalcopyrite, pyrite, pyrrhotite and titanite. Some of the biotite phenocrysts are almost entirely altered to chlorite, carbonate and epidote-clinozoisite.

2.4.6 Mafic dykes

Mafic dykes are either porphyritic or fine grained and equigranular. The main minerals in the matrix are brown hornblende, plagioclase and trace quartz. Secondary minerals are epidote-clinozoisite, chlorite, carbonate and pyrite. Phenocrysts in porphyritic dykes have been completely replaced by chlorite and carbonate. The matrix minerals are up to 100 μm across and the phenocrysts are up to 500 μm across.
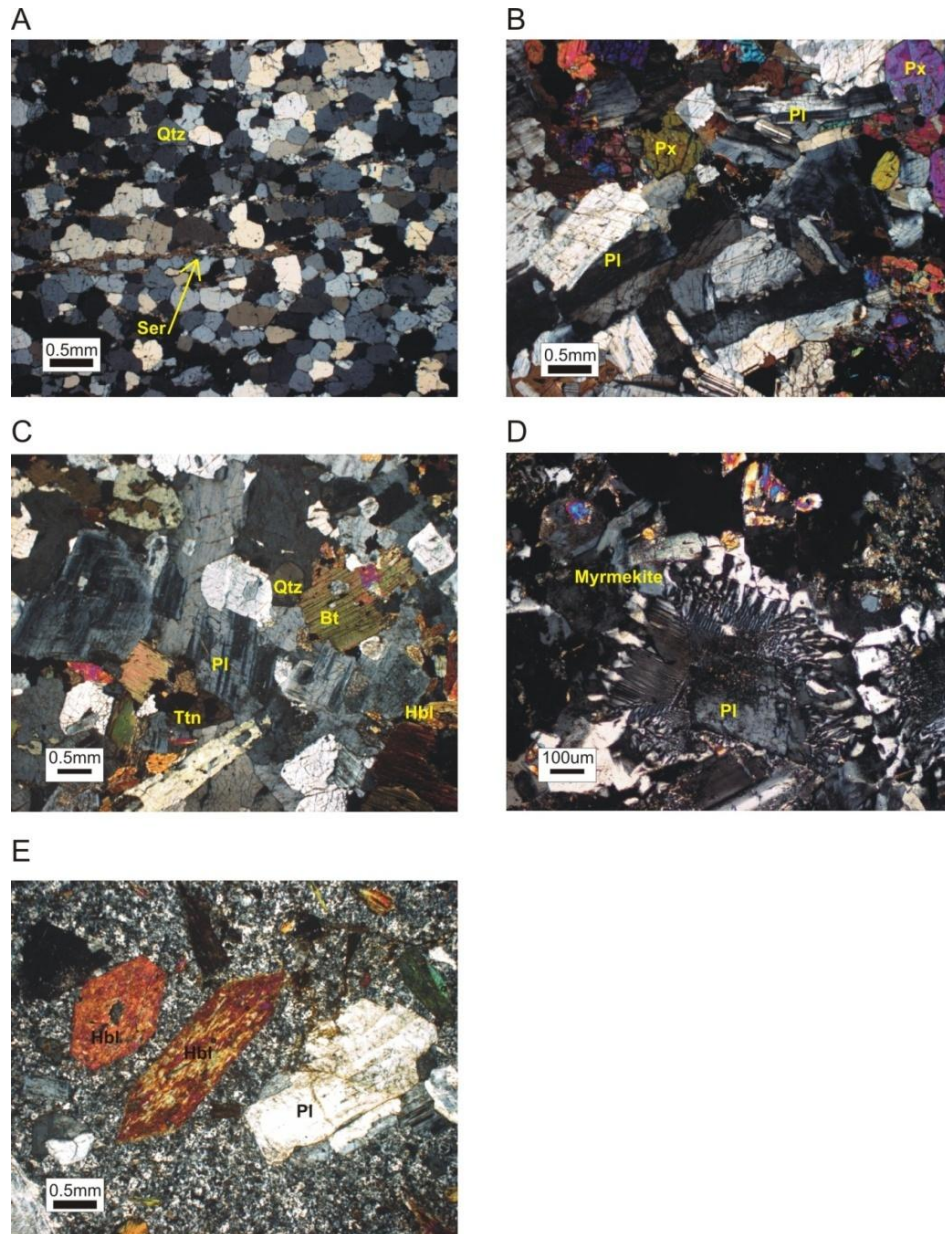
Figure 2.4: Photomicrographs of different rock types at the Hopper property. A. Quartzite of the Aishihik metamorphic suite under cross polarized light. The quartz (Qtz) shows a polygonal texture and the sericite (Ser) defines a foliation. B. Fresh equigranular diorite with pyroxene (Px) and plagioclase (Pl) under cross polarized light. C. Granodiorite under cross polarized light. D. Myrmekite texture in the granodiorite under cross polarized light. E. Plagioclase (Pl) and hornblende (Hbl) phenocrysts in a QFP dyke under cross polarized light.

2.5 Lithogeochemistry of the Hopper intrusion

Lithogeochemistry analyses were completed in order to characterized and classify the intrusion at Hopper property and to compare the intrusive rock types in the area. The analyses are also used in mass balance calculations below. The samples examined are fresh and altered granodiorite, diorite and quartz feldspar porphyry (QFP) dykes from the Hopper property. The samples selected for the analyses were free of weathering, fractures and veins in order to get a representative bulk geochemistry of the rocks. Whole rock lithogeochemical compositions were determined by X-ray fluorescence (XRF) for major elements and Induced Coupled Plasma-Mass Spectrometry (ICP-MS) for trace elements at the Geoscience Laboratories (Geo Labs) in Sudbury, Ontario.

Most of the fresh granodiorite, QFP and some hydrothermal granodiorite samples plot as granodiorite in the quartz, alkali and plagioclase (QAP) diagram (Figure 2.5A) based on mineral abundances from CIPW norm calculations. The remainder of the samples plot between quartz monzodiorite and monzodiorite. These are lower in quartz possibly because of silica loss (See below).

All the samples from Hopper plot as volcanic arc granite using the tectonic discriminant diagram of Pearce et al. (1984; Figure 2.5B) and have a similar calc-alkaline affinity (Figure 2.5C) based on AFM diagram (Irvine and Baragar, 1971). The steep negative slope and negative Nb and Ti anomalies on a spider diagram plot (Figure 2.6) confirm the calc-alkaline affinity of the igneous rocks in the Hopper area. These results coincide with the formation of the Ruby Range batholith that is likely subduction related (Erdmer and Mortensen, 1993). Figure 2.6A represents fresh granodiorite and it is similar to most altered granodiorite samples except altered granodiorite samples have a larger Nb and Zr negative anomalies (Figure 2.6B). The pattern of diorite samples is similar to the fresh granodiorite but the QFP samples exhibit a positive Zr anomaly unlike the other rock types (Figure 2.6C and Figure 2.6D). The REE pattern of QFP however, is similar to the pattern of fresh granodiorite suggesting they are co-magmatic (Figure 2.7).
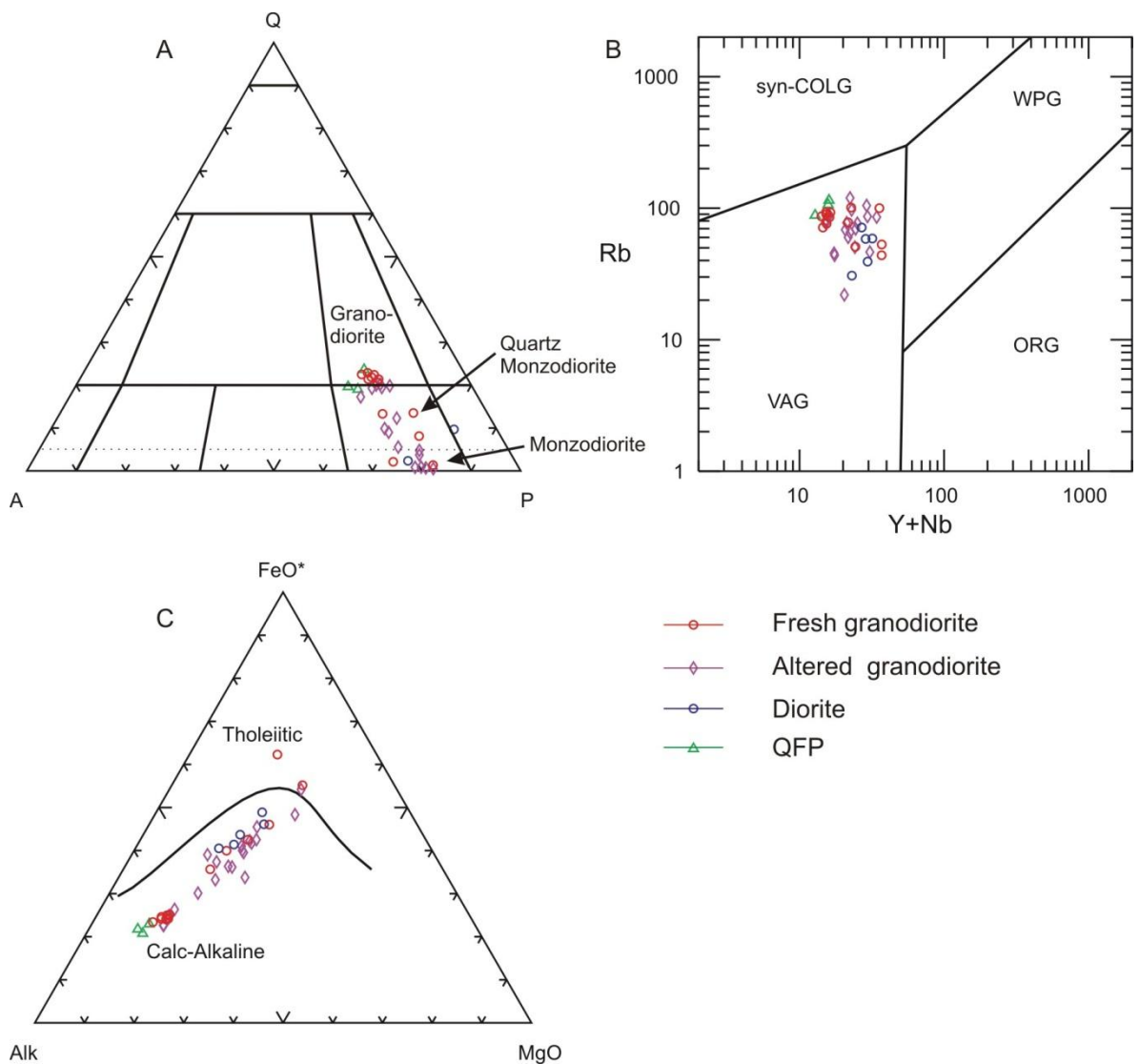
Figure 2.5: Geochemical classification of fresh and altered granodiorite, diorite and QFP from the Hopper property. A. QAP classification diagram (Q=quartz, A=alkali feldspar, P=plagioclase), based on CIPW norm (Streckeisen, 1973). B. Tectonic discrimination diagram after Pearce et al (1984) where VAG=volcanic arc granites, syn-COLG= syn collision, WPG= within plates granites and ORG= ocean ridge granites. C. AFM ternary diagram of Alk=Na$_2$O+K$_2$O, FeO*=FeO$_{total}$ and MgO after Irvine and Baragar (1971).
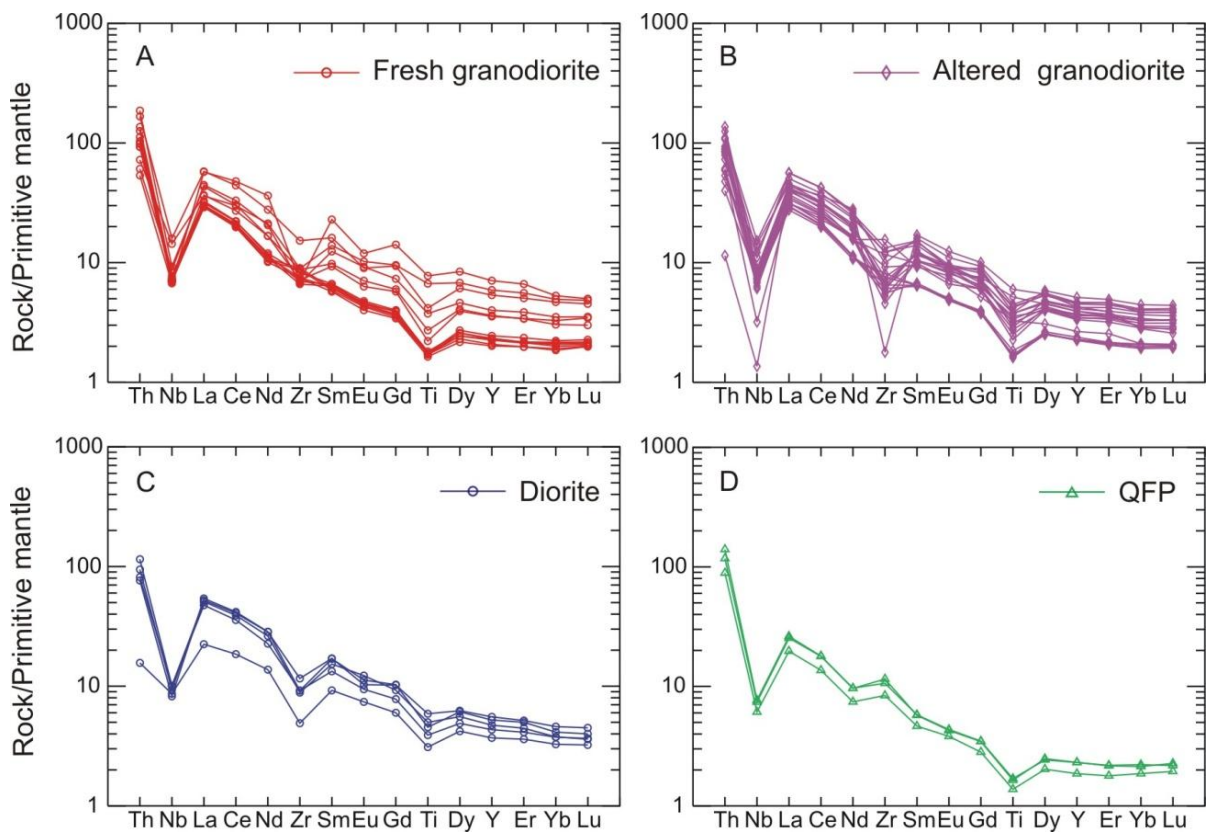
Figure 2.6: Trace element spider diagrams of intrusive samples from the Hopper property normalized to the primitive mantle. A. Fresh granodiorite, B. Altered granodiorite, C. Diorite, D. QFP dyke. Normalized values of the primitive mantle are from Sun and McDonough (1989).
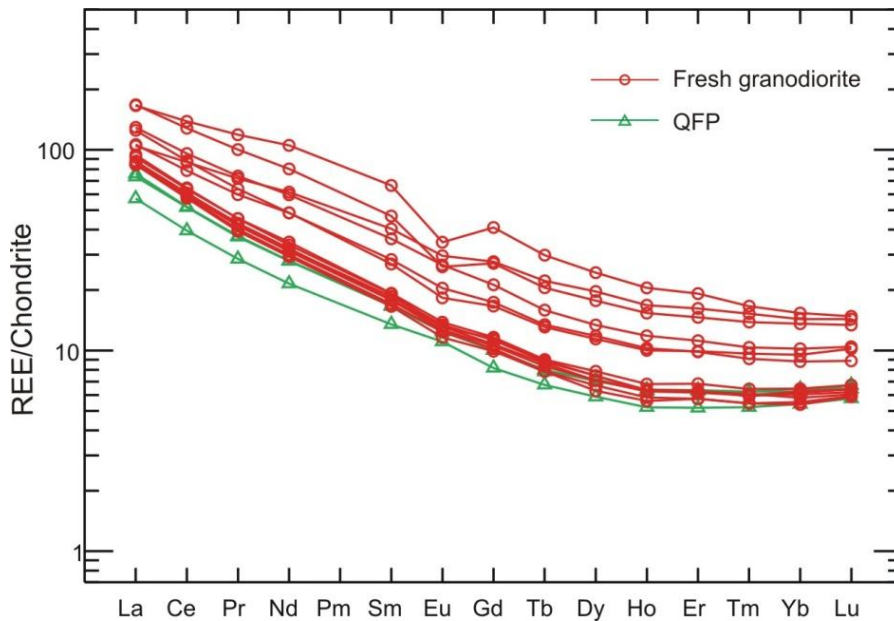
Figure 2.7: REE spider diagram of fresh granodiorite and QFP from the Hopper property. REE values of chondrite are from Sun and McDonough (1989).

2.6 Age dating of the Hopper intrusion

2.6.1 Methodology

Age dates were determined by Balz Kamber and Thomas Ulrich at Laurentian University, Sudbury, Ontario (Kamber and Ulrich, 2009; see the report in Appendix B). Magmatic and hydrothermal titanite and zircon grains of 3 samples from the Hopper granodiorite were separated and analyzed for their U, Th and Pb isotopic composition with Laser Ablation Inductively Coupled Plasma Mass Spectrometer (LA-ICP-MS) in order to date the intrusion and the mineralization. The instrument is a XSeriesII ICP-MS that consist of a small orifice cone of about 0.5 GHz ppm-1 sensitivity. Grains were ablated in ultrapure He with a 213 nm New Wave laser probe. The beam diameter was 40 μm and the laser power was maintained low (10Hz repetition rate and 15J cm-2), and Geostandards reference material 91500 was used for calibration (Kamber and Ulrich, 2009, and Benn and Kamber, 2009). One sample (HB226A) was selected in order to age date the intrusion. It was selected based on the lack of alteration, veins and fractures in this sample and its zircon content, identified by petrography. In order to date the alteration associated with the mineralization, two highly altered and mineralized samples were selected (HB076 and HB140) based on petrographic observations. Hydrothermal titanite grains were analyzed due to their close association with the mineralization,

which could potentially yield the age of mineralization. The samples were crushed, milled and passed over a Wilfley table. These were then processed with a magnetic separator. Zircon occurred in the least magnetic fraction and titanite occurred in the intermediate magnetic fraction. Both were passed through heavy liquid to separate the heavy minerals. Zircon and titanite grains in each sample were mounted on tape and epoxy and were analyzed with a 40 μm beam diameter. A total of 113 data points of zircon grains and 75 data points of titanite grains were analyzed in the three samples.

2.6.2 Results

According to Kamber and Ulrich (2009), zircon U/Pb dating was successful with results that are concordant or near concordant yielding weighted mean ages of 77.2±1.2 Ma (sample HB076; Figure 2.8), 76.0±1.1 Ma (sample HB140; Figure 2.9) and a slightly older sample 83.7±1.9 Ma (sample HB226A; Figure 2.10). Samples HB076 and HB140 both have the same age within error. The Th/U ratios of all three samples is on average above 0.5 implying the zircons are of igneous origin (Hoskin and Schaltegger, 2003), therefore, the age of sample HB226A may represents an earlier crystallization phase of the intrusion. The age of sample HB226A may represents an earlier crystallization phase of the intrusion. The youngest age of Hopper (76.0±1.1) is 3.6 Ma younger than the age of the intrusion hosting the Casino porphyry copper deposit that is 72.4±0.5 Ma (Selby and Nesbitt, 1998). These results correspond well with the ages from the margins of the Ruby Range batholith that range between 56 and 90 Ma (Johnston, 1993). These results are based on all data points except one from HB076, one from HB140 and two from HB226A that were all rejected statistically as well as one inherited zircon in sample HB226A (444 Ma of age). Both the hydrothermal and magmatic titanites could not be used for age dating due to low radiogenic Pb (206, 207 and 208) contents, a high common ^{204}Pb concentration and trace mercury, which adds to ^{204}Pb. Because of the low ^{206}Pb/^{204}Pb ratio, accurate dates could not be obtained using this method (Kamber and Ulrich, 2009).
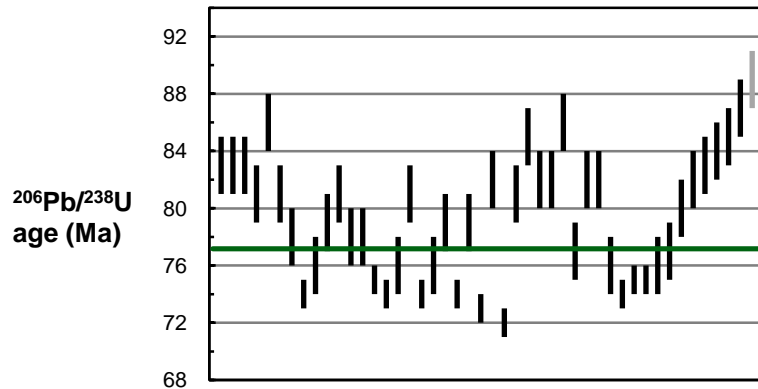
Figure 2.8: ^{206}Pb/^{238}U age of zircons from an altered and mineralized granodiorite (sample HB 076) yielding a weighted mean of 77.2±1.2 Ma (n=46 with 1 of 46 rejected in grey), placing the intrusion at the same age as the intrusion hosting the mineralization at the Casino copper deposit (Kamber and Ulrich, 2009).
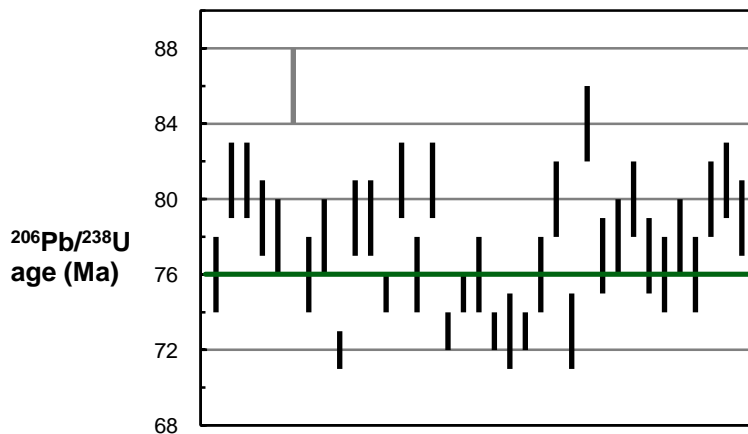
Figure 2.9: ^{206}Pb/^{238}U age of zircons from an altered and mineralized granodiorite (sample HB 140) yielding a weighted mean of 76.0±1.1 Ma (n=35 with 1 of 35 rejected in grey), placing the intrusion at the same age as the intrusion hosting the mineralization at the Casino copper deposit (Kamber and Ulrich, 2009).
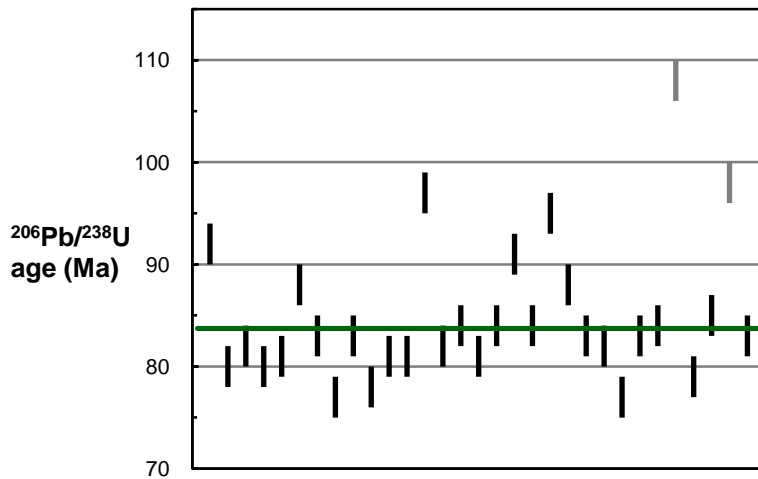
Figure 2.10: ^{206}Pb/^{238}U age of zircons from a fresh granodiorite (sample HB 226A) yielding a weighted mean of 83.7±1.9 Ma (n=31 with 2 of 31 rejected in grey; Kamber and Ulrich, 2009).

2.7 Alteration

Based on petrographic and field observations, the alteration occurs in two main assemblages at the Hopper property, potassic and propylitic. Minor, discontinuous occurrences of skarn alteration are also present at the property.

2.7.1 Potassic alteration assemblage

Potassic alteration consists of fine to medium grained K-feldspar and rarely also biotite. It occurs as veins and as replacement of plagioclase and hornblende (Figure 2.11A). The potassic alteration was observed in granodiorite, QFP, metasediments and aplite dykes. Rarely, fine grained biotite is an alteration product of hornblende. The degree of K-feldspar alteration was determined by etching the samples with hydrofluoric acid and staining with sodium cobaltinitrite by Vancouver Petrographics (Appendix J). This process stains K-feldspar yellow which allows determining the visual percentage of K-feldspar in samples. The software MapInfo was used to create grid surface thematic maps showing the degree of K-feldspar and chlorite alteration spatially. The percentage of K-feldspar shows no correlation with the mineralization (Figure 2.12). Mass balance calculations confirm the lack of correlation between potassic alteration and mineralization and in fact potassium is lost during mineralization (see below). There is also minor incipient sericite alteration of plagioclase, biotite and

hornblende in granodiorite, QFP, metasediments and aplite dykes. However, it is not clear whether it is associated with potassic or propylitic alteration.
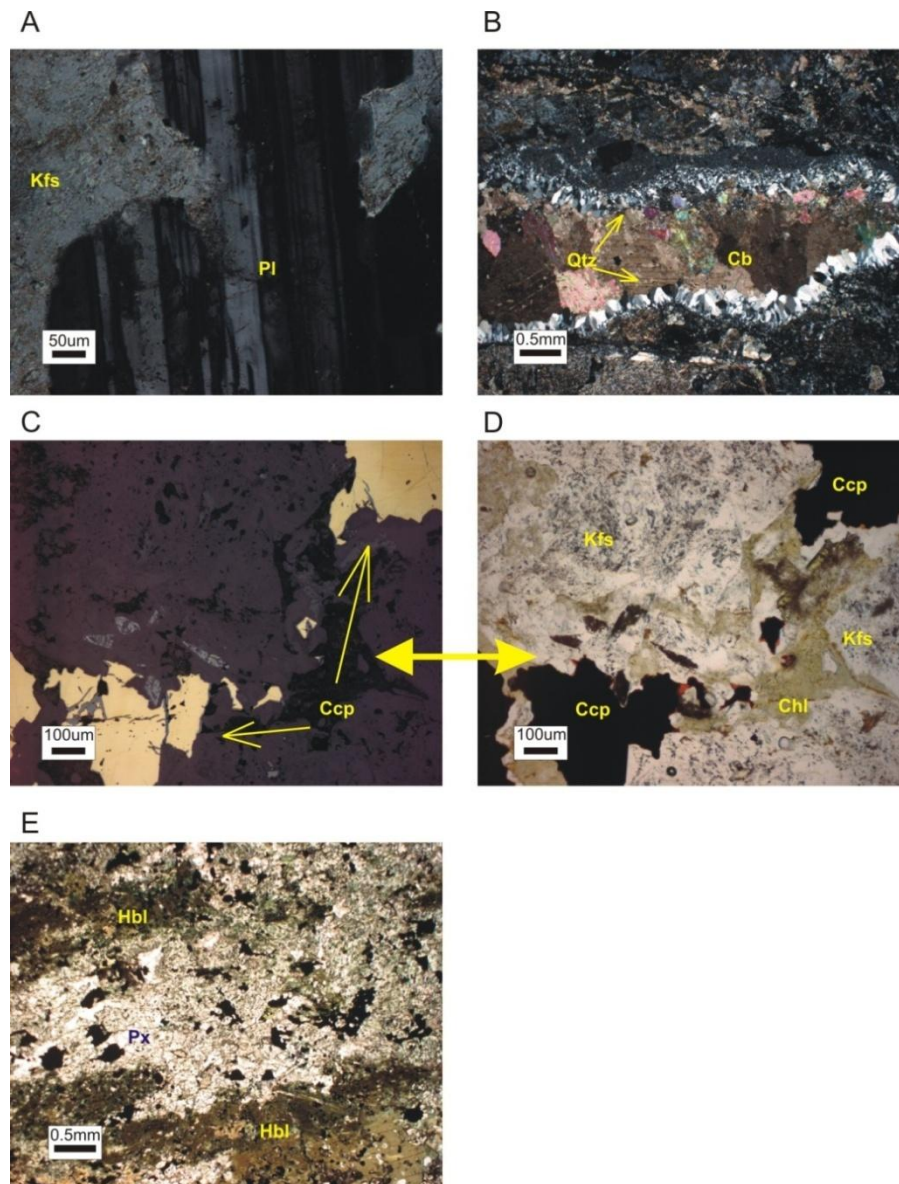
Figure 2.11: Photomicrographs of alteration and mineralization of the Hopper intrusion and skarn. A. K-feldspar (Kfs) replacement of plagioclase (Pl) under cross polarized light. B. Quartz (Qtz) carbonate (Cb) vein with a comb texture in an aplite dyke under cross polarized light. C. Chalcopyrite (Ccp) under reflected light. D. The same chalcopyrite under plane light showing the association of chalcopyrite with chlorite. The chlorite in this sample cross cuts a K-

feldspar vein. E. Skarn alteration with alternating layers of hornblende (Hbl) and pyroxene (Px) under plain polarized light.
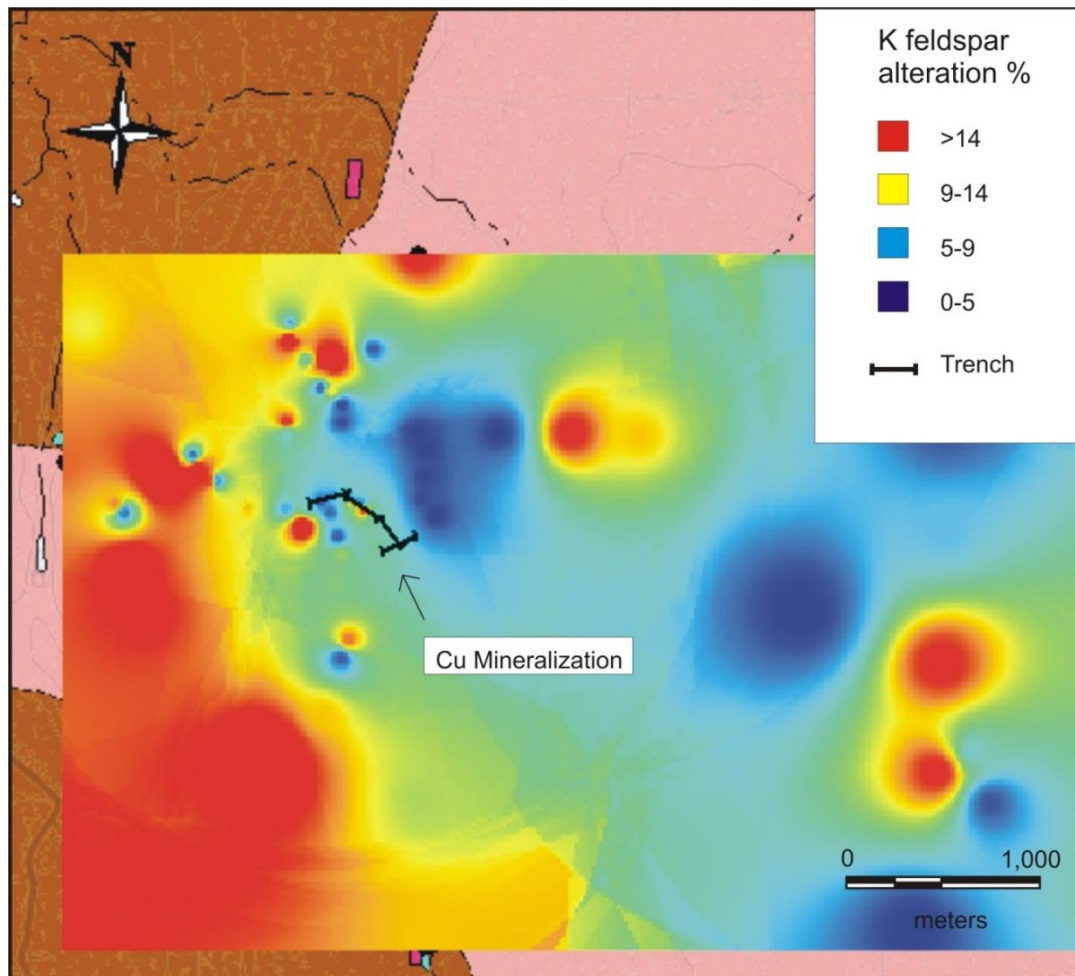
Figure 2.12: Spatial distribution of K-feldspar alteration at the Hopper property based on visual percentage estimates of stained samples. According to this map, K-feldspar alteration is very restricted and does not correlate to the mineralization.

2.7.2 Propylitic alteration assemblage

Propylitic alteration is observed in granodiorite, metasediments, mafic dykes, skarn, aplite dyke and QFP dykes. The propylitic alteration assemblage consists of chlorite, carbonate, epidote-clinozoisite and titanite (Figure 2.13). The close correlation between chlorite and titanite indicates that these titanite grains are hydrothermal in origin. Some of the titanite grains are replaced by ilmenite. This has also been observed by Broska et al (2007) who related the replacement of titanite by ilmenite to

the alteration of plagioclase to sericite and the alteration of biotite to chlorite. The alteration minerals range in size between fine and coarse grained and are randomly oriented. They are commonly anhedral and the chlorite exhibits a fibrous texture in some cases. Chlorite commonly is present as patches in hornblende and plagioclase and along cleavages of biotite. Chlorite is observed to have completely replaced biotite, but it also occurs in fractures without replacement of other minerals. The propylitic alteration is mainly a product of alteration of biotite and hornblende. Carbonate and clinozoisite also altered plagioclase. Carbonate is also present with quartz in mm wide quartz-carbonate veins. One quartz carbonate vein exhibits a comb texture (Figure 2.11B). The propylitic alteration occurs as dissemination in the matrix and along fractures. These fractures were observed to cross cut K-feldspar alteration (Figure 2.11C and Figure 2.11D), therefore propylitic alteration is later than potassic alteration. Figure 2.13 summarizes the timing relationship of the alteration and mineralization at Hopper property.

   Chalcopyrite and molybdenite occur with the propylitic alteration, specifically with the chlorite, titanite and clinozoisite-epidote both as dissemination in the matrix and along fractures together with chlorite, epidote and titanite (Figure 2.11C and Figure 2.11D). Spatially, there is a strong correlation between chlorite and the copper mineralization. Figure 2.14 shows the close spatial association between the chlorite alteration percentage of hornblende and biotite compared to the mineralization zone.

2.7.3 Skarn alteration

The skarn at Hopper occurs as small discontinuous outcrops. It is characterized by banded layers of anhedral green hornblende and pyroxene (Figure 2.11E). Pyroxene grains are up to 300 μm and hornblende grains are up to 1 mm across. Other major minerals in skarn are plagioclase, magnetite and titanite. Minor minerals are quartz, chlorite, epidote-clinozoisite, pyrrhotite, chalcopyrite and pyrite. Apatite is present as an accessory mineral.

Minerals | Magmatic minerals | Potassic alteration | Propylitic alteration Main mineralization Syntectonic | Supergene oxidation stage

Time →

Quartz

Plag

Biotite

Hornblende

Zircon

titanite

Apatite

Sericite

K feldspar   ?

Chlorite

Epidote-clinozoisite

Carbonate

Actinolite   ?

Magnetite

Pyrrhotite

Ilmenite

Pyrite

Chalcopyrite

Molybdenite

Malachite

Goethite
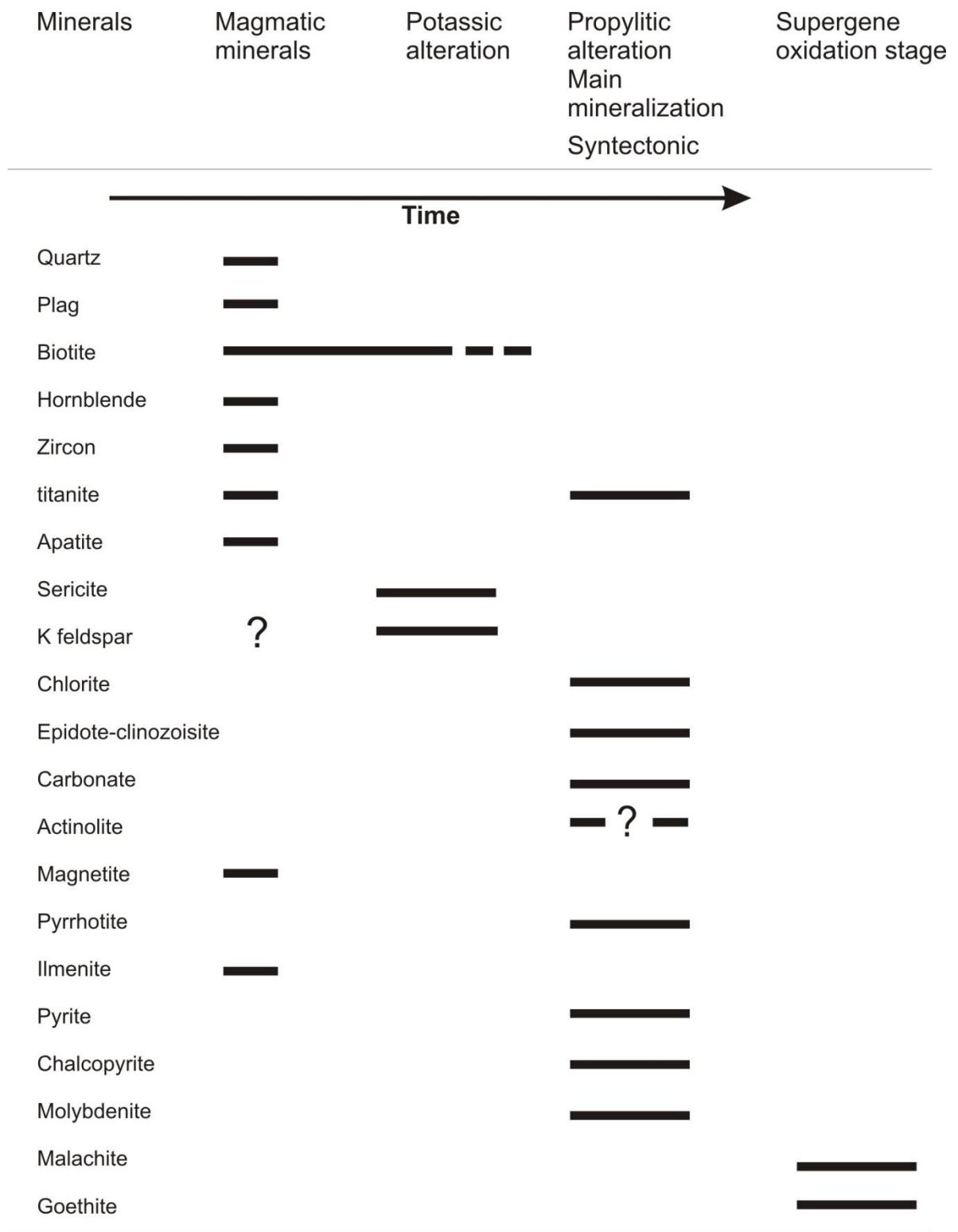
Figure 2.13: Alteration and mineralization timing relationship based on petrographic analysis.

26
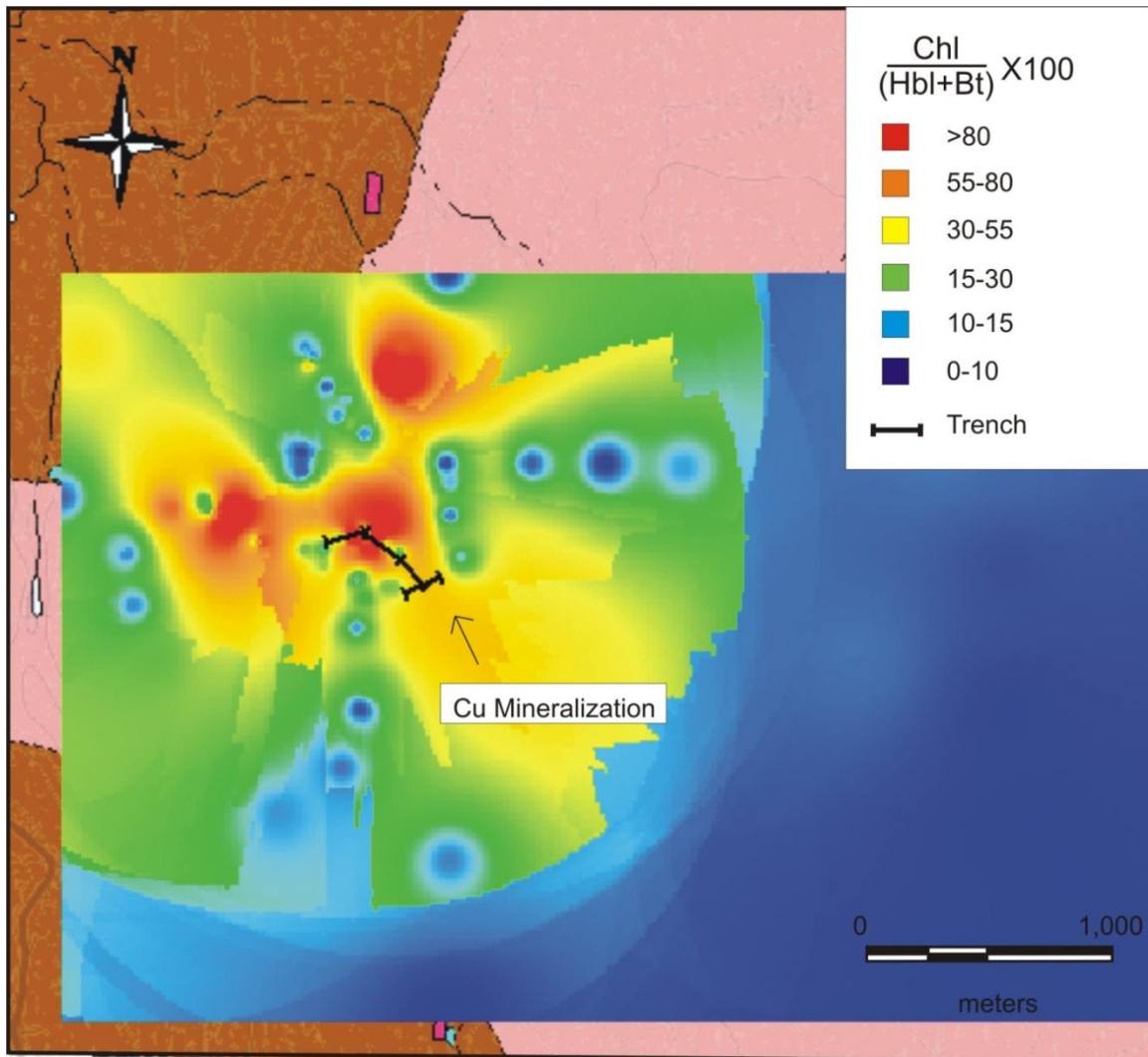
Figure 2.14: Alteration map of chlorite at the Hopper property based on petrography. The chlorite is plotted as a percentage of chlorite/(hornblende+biotite) based on petrographic analysis of granodiorite samples. The figure shows a clear correlation between the copper occurrence and chlorite alteration.

2.8 Mineralization

The majority of the copper and molybdenite is hosted in the granodiorite in a small shear zone. The shear zone is defined by foliated chlorite with slickenside structures and trend 318° with a 79° dip to the northeast. The main zone of mineralization is located in an area roughly 500 m long and 20 m wide. Both chalcopyrite and molybdenite occur in a random orientation as disseminations and along

fractures and shear surfaces. Both are anhedral and range in size from less than 50 μm to roughly 500 μm across. Petrographic observations revealed that the chalcopyrite occurs with chlorite, hydrothermal titanite, carbonate and epidote-clinozoisite (Figure 2.11C and Figure 2.11D) and that chalcopyrite is in planar contact with chlorite, titanite and epidote-clinosoisite. It is therefore interpreted to be directly associated with the propylitic alteration. Spatially there is also a correlation between the chalcopyrite occurrence and propylitic alteration as indicated in Figure 2.14. Chalcopyrite was also observed as an inclusion in one possibly magmatic, euhedral titanite (see Chapter 4). Chalcopyrite also occurs in trace amounts in metasediments, aplite and QFP dykes. Molybdenite occurs only in granodiorite as disseminations and on shear surfaces associated with chlorite.

Other opaque minerals include pyrite, pyrrhotite and magnetite with ilmenite exolutions. Magnetite occurs in the Hopper intrusion as a euhedral crystal, up to roughly 500 μm across and is disseminated. The magnetite is likely magmatic due to its occurrence in the matrix and lack of any correlation with other hydrothermal minerals or fractures and the ilmenite exsolution lamellae, which indicate that it crystallized at high temperature. It is also found as inclusions in magmatic hornblende, further indicating that it is magmatic in origin. Pyrite and pyrrhotite are also disseminated in the granodiorite, the metasediments, and the QFP dykes. Pyrite is euhedral, up to 500 μm across and occurs together with the chalcopyrite. In some cases it also has chalcopyrite as inclusions. The pyrrhotite is finer grained and is only present in trace amounts with pyrite and chalcopyrite.

2.9 Sulphur isotopes analysis

Seven samples were analyzed for sulphur isotopes at Queen's University in order to determine the source of sulphur at the Hopper property. For comparison purposes, sulphur isotopes were analyzed from 3 mineralized granodiorite samples from the Hopper property and 4 mineralized skarn core samples from Janisiw showing, 3 km west of the Hopper property (Table 2.1). The granodiorite samples contain chalcopyrite and pyrite that yielded $\delta^{34}S$ ranging between -0.8 to -1.7 per mil. The skarn samples consist of chalcopyrite and pyrrhotite that yielded $\delta^{34}S$ ranging between 0.7 to -0.6 per mil.

Table 2.1: Summary of sulphur isotopes data.

Sample Location	Sample Number	Rock Type	Sulphide Seperates	$\delta^{34}S(CDT)$
	HB076		Chalcopyrite +pyrite+ 65% silicates	-1.7±0.3
	HB077		Chalcopyrite+pyrite	-0.8±0.3
Hopper Property	HB152	Granodiorite	Chalcopyrite+pyrite	-1.0±0.3
	RL-08-26		Pyrrhotite	0.7±0.3
	RL-08-29		Chalcopyrite + pyrrhotite	-0.6±0.3
	RL-08-30		Chalcopyrite + pyrrotite	-0.2±0.3
Janisiw	RL-08-35	Skarn	Chalcopyrite + pyrrotite + 20% silicates	0.0±0.3

2.10 Mass Balance

2.10.1 Methodology

Every type of hydrothermal mineralization is commonly associated with alteration as a result of interactions between fluids carrying ore and the host rock. Therefore, characterization of the nature of the fluids and the alteration can serve as a useful tool in exploration (Lesher 1986 and Appleyard, 1990). Understanding the characteristics of the fluids can help to understand the physical and chemical conditions that led to mineralization. Commonly there are certain pathfinder elements that change in concentration closer to the mineralization (Appleyard, 1980). During an alteration event, material may be either added to or removed from the original parent rock, but these mass changes and their magnitude are not always apparent (Appleyard, 1990).

In order to quantify the elemental changes in concentration that took place during an alteration event, mass balance calculations are carried out by comparing between the background elemental levels in the parent rock (typically assumed to be the least altered rock) and altered rocks. Choosing the right parent material is crucial in calculating mass changes because the calculations are done by using a reference parent material (Grant, 1986). The least altered rock is chosen based on field and petrographic observations. As recommended by Ulrich and Heinrich (2001), the chosen altered rocks are clear of vein filling to better represent bulk replacement of rocks during alteration instead of fracture filling. The least altered sample chosen for this study is characterized by lower lost on ignition (LOI), $Fe_{(total)}$, MgO, Cu, Al_2O_3/Na_2O and $Al_2O_3/(Na_2O+K_2O)$ values than the altered rocks. It also has a consistent Zr versus SiO_2 values with other least altered rocks compared to altered rocks that show a scatter. Petrographic analysis also indicated the sample chosen is fresh although it contains 10 modal percentage of K-feldspar. The K-feldspar in the sample is considered magmatic because it does not show replacement textures with other minerals.

Lithogeochemistry data for the mass balance calculations can be used based on one of the following assumptions (Grant, 1986 and Appleyard, 1990):

1. Assume that no mass change has occurred

2. Assume that there has been no change in volume when making corrections for density changes. Arguments for constant volume rely on textural evidence of textural preservation in altered rocks. However, this assumption is difficult to be made when there have been permeable changes in the alteration zones (Lesher et al., 1986).

3. Assume some elements were immobile during alteration. Commonly elements such as Ti, Al, Zr and REE elements are considered to have been immobile. This allows for volume changes calculations.

This study characterizes volume and mass changes during alteration associated with copper mineralization based on methods developed by Grant (1986) and Gresens (1967) assuming some elements are immobile. It applies to alteration that is pervasive and not alteration that appears in veins. The calculations based on Gresens (1967) method used the SOMA computer program of Appleyard and Memarian (2003).

The general metasomatic equation of Gresens (1967) suggests a method for the mass balance calculation which has been applied in many studies of alteration processes (e.g. Grant 1986 and Appleyard, 1990). This method is based on the assumption that during any alteration there are always some elements that are immobile and these can be utilized to calculate changes in concentration. Dissolution and precipitation of minerals during alteration is the cause for gains and losses of elements. Some of the factors controlling this process are pressure, temperature, water-rock ratio, time and fluid composition. The mobility of both major and trace elements is controlled by these factors. Elements with low ionic potential such as LIL trace elements (large ion lithophile) are commonly mobile whereas HREE (heavy rare earth elements) are much more immobile due to their more intermediate ionic potentials. In addition, HREE are mostly contained by accessory minerals such as zircon that are much less susceptible to alteration than micas and feldspars where LIL elements are found (Lesher et al., 1986).

A common volume factor (FV) is then applied to the behavior of all elements when calculating the gains and losses (Grant, 1986). The volume factor is defined as the ratio between the initial and final volumes of the rock or the volume change factor when there is a zero change in mass of an element,

i.e., if using immobile elements (Appleyard, 1980 and Grant, 1986). The immobile elements show a clustering behavior of their FV calculated from the Gresens' equation (Appleyard, 1990).

Gresens (1967) wrote an equation to calculate the change in mass and the difference in composition between the parent and altered rock, but in order to calculate mass change, the FV needs to be calculated first. The equation for FV is as follow:

Equation 2.1:

$$FV_\eta^0 = \frac{\rho^0 * \chi_\eta^0}{\rho^A * \chi_\eta^A}$$

Where FV_η^0 is the volume change for element η where there is a zero change in η. ρ^0 is the density of the parent rock, χ_η^0 is the concentration of element η in the parent rock and χ_η^A and ρ^A refer to the altered rock (Appleyard, 1990). Once the FV is known $\Delta\chi$ can be calculated according to the following equation:

Equation 2.2:

$$\Delta\chi_\eta = \left(\frac{v^A * \rho^A}{v^0 * \rho^0} * \chi_\eta^A\right) - \chi_\eta^0$$

Where v^A/v^0 equals FV.

The data are presented as $\pm\Delta\chi_\eta$ or as net composition with absolute values where $\pm\Delta\chi_\eta$ is added to the original composition of the parent rock. This method takes in account volume changes and specific gravities (Appleyard, 1980). There are three possible ways to solve for FV according to Appleyard (1990):

1. To physically calculate volume change based on physical parameters. This solution is not feasible in most cases.
2. Assume a specific element is immobile.
3. Assume that in most alteration events there is a group of immobile elements. These can be selected due to their FV values clustering behavior when comparing between the FV values of the parent versus the altered rock. The mean of the clustered FV is the best value to represent the actual volume change.

Grant (1986) proposed a simple graphical method based on Gresens' equation where Gresens' equation is rewritten as a linear equation representing the relationship between the concentration of an element in the altered rock compared to its concentration in the parent rock. The linear solution for all

components that show no gain or loss between altered and parent rock defines an isocon. The equation for the isocon is:

Equation 2.3:

$$\chi^A = (M^0 / M^A) * \chi^0 \; .$$

M^0 and M^A are the masses before and after alteration. Each element has a constant value of (M^0 / M^A). The value of (M^0 / M^A) can be determined graphically since it is the slope of the isocon that passes through the origin when plotted as altered versus parent rock concentrations. The slope of the line defines the mass change in the alteration. Points that fall above the isocon gained mass and points below the isocon lost mass (Grant, 1986). The mass change is given by Grant's basic equation that is based on the Gresens' method is

Equation 2.4:

$$\Delta\chi_\eta / \chi_\eta^0 = (M^A / M^0) * (\chi_\eta^A / \chi_\eta^0) - 1$$

Where $\Delta\chi_\eta / \chi_\eta^0$ is gained or lost mass of an element η relative to χ_η^0. If the immobile elements are known for which $\Delta\chi_\eta = 0$, it is possible to solve the equation of the isocon. The isocon method is based on assumption that either the mass is constant or the volume is constant (Grant, 1986). An example for an isocon based on a fresh sample and an altered and mineralized sample from Hopper is presented in Figure 2.15. Elements above the isocon have gained in concentration such as Cu and Mo and elements below the isocon lost in concentration such as Na_2O, SiO_2 and K_2O.

2.10.2 Results

In order to calculate the gains and losses based on the Grant (1986) method, immobile elements have to be selected. They were selected based on the clustering behavior of the values of the ratio of elements in the altered versus the same value in the parent rock, $(\chi_\eta^A / \chi_\eta^0)$. The clustering behavior of FV values and the formation of an isocon by certain elements were also taken into consideration in the immobile elements selection process. The elements selected as immobile are Yb, Sm, Nd and Gd. REE commonly act as immobile elements as well as Al, Zr and Ti. The calculations were also done with Al and Zr as immobile elements for comparison purposes and are presented in Appendix F. The elements that gained over 10 grams/10^6 grams in all samples are: Cu, Mo, V, Zn, FeO and MgO. The elements lost over 10 grams/10^6 grams in all samples are Ba, Cr, Rb, Zr, Al, K_2O, Na_2O and SiO_2. Any change below 10 grams/10^6 grams is close to the detection limit. Figure 2.15 is an example of an

isocon between a least altered granodiorite sample and an intensely mineralized and altered granodiorite.
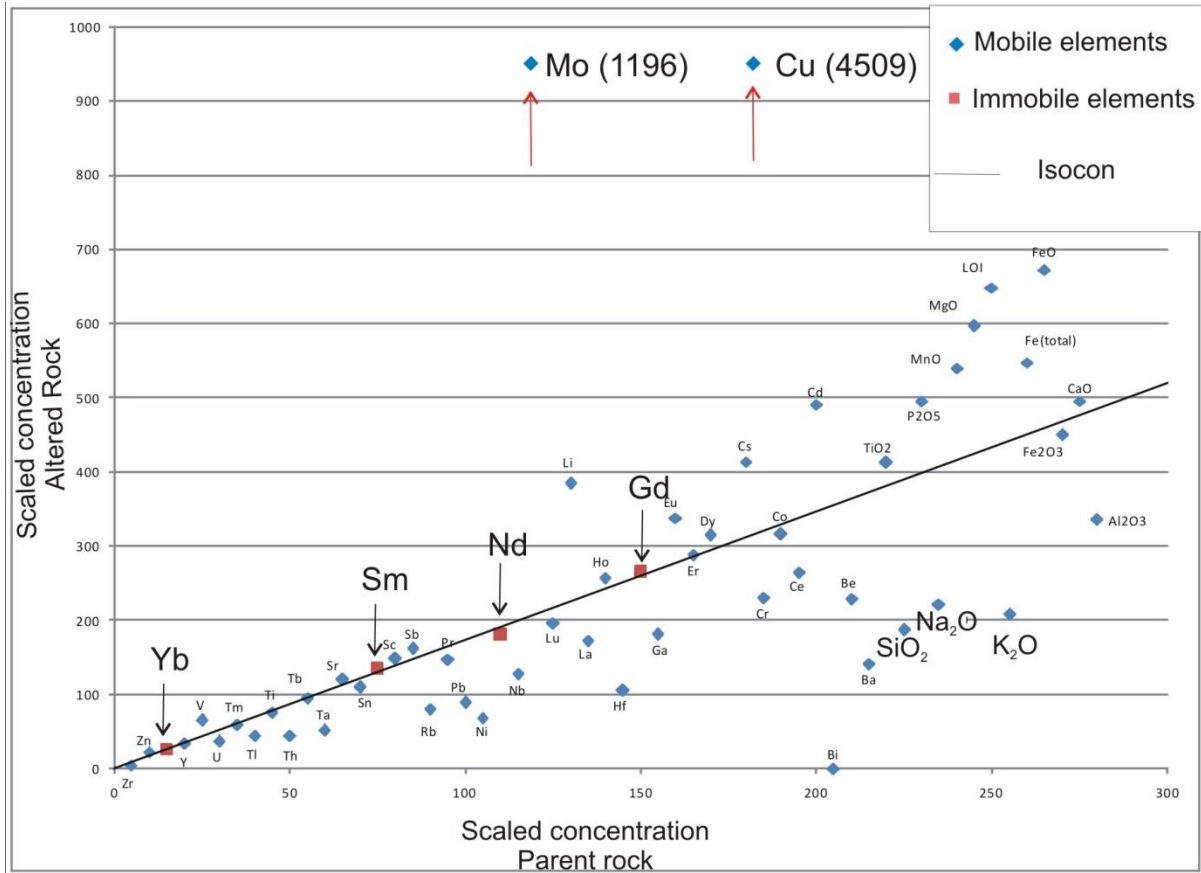
Figure 2.15: An example of an isocon between a least altered granodiorite (HB216) and a mineralized and altered granodiorite (sample HB098A). The values have been rescaled to fit in the plot. The red squares represent the immobile elements forming the isocon (Yb, Sm, Nd and Gd). The mobile elements that plot above the isocon (such as Cu and Mo) gained in concentration and the elements that plot below the isocon lost in concentration (such as SiO_2, Na_2O and K_2O).

According to the Grant method, in all samples Ba shows the largest concentration loss for trace elements of over 1204 grams/10^6 grams. The largest gain of trace elements is of Cu which gained up to 410 grams/10^6 grams, unlike Mo that gained only 20 grams/10^6 grams compared to the parent rock. Ti however, shows both gains of up to 1207 grams/10^6 grams and losses of up to 394 grams/10^6 grams. Another notable gain is V, which gained 127 grams/10^6 grams. Rb lost up to 78 grams/10^6

grams and Cr lost up to 37 grams/ 10^6 grams. Sr shows both losses and gains compared to the parent rock. It lost up to 301 grams/10^6 grams and gained up to 171 grams/10^6 grams. One of the major elements that shows the largest loss is SiO_2 with up to 49.20 grams/100 grams loss. K_2O lost up to 2.72 grams/100 grams and Na_2O lost up to 3.25 grams/100 grams. FeO gained up to 1.39 grams/100 grams similar to Fe_2O_3 with a gain of 1.16 grams/100 grams (although Fe_2O_3 also lost 0.95 grams/100 grams). CaO shows a gain of 1.19 grams/100 grams although some samples lost CaO up to 1.12 grams/100 grams. MgO gained up to 1.52 grams/100 grams and lost up to 0.17 grams/100 grams. Except for one sample that gained in Al_2O_3 concentration (2.05 grams/100 grams), all samples lost up to 9.39 grams/100 grams. An example for these gains and losses is presented in Figure 2.16 and Figure 2.17.
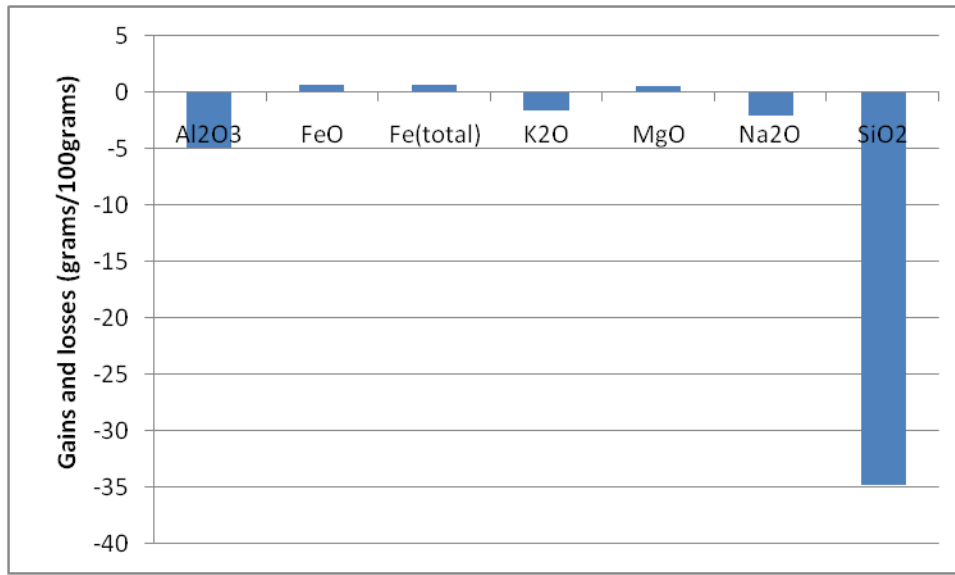
Figure 2.16: An example of major elements gained and lost in an altered and mineralized sample (sample HB098A) relative to a least altered rock based on Grant's method, where Yb, Sm, Nd and Gd are selected as immobile elements. Elements above the 0 change are gained and below 0 are lost. The altered sample shows a clear desilicification as well as a loss in Al_2O_3, K_2O and Na_2O. There is also a very minor increase in FeO and MgO.
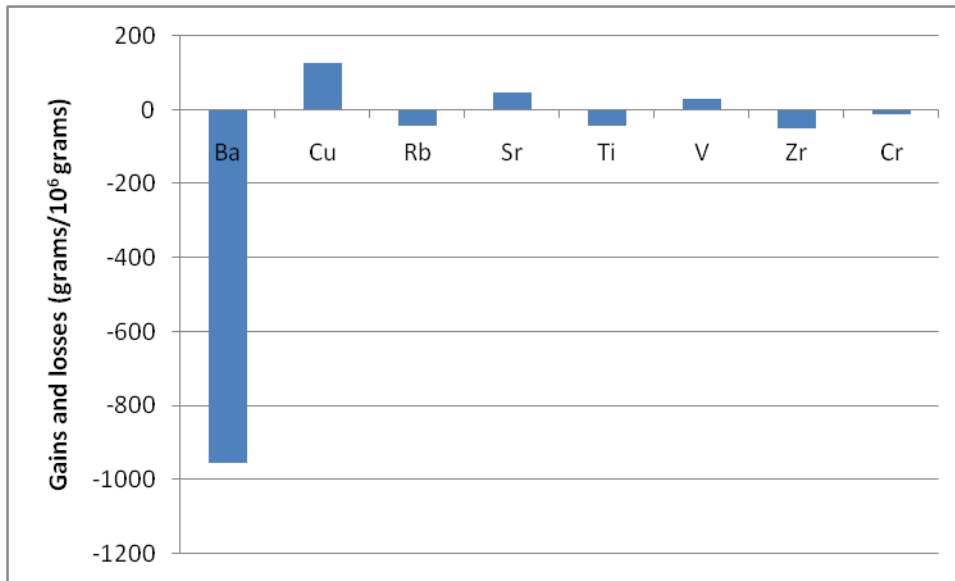
Figure 2.17: An example of trace elements gained and lost in an altered and mineralized sample (sample HB098A) relative to a least altered rock based on Grant's method when Yb, Sm, Nd and Gd are selected as immobile elements. Elements above the 0 change are gained and below 0 are lost. In this case, Ba, Rb, Ti and Zr show a loss in concentration and Cu, Sr and V show a gain in concentration. Changes in concentration of less than 10 grams/10^6 grams are not considered.

Calculations by Gresens' method using the SOMA program developed by E.C., Appleyard and M. Memarian (2003) show the same quantitative results. The results of Gresens' method however, are presented here as elements instead of oxides. Elements chosen as immobile are the same as those chosen for the calculations based on Grant's method and these include Yb, Sm, Nd and Gd. The elements that show a loss in concentration are: Ba, Cr, Rb, Zr, Al, K, Na and Si. Elements that show a gain in concentration are: Cu, Mo, V, Zn, Fe, and Mg. Quantitatively, the gains and losses have the same values (±1-2 grams/100 grams) compare to the Grant method when calculating the change in concentration. Si lost up to -21.46 grams/100 grams and Al lost up to 4.97 grams/100 grams except one sample that gained 1.17 grams/100 grams Al. Mg and Fe^{2+} gained up to 0.93 grams/100 grams and 1.09 grams/100 grams respectively. Mn and P show very small changes and can be considered immobile in this case. Na lost up to 2.28 grams/100 grams and K lost up to 1.66 grams/100 grams. Ca show both loss and gain in the samples between 0.80 and 0.81 grams/100 grams. Among the trace elements, Cu gained up to 413.40 grams/10^6 grams and Mo gained up to 20.40 grams/10^6 grams. An

example of mass balance calculations of a mineralized example compare to a least altered sample based on Gresens' method is presented in Figure 2.18 and Figure 2.19.
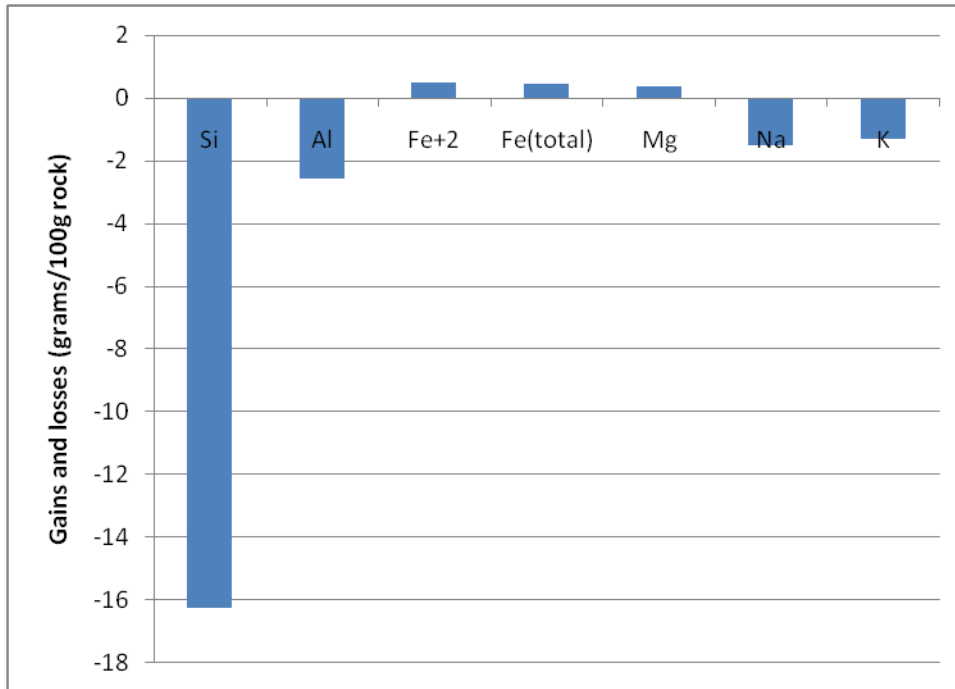
Figure 2.18: An example of major elements gained and lost in an altered and mineralized sample (sample HB098A) relative to a least altered rock based on Gresens' method. Calculations were done using SOMA when Yb, Sm, Nd and Gd are selected as immobile elements. Elements above the 0 change are gained and below 0 are lost. The altered sample indicates a clear desilicification as well as a loss in Al, K and N. There is also a minor increase in Fe^{2+} and Mg.
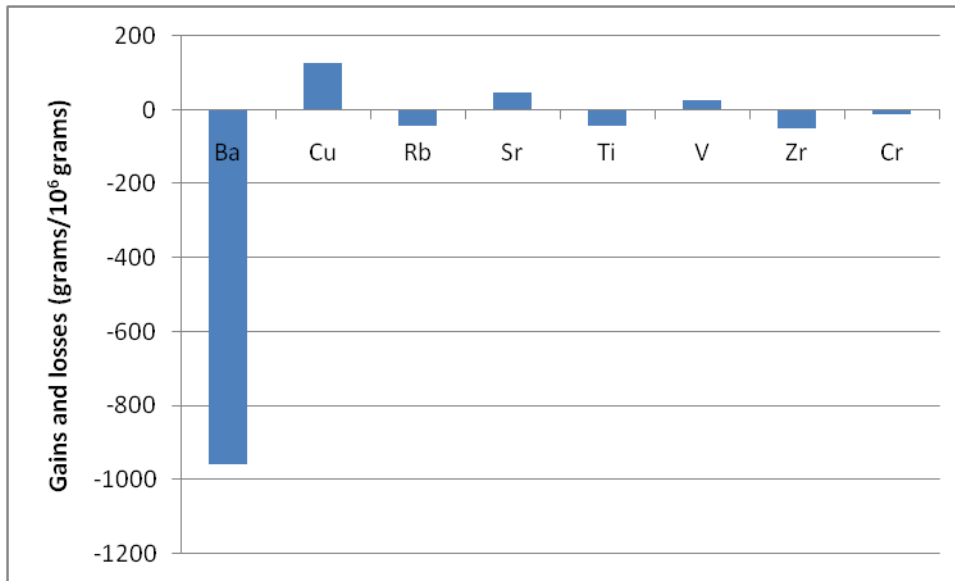
Figure 2.19: An example of trace elements gained and lost in an altered and mineralized sample (sample HB098A) relative to a least altered rock based on Gresens' method when Yb, Sm, Nd and Gd are selected as immobile elements. Elements above the 0 change in ppm are gained and below 0 ppm are lost. In this case, Ba, Rb, Ti and Zr were lost and Cu, Sr and V were gained. Changes of less than 10 grams/10^6 grams are not considered.

Figure 2.20 shows a plot of Si loss versus chlorite percentage in biotite and hornblende. According to this figure, it is evident that the high loss in Si is associated with greater values of chlorite and a minor loss in Si is associated with lower chlorite percentage. However, when plotting the Si loss versus distance from the mineralization there is no clear linear relationship between the two (Figure 2.21).
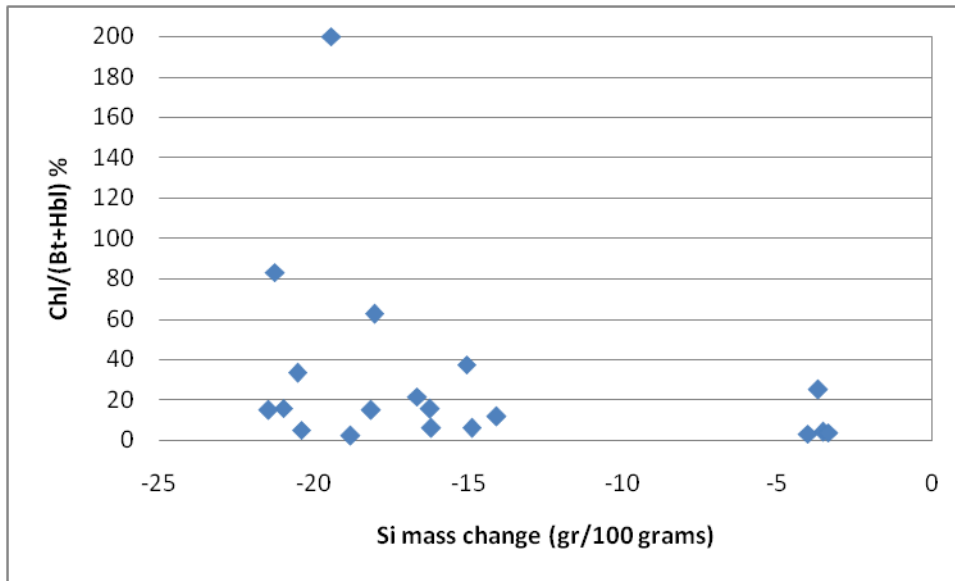
Figure 2.20: Variations in Si loss versus chlorite alteration of hornblende and biotite percentage. The Si loss values are based on mass balance calculations using Gresens' method with Yb, Sm, Nd and Gd selected as immobile elements. The chlorite percentage values are based on modal percentage. The figure shows higher loss of Si corresponds with higher values chlorite percentage.
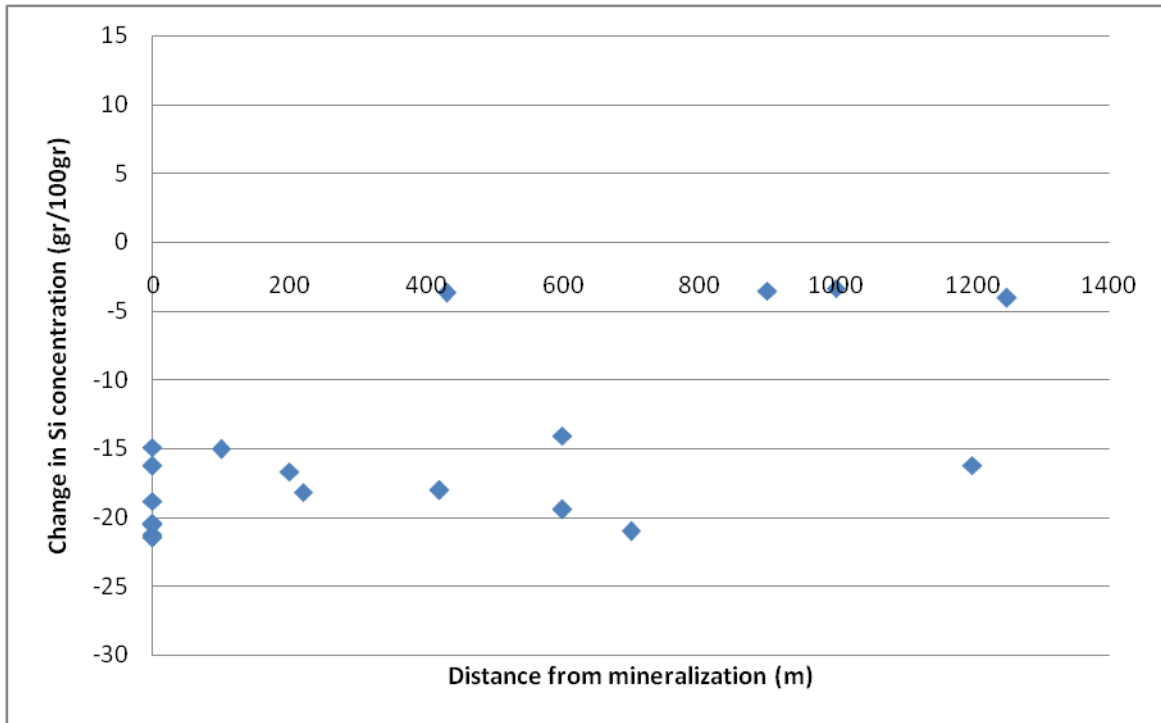
Figure 2.21: Variations in Si loss versus distance from mineralization show a weak correlation between the two. The Si loss values are based on mass balance calculations using Gresens' method with Yb, Sm, Nd and Gd selected as immobile elements.

The losses of Al and Ba are also related to the chlorite alteration. Figure 2.22 shows a weak negative trend between chlorite alteration percentage and loss of Al (grams/100 grams) except for one sample. A similar trend is observed when Ba is plotted versus the chlorite alteration (Figure 2.23) indicating the propylitic alteration is probably characterized by Al and Ba loss as well as Si.
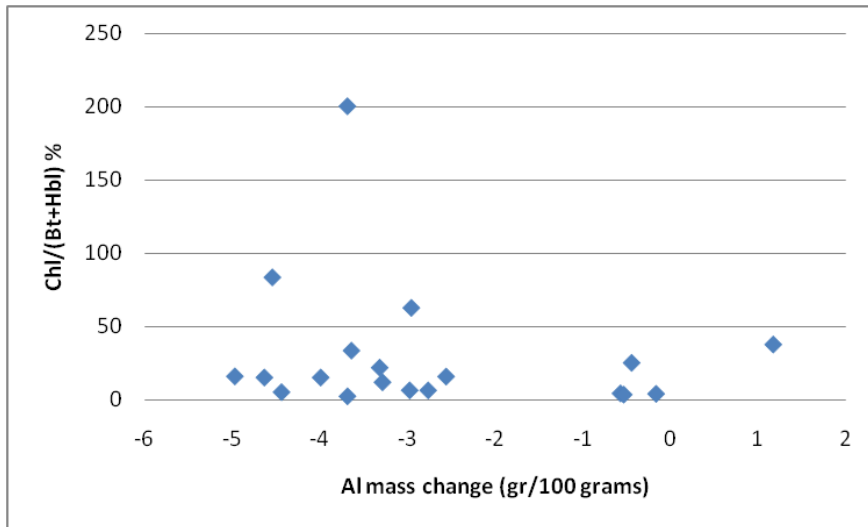
Figure 2.22: Variations in Al loss versus chlorite alteration of hornblende and biotite percentage. The Al loss values are based on mass balance calculations using Gresens' method with Yb, Sm, Nd and Gd selected as immobile elements. The chlorite percentage values are based on modal percentage. The figure shows higher loss of Al corresponds with higher values chlorite percentage.
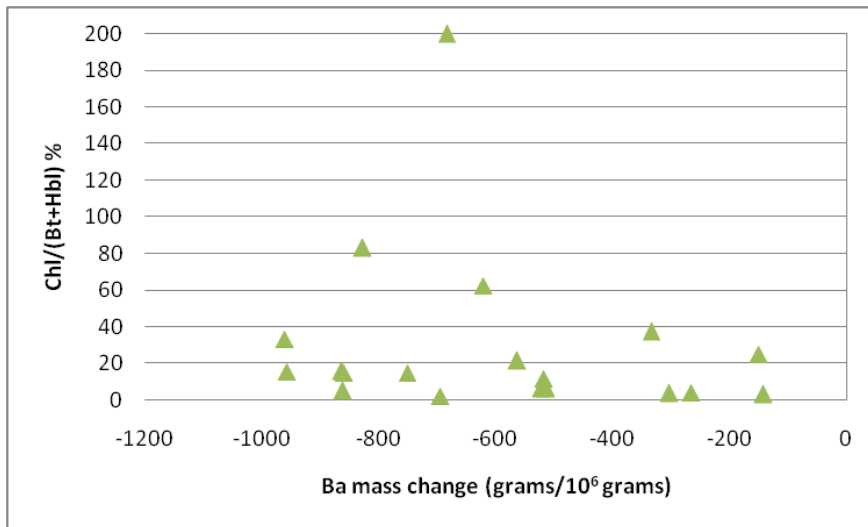
Figure 2.23: Variations in Ba loss versus chlorite alteration of hornblende and biotite percentage. The Ba loss values are based on mass balance calculations using Gresens' method with Yb, Sm, Nd and Gd selected as immobile elements. The chlorite percentage values are based on modal percentage. The figure shows higher loss of Ba corresponds with higher values chlorite percentage.

2.11 Discussion

It is possible that the Hopper property contains porphyry type mineralization because of the many similarities between a typical porphyry copper type deposit and the mineralization at the Hopper property. Hopper is situated in close proximity to other porphyry copper deposits such as the Carmacks, Minto and Casino (Selby and Nesbitt, 2000). In addition, it is hosted in a calc-alkaline granodiorite intruded by QFP dykes, similarly to other porphyry type deposits. Another similarity is that the mineralization consists of mainly chalcopyrite and molybdenite that occur as disseminations and along fractures and occur where both potassic and propylitic alterations are found. Three samples from the Hopper intrusion yielded 77. 2 ± 1.2 Ma, 76.0 ± 1.1 Ma, and slightly older 83.7 ± 1.9 Ma based on zircon U/Pb age dating using LA-ICP-MS (Kamber and Ulrich, 2009). These results are similar to the intrusion hosting the Casino porphyry copper deposit that is 72.4 ± 0.5 Ma (Selby and Nesbitt, 1998). Typical porphyry copper deposit is characterized by potassic alteration at the core surrounded by phyllic, propylitic and argillic alteration zones consecutively (Gustafson and Hunt, 1975).

However, unlike typical porphyry copper deposits, the copper mineralization at Hopper occurs along fractures, a shear surface and with close association with the propylitic alteration instead of potassic or phyllic alteration. Mass balance calculations based on the methods of Gresens (1967) and Grant (1986) show that the mineralization is closely related to silica loss, as well as K_2O, Na_2O, Al_2O_3, Ba, Cr, Rb and Zr losses and gains in Cu, Mo, V, Zn, FeO and MgO. The loss of K_2O therefore clearly shows that potassic alteration is not significant. Silica was released from quartz and other magmatic minerals. Samples that lost Ca probably released Ca from plagioclase which also released Ba and Sr and Al when altered to sericite. The lost Ca and Si escaped the system along fractures as space filling quartz-carbonate veins. Fe and Mg were probably added to the system from Fe and volatile rich fluids. The added Fe together with Mg form epidote-clinozoisite and chlorite, and Fe combined with S form sulphides. Some samples showed a gain of Ca. The combination of Ca with LOI (which likely includes CO_2) is probably responsible for the propylitic alteration and formation of chlorite and carbonate. These results are consistent with other mass balance calculations in other propylitic occurrences, as discussed below.

Porphyry copper and gold deposit at the Bajo de la Alumbrera, Argentina, a textbook example for a porphyry type mineralization, shows similar results in a mass balance study by Ulrich and Heinrich (2001), based on the Grant (1986) method . The deposit is a well known gold-rich porphyry copper deposit in northwestern Argentina, 200 km east of the main Andean copper belt in Chile. The deposit

is characterized by a classic porphyry type alteration zoning. The earliest alteration at Bajo de la Alumbrera is quartz-magnetite alteration. This zone grades into a potassic alteration, which is characterized with biotite and K-feldspar. This alteration is surrounded by a propylitic outer halo. The alteration is then overprinted by feldspar-destructive alteration including sericite, pyrite $\pm$ clay and $\pm$ gypsum.

According to Ulrich and Heinrich (2001), the potassic zone that is associated with the mineralization shows large gains in K, Si, S, Au and Cu and losses in Na, Ca, Sr, and Ba. The propylitic alteration at the edge of the deposit gained CO_2 and Ca that could have come from the Ca depleted potassic zone. Other major gains in the propylitic zone are in Zn, Pb, Mn, Sn, H_2O, and Ba. Na, K, Sr, Al, V, Cr, Co, W and Rb showed losses in concentrations. The propylitic alteration zone also shows a significant desilicification. This is similar to Hopper that has gains in Zn and losses in Si, Rb, Na and K.

The mineralization found at Hopper occurs along a small shear surface, therefore it is interesting to compare between the mass balance in Hopper copper occurrence and mass balance in other shearing occurrences. Goddard and Evans (1995) investigated the structural and geochemical characteristics of two thrust faults formed at 4-7 km and 10-12 km depth in crystalline thrust sheets in northwestern Wyoming. Their mass balance calculations results are very similar to Hopper. Rocks at the shallow level exhibit 10-40% depletion of Si, Al, K, Na and Ca and 0-20% depletion of Si, Al and K at the fault core. These soluble elements were depleted during a syntectonic fluid flow. Goddard and Evans (1995) found that SiO_2, Al_2O_3, CaO, Na_2O and K_2O were lost and that Fe_2O_3, MgO and LOI (CO_2 and H_2O) were gained. Losses of SiO_2 and Al_2O_3 are due to feldspars having been altered to sericite, clays and other phyllosilicates and transport of the soluble elements out of the system. The gains in Fe_2O_3 and MgO can be explained by the fractures filled with kaolinite and Fe oxides found in the area.

Ductile shearing associated with gold in the Okote area in southern Ethiopia yielded LOI, Fe_2O_3, K_2O, P_2O_5, Ba, Cu, Sr and V gains and MgO, CaO and SiO_2 losses in a chlorite-carbonate-biotite schist according to Deksissa and Koeberl (2004). This is unlike Hopper that lost K and Ba and gained MgO. The addition of K in this case is related to biotite, muscovite and K-feldspar alteration. Chlorite, carbonate and pyrite are related to the volatile addition. MgO, CaO and SiO_2 were depleted and precipitated along veins of quartz-carbonate-tourmaline. The epidote-amphibole-chlorite schist also found in the area gained Fe_2O_3, MnO, Na_2O, P_2O_5, SiO_2 and TiO_2 and lost MgO, CaO and K_2O. The Fe_2O_3, MnO and TiO_2 gains are probably related to the formation of Fe rich epidote, magnetite,

42

ilmenite and titanite and the addition of SiO_2 is represented by silicification of the schist. MgO and CaO were depleted and precipitated in the quartz-carbonate veins. Carbonation and hydration related to the formation of chlorite, carbonates, epidote and albite is usually related to the release of SiO_2, MgO, FeO and CaO from ferromagnesian minerals, which were then precipitated as fracture filling of quartz-carbonate veins (Deksissa and Koeberl, 2004).

Metasomatism in other shear zones that are related to gold occurrences most commonly show increases in LOI and S concentrations, as observed in the Rundle gold deposit in the Swayze greenstone belt of the Abitibi sub-province (Love and Roberts 1991) and in the Villeranges Basin, Marche-Combrailles Shear zone in northwestern France (Boiron et al., 1989). However, the behavior of many other elements such as Si, K varies between different shearing events.

2.12 Genetic model for the Cu mineralization at the Hopper property

The main focus of this study was to develop a genetic model for the copper mineralization at the Hopper property. Based on field and laboratory results, two possible models for the mineralization are proposed. One model is the ortho-magmatic model (i.e., derived from a magmatic-hydrothermal system) where the mineralization at Hopper is related to a porphyry system and was remobilized to the propylitic zone. The other possible model is the shear-related mineralization model. In this case the mineralizing fluids are not genetically related to the host intrusion, but rather are associated with a regional deformation event.

The copper and molybdenite mineralization at the Hopper property are possibly ortho-magmatic and related to a porphyry occurrence at depth. Results to support this hypothesis include the age of the host intrusion, whole rock chemistry, S isotopes and geological settings. Similar to typical porphyry copper deposits, the Hopper mineralization is hosted in a calc-alkaline intrusion. The granodiorite, hosting the mineralization, is located roughly 200 km south of the Casino porphyry copper deposit both of which are of similar ages, hosted in late Cretaceous intrusions. Other porphyry copper deposits in the area are Minto and Cash deposits, although these are Jurassic of age. In British Columbia, ages of porphyry copper deposits are upper and middle Jurassic, late Cretaceous, Eocene and Oligocene (Sillitoe, 1972). Hopper is also similar to classical porphyry copper deposits in that the granodiorite hosting the mineralization is intruded by quartz feldspar porphyry dykes and is characterized by both propylitic and potassic alteration types. In addition, like most porphyry copper deposits, the copper and molybdenum mineralization at the Hopper property occur as disseminated chalcopyrite and molybdenite in granodiorite that also hosts quartz carbonate veins. However, the

43

majority of the mineralization at Hopper is focused along fractures related to a small shear zone and it is associated with propylitic alteration cross cutting potassic alteration, in contrast to most porphyry copper type deposits where the main mineralization is associated with potassic alteration. Therefore, it is likely the copper and molybdenite have been remobilized and redistributed. It is possible the remobilization took place syntectonically because the mineralization occurs along a shear surface. Mass balance calculations confirm the association between gaining of Cu and Mo with a loss in Si and K as expected in a propylitic alteration.

Similar remobilization took place in Bajo de la Alumbrera in Argentina where late stages of fluid input caused remobilization of mineralization, resulting in chalcopyrite and pyrite mineralization along late fractures with chlorite and sericite. The mineralization in Bajo de la Alumbrera is also found in later intrusions due to the remobilization (Ulrich and Heinrich, 2001). Sulphur isotopes from the mineralization at Hopper also indicate a magmatic source for the mineralization (which can include remobilized magmatic sulphur). The $\delta^{34}S$ values for chalcopyrite and pyrite from the granodiorite at the Hopper property ranges from -0.8 to -1.7 per mil, consistent with a magmatic source (Ohmoto and Rye, 1979). This supports the notion that the mineralization at the Hopper property is a porphyry type mineralization which follows the ortho-magmatic model. A summary of this model is given in Figure 2.24.

45
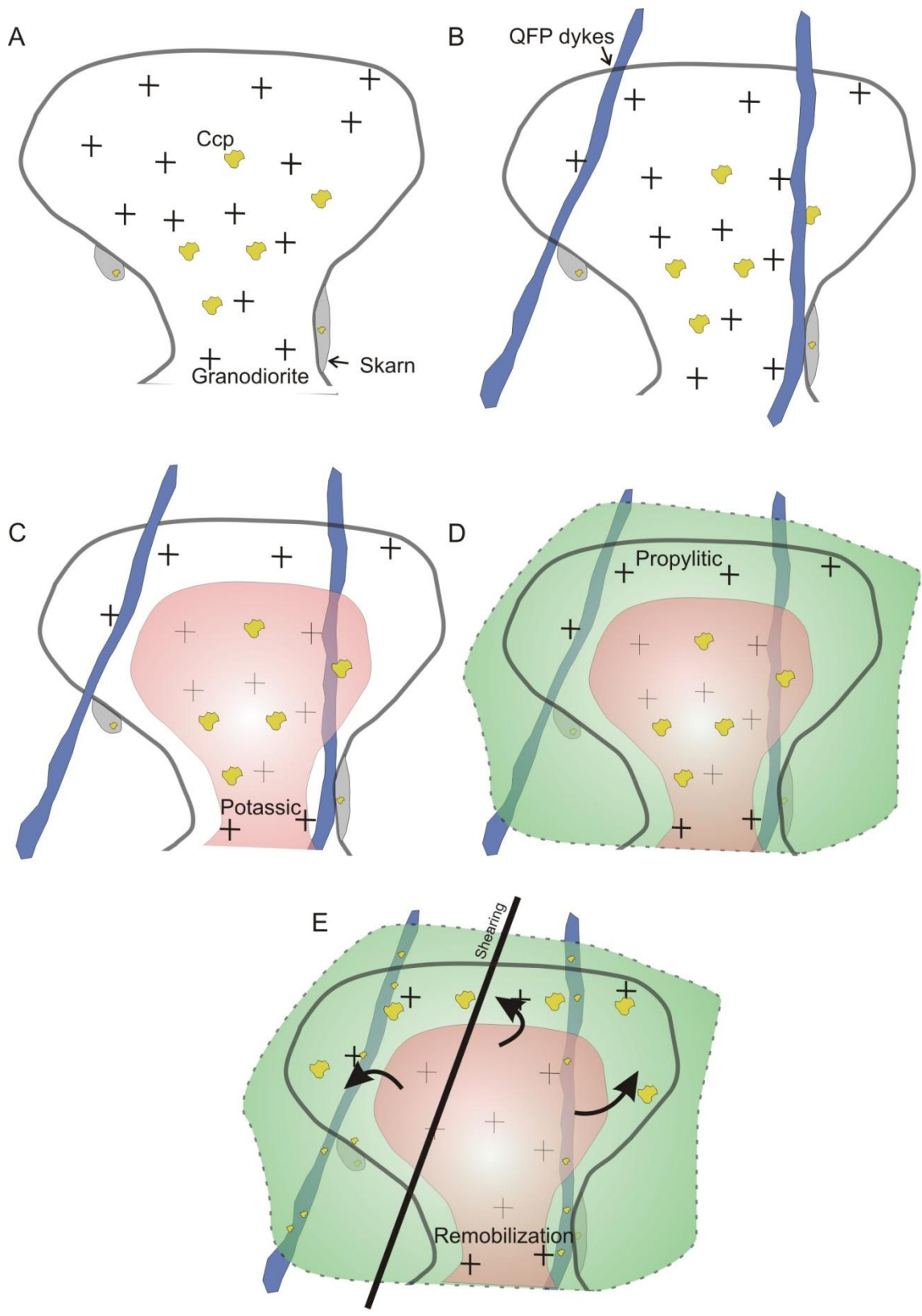
Figure 2.24: The ortho-magmatic model for the mineralization at Hopper. A. The granodiorite intruded during the late Cretaceous resulting in skarn alteration. This mineralization includes ortho-magmatic fluids that are responsible for the mineralization. B. The granodiorite was intruded by QFP dykes. C. Potassic alteration including K-feldspar and biotite altered the granodiorite and the QFP dykes. D. Propylitic alteration occurred at the margins of the potassic alteration and overprinted it based on cross cutting relationships. E. Remobilization of the mineralization from the potassic zone to the propylitic zone occurred. It is suspected to be syntectonic with the shearing due to the occurrence of the mineralization on a slickenside surface.

One problem with the first model is that the QFP dykes found at Hopper are mineralized as well. These dykes could range in age between late Cretaceous to Eocene based on lithological correlations (Johnston and Timmerman, 1994). If the dykes are late Cretaceous and are similar in age to the Hopper intrusion, the ortho-magmatic model is plausible. However, if the QFP dykes are much younger (Eocene in age) than the Hopper intrusion, then the mineralization might not be related to the intrusion. In this case, another possible explanation for the copper occurrence at the Hopper property is that it was remobilized through a shearing event and brittle deformation from a different location, possibly a copper skarn occurrence which is found in the same locality (Figure 2.25). The occurrences of copper and molybdenite together with propylitic alteration that cross cuts potassic alteration along fractures and a shearing plane support this argument. In addition, S isotopes from the skarn mineralization had values ranging between 0.7 δ^{34}S to -0.6 δ^{34}S. These values are similar to the ones from Hopper, suggesting both occurrences could be of similar origin. However, if the QFP dykes are indeed Eocene in age, the mineralization could be late Cretaceous mineralization remobilized to the QFP dykes during the Eocene.
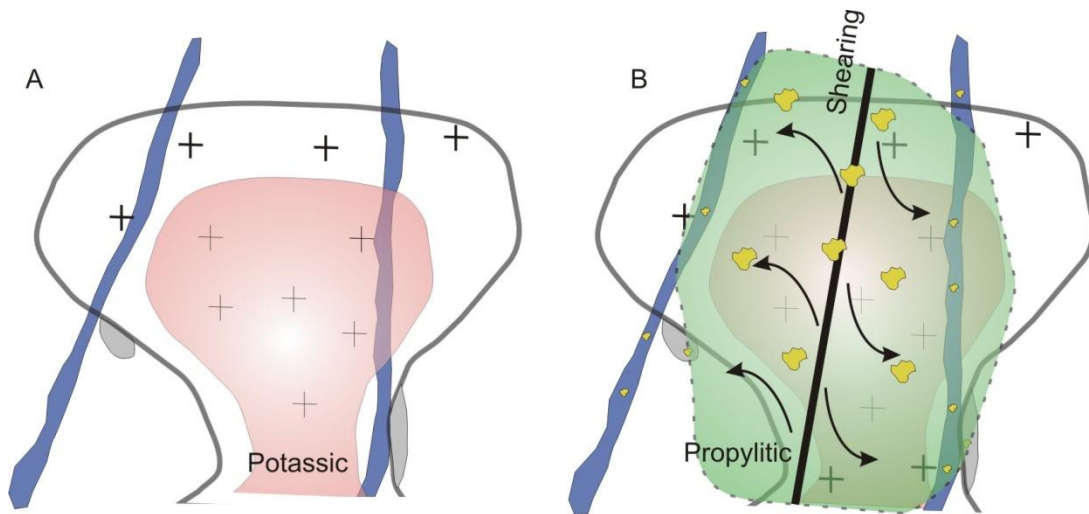
Figure 2.25: The shearing model. A. The intrusion is not related to the mineralization and is barren. Potassic alteration took place but it is not associated with a mineralization. B. Mineralization occurred together with propylitic alteration during shearing.

2.13 Conclusions

The mineralization at the Hopper property is associated with shearing and propylitic alteration minerals that include chlorite, epidote-clinozoisite, carbonate and titanite. These results agree with mass balance calculations based on Gresens' and Grant's methods indicating a loss in silica and potassium which contradict the classical model for the mineralization in porphyry copper deposits according to which mineralization is associated with potassic alteration. Both Gresens' and Grant's methods showed that the altered granodiorite lost SiO_2, Na_2O, K_2O, Ba, Rb, and Cr, and gained in addition to Cu and Mo, FeO, Fe_2O_3, MgO, CaO, and V.

There are two possible models for the mineralization at Hopper property based on field work and geochemical analyses. One possible model for the copper occurrence is that the mineralization at Hopper is related to a porphyry system and the copper and molybdenite have been remobilized like the copper found with propylitic alteration in Bajo de la Alumbrera. The lithogeochemistry data, the sulphur isotopes ($\delta^{34}S$) and the age of the intrusion strongly suggest the mineralization is of ortho-magmatic origin. The second model is a shear related mineralization.

Chapter 3
Mineral Chemistry

3.1 Introduction

This chapter presents geochemical compositions of minerals from the Hopper intrusion based on analyses using an electron microprobe in order to compare the Hopper intrusion to other known porphyry copper deposits. Minerals analyzed are magmatic plagioclase, biotite and amphibole, and hydrothermal chlorite. These minerals are the main constituents of the magmatic composition of the intrusion and the hydrothermal alteration. Results of titanite analysis are presented in Chapter 4.

Mineral chemistry is commonly used in order to understand the conditions at which mineralization occurs. Studying the chemistry of minerals such as biotite, amphibole and chlorite can assist in reconstructing the conditions under which they crystallized, such as temperature, pressure and fugacity ratios of HF, HCl and H_2O of the mineralizing fluid (Panigrahi et al., 2008).

Biotite is an interesting mineral to study because it contains a hydroxyl site which undergoes substitution and at high temperature there is a F-Cl-OH exchange with hydrothermal fluids (Munoz, 1984, Selby and Nesbitt, 2000 and Panigrahi et al., 2008). Similar to biotite, hydrothermal amphiboles have a unique chemical signature of compositions ranging from hornblende to Mg-rich actinolite (Chivas, 1981 and Agemar et al., 1999).

Chlorite is the main alteration product associated with the copper mineralization at the Hopper property. It is a common alteration product of fluid-rock interactions in hydrothermal systems related to mineralization and can be used as a tool for discerning the temperature of crystallization (Panigrahi et al., 2008, Cathelineau, 1988).

3.2 Methodology

Polished thin sections (30 μm thick) were analyzed with a petrographic microscope using transmitted and reflected light. Magmatic plagioclase, biotite and amphibole grains in thin sections were chosen based on petrographic analyses for electron microprobe analysis from least altered rock samples in order to determine their composition. The magmatic minerals selected show interlocking magmatic

texture with other magmatic phases, are commonly euhedral, and show no evidence of having been replaced. Their modal percentages are based on visual estimates.

Forty three chlorite grains from 23 samples were chosen based on their samples' locations relative to the mineralization. Thirty two plagioclase grains from 6 samples were analyzed for Na, Si, Mg, Al, Fe, K, Ca and Sr and the stoichiometry is based on 8 oxygens. Twenty eight biotite grains from 9 samples and 34 amphibole grains from 9 samples were analyzed for F, Na, Si, Mg, Al, Ti, Cu, Mn, Fe, Cl, K and Ca. The majority of the amphibole grains are homogenous except 5 grains that exhibit patchy green replacement texture which was analyzed as well. The chemistry of the amphiboles is compared with the whole rock chemistry, which was analyzed by using X-ray fluorescence (XRF) and Induced Coupled Plasma-Mass Spectrometry (ICP-MS) at the Geoscience Laboratories (Geo Labs) in Sudbury, Ontario. Biotite was also analyzed for Ba. The biotite stoichiometry is based on 22 equivalent oxygen, and the amphibole stoichiometry is based on 23 equivalent oxygen. Chlorite was analyzed for Si, Al, Fe, Cu, Mg, Ca, F, Mn, Na, K and Ti. The stoichiometry of chlorite is calculated and classified based on 28 equivalent oxygen and the Excel spreadsheet developed by Tindle A.G (1993). The chlorite composition is used in geothermometry calculations based on methods developed by Kranidiotis and MacLean (1987) and Cathelineau (1988; see below).

The chosen minerals were analyzed with a Cameca SX50 electron microprobe at the Department of Geology, University of Toronto. The probe conditions for amphibole and biotite were 15 kV acceleration voltage, 20 nA beam current, and 1 μm beam diameter. Operating conditions for plagioclase were 15 kV acceleration voltage, 20 nA beam current and 10 μm beam diameter and for chlorite the conditions were 15 kV acceleration voltage, 34 nA beam current and 1 μm beam diameter. The detection limits for all elements except F are below 0.1 wt.% whereas the detection limits for F is roughly 0.2 wt.%. Percent error is less than 1 for most major elements (Si, Al and Fe) but it is over 50 and up to hundreds of percent error for elements close to their detection limit such as Cu, Sr.

Calibration standards for plagioclase were MgO (Mg), hematite (Fe), $SrTiO_3$ (Sr), albite (Na), anorthite (Si, Ca and Al) and microcline (K). Calibration standards for biotite were kaersutite (Ti), albite (Na and K), anorthite (Ca), sanidine (Ba), tugtupite (Cl), biotite (Fe, Mg, K, Al and Si), chalcopyrite (Cu) and rhodonite (Mn). Calibration standards for amphibole were hornblende (Na, K, Si, Mg, Al, Fe, K, Ca and Ti), tugtupite (Cl), chalcopyrite (Cu) rhodonite (Mn) and fluorite (F).

Calibration standards for chlorite were rutile (Ti), Cu_2O (Cu), albite (Na and K), sanidine (K), craugite (Ca), chlorite (Al, Fe, Si and Mg), rhodonite (Mn) and fluorite (F).

3.3 Results

3.3.1 Petrography of plagioclase, amphibole, biotite and chlorite

The majority of the mineralization at the Hopper property is hosted by an equigranular granodiorite, which is part of an intrusion that ranges in composition from granodiorite to diorite. The main magmatic minerals are plagioclase, hornblende, biotite and the dominant hydrothermal mineral is chlorite (Figure 3.1).

Most of the plagioclase in granodiorite and diorite is euhedral or subhedral, randomly oriented, and crystals range from 100 μm to over 1 mm in length (Figure 3.1A). Grains exhibit albite twinning, zoning (Figure 3.1B) and in some samples plagioclase also exhibits a myrmekite texture (Figure 2.4D). Subhedral grains are generally the result of potassic alteration, which obliterated the previous euhedral boundaries. Plagioclase comprises between 50-75% of the rock by visual estimation.

Hornblende and biotite are the main mafic minerals in the granodiorite. The modal proportion of hornblende varies between 2 and 25 percent of the rock based on visual estimates. In fresh rocks, the hornblende is green, anhedral, subhedral and euhedral (Figure 3.1C). Altered hornblende tends to be more anhedral. The grain size of hornblende ranges between 100 μm and 1.5 mm. It is randomly oriented and some grains exhibit zoning under cross polarized light. Hornblende is altered mainly to chlorite although some grains are altered to actinolite, carbonate, titanite and biotite (Figure 3.1D).

Biotite comprises between 1 and 10 visual percentage of the granodiorite and diorite. It is characterized by anhedral, subhedral and crystals that range from 100 μm to 1mm in length (Figure 3.1E). The biotite is randomly oriented similarly to hornblende and plagioclase. The majority of the biotite is magmatic with the exception of a few samples where the biotite appears to have replaced hornblende. The biotite is altered mostly to chlorite with accessory titanite and epidote-clinozoisite. Minor minerals are quartz, magnetite with ilmenite exolutions and titanite, apatite and zircon as accessory phases.

The main alteration minerals are chlorite, sericite, K-feldspar, carbonate, epidote-clinozoisite, titanite, and less commonly actinolite and secondary biotite. Chlorite is the main alteration mineral

and copper mineralization is closely associated with it (Figure 3.1F) Epidote-clinozoisite also shows some association with the mineralization and it occurs together with the chlorite.

Chlorite was chosen for the analysis due to its close relationship with the mineralization and because the chemical composition of chlorite is known to vary with distance from mineralization (Parry and Downey, 1982). Chlorite has altered 0-100 % of the biotite and hornblende at the Hopper property based on visual estimates, and occurs as both disseminations and along fractures and shear surfaces. The chlorite was analyzed in granodiorite, QFP dykes, mafic dykes and skarn. It is anhedral to subhedral, and the grain size is variable depending on the grain size of the parent mineral.
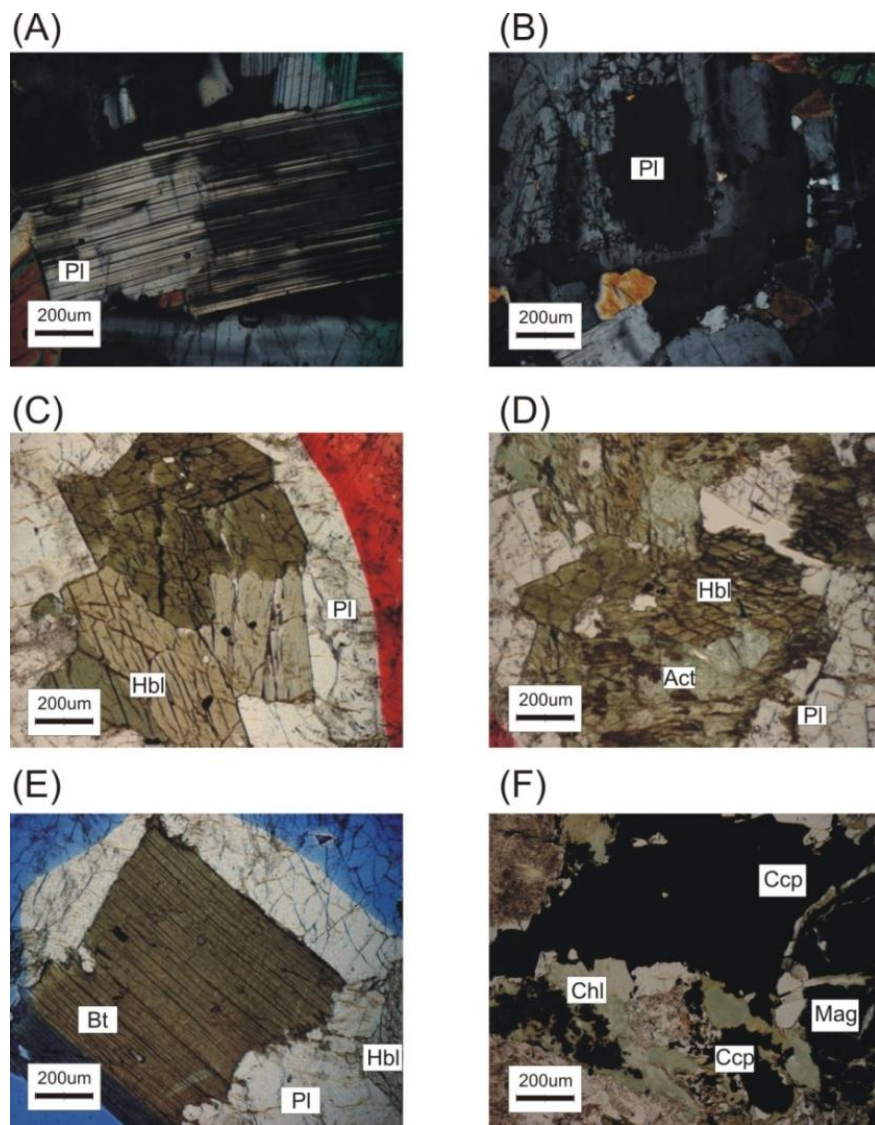
Figure 3.1: Photomicrographs of magmatic and hydrothermal minerals from the intrusion at the Hopper property. A. Magmatic, euhedral plagioclase in a diorite under cross polarized light. B. Magmatic zoned plagioclase in a granodiorite under cross polarized light. C) Magmatic hornblende in granodiorite under plain polarized light. D. Hydrothermal actinolite replacing magmatic hornblende in a granodiorite under plain polarized light. E. Magmatic, euhedral biotite in a granodiorite under plain polarized light. F. Hydrothermal chlorite along a fracture associated with chalcopyrite in a granodiorite under plain polarized light. Pl=plagioclase, Hbl= hornblende, Act= actinolite, Bt= biotite, Chl= chlorite, Ccp= chalcopyrite, Mag= magnetite.

3.3.2 Plagioclase

Plagioclase is a compositional series that includes albite, oligoclase, andesine, labradorite, bytownite and anorthite and ranges between $Na(AlSi_3O_8)$ and $Ca(Al_2Si_2O_8)$ (Deer et al., 1966). Representative data for electron microprobe analysis of plagioclase are presented in Table 3.1 and complete data can be found in Appendix G.

The majority of the plagioclase plots as andesine in both the diorite and granodiorite. The analyses were done as point analyses in random areas in the plagioclase grains because all analyzed plagioclase grains have a homogeneous morphology except one that is zoned. However, plagioclase shows a wide range in composition between An_{33} and An_{51} due to zoning that is not apparent petrographically and due to variations between samples (Figure 3.2). The zoned grain was analyzed using a traverse which resulted with andesine rims (more sodic rims) and labradorite core (more calcic core). The composition of plagioclase including the core of the zoned plagioclase ranges between An_{33} and An_{66} (Figure 3.3).
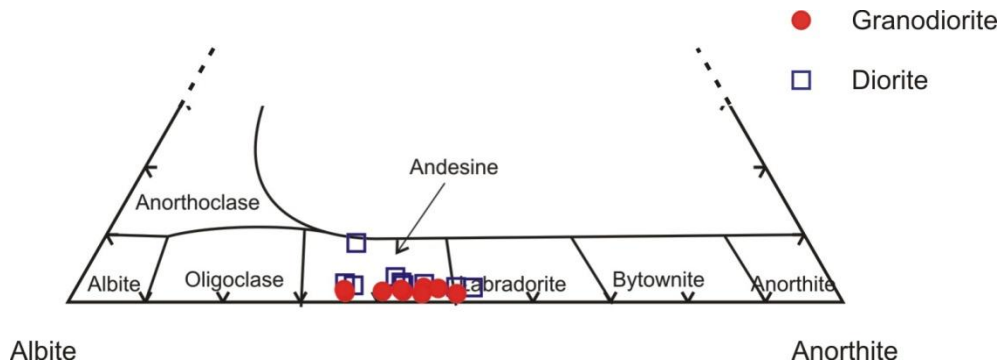
Figure 3.2: Magmatic homogeneous plagioclase classification.
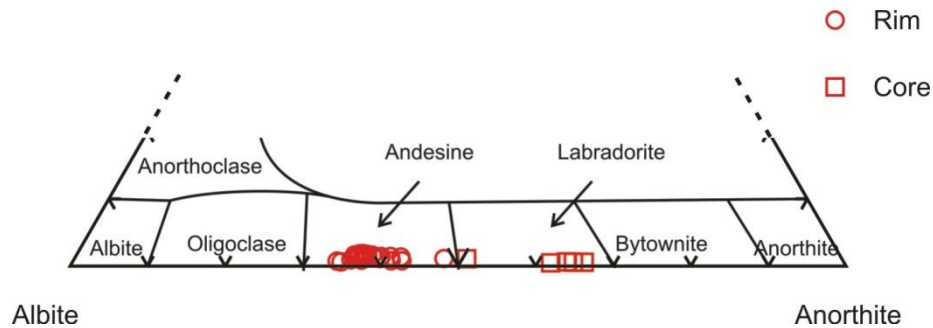
Figure 3.3: Classification of a zoned plagioclase based on a traverse analysis.

Table 3.1: Representative electron microprobe analysis of magmatic plagioclase from the Hopper property (Fe is assumed to be Fe^{3+}). Values represented as n.d are non detectable. Xan=anorthite fraction, Xab=albite fracion, Xor=orthoclase fracion, apfu=atoms per formula unit.

	HB044	HB162	HB222 core
(wt%):			
Na_2O	6.34	7.19	4.29
SiO_2	57.54	58.90	52.12
MgO	n.d	n.d	n.d
Al_2O_3	26.94	25.95	30.62
FeO	0.28	0.16	0.10
K2O	0.44	0.26	0.09
CaO	8.70	7.18	12.67
SrO	n.d	n.d	n.d
Total	100.26	99.61	99.83
Cations based on 8 oxygens (apfu):			
Si	2.576	2.638	2.366
Al	1.421	1.370	1.638
Fe	0.011	0.006	0.004
Tetrahedral Site	4.008	4.013	4.008
Mg	n.d	n.d	n.d
Sr	n.d	n.d	n.d
Ca	0.417	0.345	0.616
Na	0.550	0.624	0.377
K	0.025	0.015	0.005
Xab=Na/(Ca+K+Na)	0.554	0.635	0.378
Xan=Ca/(Ca+K+Na)	0.421	0.350	0.617
Xor=K/(Ca+K+Na)	0.025	0.015	0.005
Alkali Sum	0.992	0.983	0.999
	Andesine	Andesine	Labradorite

3.3.3 Amphibole

The general formula for Ca rich amphibole is $X_{2-3}Y_5Z_8O_{22}(OH)_2$ where X=Ca, Na, K, Mn, Y=Mg, Fe^{+2}, Fe^{+3}, Al, Ti, Mn, Cr, Li, Zn and Z=Si and Al (Deer et al., 1966).

Representative amphiboles in the granodiorite can be classified according to the X_{Mg} Mg/(Mg+Fe$_{total}$) versus Si ratio. The X_{Mg} average is 0.70 apfu (atom per formula unit) with a small range of 0.64-0.75 apfu (Table 3.2), and the Si range is between 6.98 and 7.86 (apfu). This places the amphiboles between Magnesio-Hornblende and Actinolite (Figure 3.4; the complete data can be

found in Appendix G). All grains appear homogeneous and magmatic except five of the amphiboles with actinolite composition that have a patchy replacement texture. In addition, there are 3 amphiboles of actinolite composition with no replacement texture and petrographical characteristics of hornblende.

Table 3.2: Representative electron microprobe analysis of magmatic amphiboles from the Hopper property based on 23 oxygens equivalent. Copper is below detection limit.

	HB184 Actinolitic Hornblende	HB192 Magnesio-Hornblende	HB090 Actinolite
(Wt.%):			
Na_2O	0.84	1.39	0.12
SiO_2	51.29	47.18	54.80
MgO	16.74	13.90	16.48
Al_2O_3	3.90	6.70	0.82
MnO	0.58	0.50	0.44
FeO	11.10	14.06	12.70
K_2O	0.27	0.71	0.03
CaO	12.11	11.62	12.64
TiO_2	0.60	1.33	0.08
F	0.40	0.39	0.00
Cl	0.03	0.16	0.05
H_2O	1.88	1.80	2.08
Sub Total	99.73	99.75	100.25
O=F,Cl	0.17	0.20	0.01
Total	99.55	99.55	100.24

Cations and anions based on 23 oxygens equiv. (apfu):

	HB184	HB192	HB090
Si	7.416	6.984	7.857
Al ^{iv}	0.584	1.016	0.139
Tetrahedral Site	8.000	8.000	7.995
Al ^{vi}	0.081	0.153	0.000
Ti	0.065	0.148	0.008
Fe$_{(total)}$	1.342	1.741	1.523
Mg	3.608	3.067	3.523
Mn	0.071	0.063	0.054
Octahedral Site	5.168	5.172	5.108
Ca	1.877	1.844	1.942
Na	0.235	0.398	0.034
K	0.049	0.135	0.006
Total alkali cations	2.160	2.377	1.981
F	0.182	0.183	0.000
Cl	0.008	0.039	0.012
OH	1.810	1.778	1.988
X_{Mg}	0.729	0.638	0.698
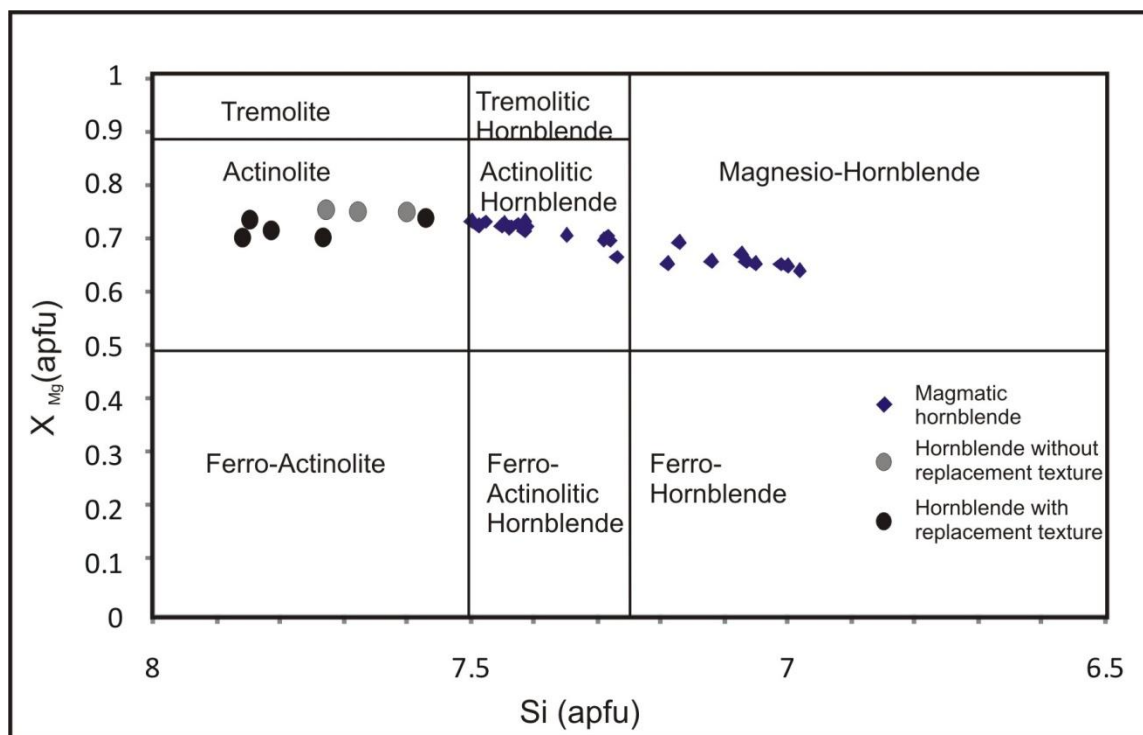
Figure 3.4: Classification of amphiboles from the Hopper property based on 23 oxygens equivalent (modified from Leake, 1978 and Agemar et al, 1999). The figure presents the compositional difference between least altered magmatic amphibole (in diamond) plotted in magnesio-hornblende and actinolitic hornblende fields, amphiboles without replacement texture (in grey) plotted in the actinolite field and hornblende that exhibit replacement texture (in black) plotted in the actinolite field. The amphiboles without the replacement texture petrographically have hornblende characteristics.

The elemental sum of Na and K also ranges widely between 0.04 and 0.53 (apfu). The X_{Mg} shows a positive linear trend versus elemental Si (Figure 3.4) and the sum of Na and K has a negative linear trend with Si (Figure 3.5). The X_{Mg} does not show any spatial correlation with the mineralization possibly due to its small range of values. Copper content in amphiboles was also examined but was below detection limit.
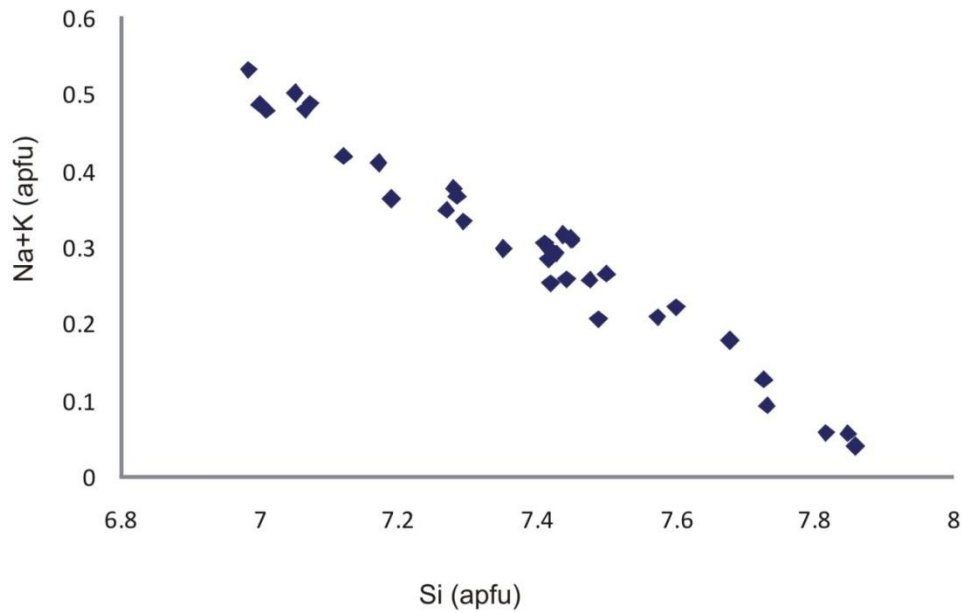
Figure 3.5: Variations of the elemental sum of Na and K versus Si in magmatic amphiboles from the Hopper property based on 23 oxygens equivalent.

Similar to the amphibole mineral chemistry, whole rock data of altered granodiorite and least altered granodiorite also have a positive trend when plotted as X_{Mg} versus Si (Figure 3.6). In addition, the whole rock data show a positive trend when plotted as Na+K versus Si (Figure 3.7) whereas the amphiboles exhibit a negative trend.
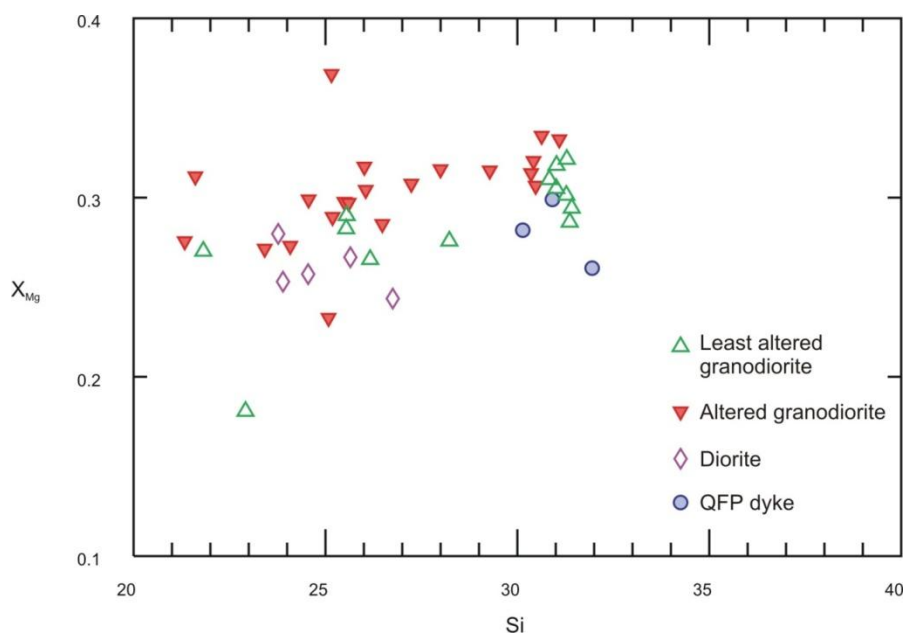
Figure 3.6: Whole rock variations of elemental X_{Mg} versus elemental Si.
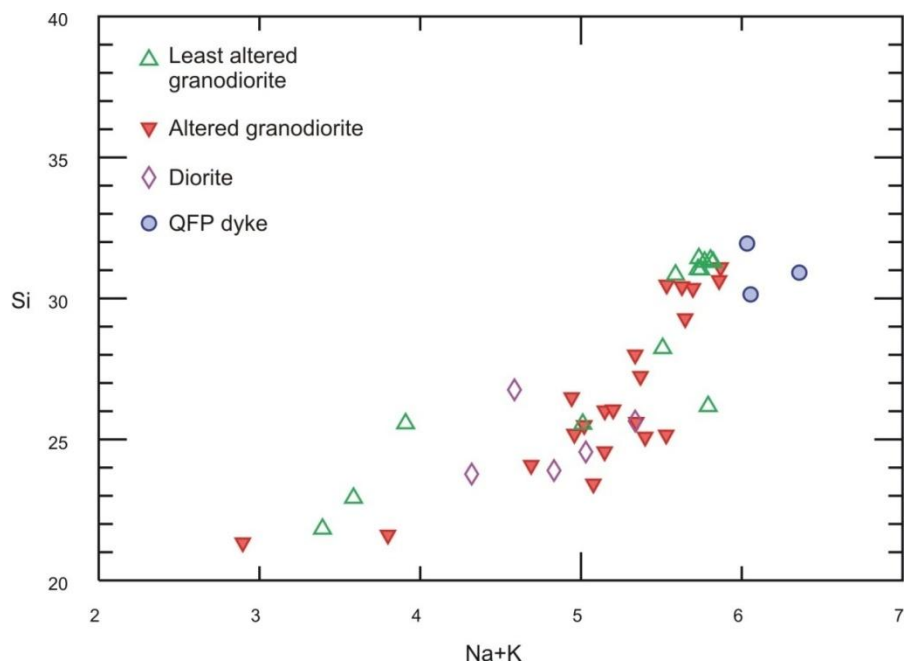
Figure 3.7: Whole rock variations in elemental Na+K versus Si.

3.3.4 Biotite

Biotite has the formula $K_2(Mg,Fe^{+2})_{6-4}(Fe^{+3},Al,Ti)_{0-2}(Si_{6-5}Al_{2-3}O_{20})(OH,F)_4.$ Substitutions for K are Na, Ca, Ba, Rb and Cs. Mn substitutes for Fe^{+2} and Li substitutes for Al. Ti may be substituting for Si or (Fe,Mg) (Deer et al., 1966).

   Biotite that is euhedral and does not show any alteration or replacement textures is interpreted to be magmatic. Twenty nine analyses points in magmatic biotite from the intrusion at Hopper were examined by an electron microprobe in order to characterize the intrusion and compare between the chemistry of biotite from the intrusion in Hopper to known porphyry copper deposits. The samples examined are from both diorite and granodiorite which are interpreted to be part of the same intrusion where only the latter hosts the copper mineralization. Representative biotite compositions are represented in Table 3.3 and complete data can be found in Appendix G.

Table 3.3: Representative electron microprobe analysis of magmatic biotite from the Hopper property based on 22 oxygens equivalent.

	HB072 Granodiorite	HB184 Granodiorite	HB044 Diorite
(Wt %):			
SiO_2	37.97	37.40	36.64
TiO_2	4.04	4.08	4.69
Al_2O_3	13.48	13.43	13.74
FeO (total)	19.60	17.06	16.90
MnO	0.29	0.23	0.07
MgO	13.57	13.83	13.51
BaO	0.30	1.16	0.65
CaO	0.00	0.10	0.05
Na2O	0.08	0.14	0.15
K_2O	8.20	8.52	8.74
F	0.50	0.34	0.49
Cl	0.14	0.14	0.19
H_2O	3.77	3.78	3.67
Sub total	101.94	100.21	99.50
O=F,Cl	0.24	0.17	0.25
Total	101.71	100.04	99.25

Cations based on 22 oxygens equiv. (apfu):

	HB072 Granodiorite	HB184 Granodiorite	HB044 Diorite
Si	5.638	5.640	5.559
$Al^{(IV)}$	2.360	2.360	2.441
Tetrahedral-Site	7.997	8.000	8.000
$Al^{(VI)}$	0.000	0.027	0.015
Ti	0.451	0.463	0.536
Fe (total)	2.434	2.151	2.144
Mn	0.037	0.030	0.010
Mg	3.005	3.108	3.057
Octahedral-Site	5.927	5.779	5.762
Ba	0.017	0.068	0.039
Ca	0.000	0.016	0.008
Na	0.024	0.040	0.045
K	1.554	1.640	1.693
Total alkali	1.595	1.764	1.784
F	0.235	0.161	0.236
Cl	0.035	0.036	0.048
OH	3.730	3.803	3.716
X_{Mg}	0.552	0.591	0.588

Biotite from both diorite and fresh granodiorite plot between phlogopite and annite and exhibit very low Al^{VI} (Figure 3.8).
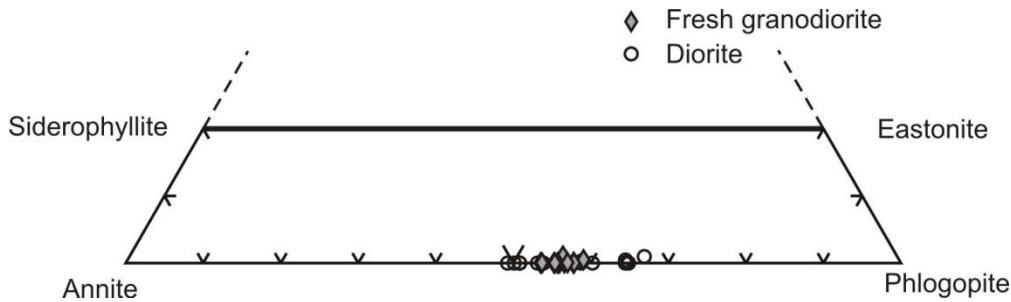
Figure 3.8: Classification of magmatic biotite from fresh granodiorite and diorite. Both types of biotite plot between phlogopite and annite and are very low in Al^{VI}.

Biotite from diorite exhibits a negative trend between X_{Mg} and TiO_2 (Figure 3.9A) with values of X_{Mg} ranging between 0.49 and 0.67 (apfu) and 4-6 wt.% TiO_2 where as the granodiorite has more consistent values ranging between ~4-5 wt.% TiO_2 and 0.53-0.59 X_{Mg} (apfu). The BaO content shows two very distinct behaviors in the diorite and granodiorite (Figure 3.9B). The BaO content in diorite is constant with an average of ~0.65 wt.%, whereas the BaO composition in biotite from granodiorite is more variable (ranging from 0.15 to 1.3 wt.%). Al_2O_3, F and MnO values are variable in both granodiorite and diorite with no clear trend (Figure 3.9C, Figure 3.9D and Figure 3.9E).

Other differences between biotite in granodiorite and diorite are that magmatic biotite from the diorite has a positive trend of X_{Mg} (apfu) versus SiO_2 unlike the magmatic biotite from the granodiorite that appears as a cluster of constant X_{Mg} (apfu) and SiO_2 (Figure 3.9F). Na_2O values are more variable in diorite (0.06-0.36 wt.%) compare to granodiorite values (0.07-0.17 wt.%; Figure 3.9G). Magmatic biotite samples from Hopper show variability in K_2O wt.% values, although the biotite from diorite samples has a negative trend with the X_{Mg} (apfu; Figure 3.9H). Cl values in diorite range between 0.08-0.34 wt.% and increase with decreased X_{Mg} (apfu), whereas biotite from granodiorite has low and consistent Cl values (0.11-0.27 wt.%). Biotite from mineralized granodiorite shows the highest Cl values within the granodiorite samples (Figure 3.9I). These results are discussed further, below.
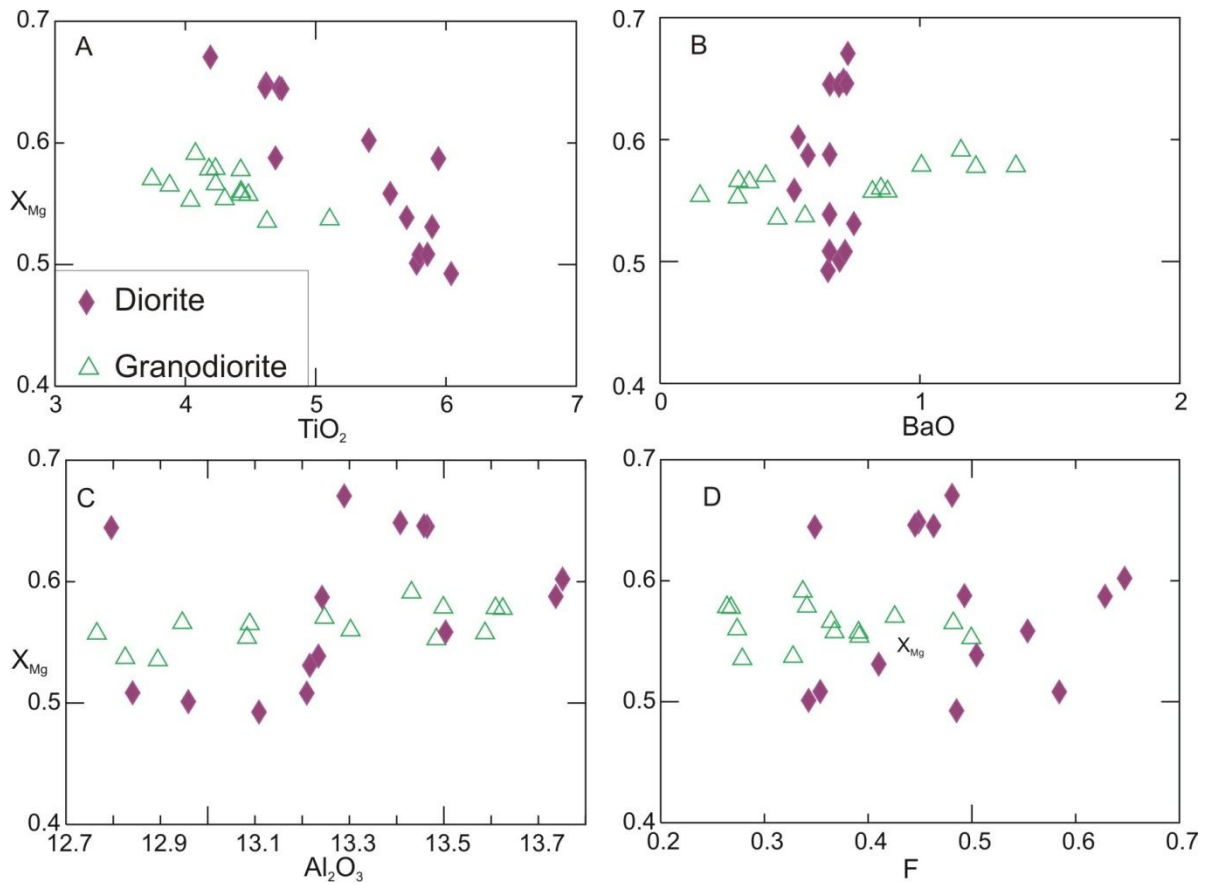
Figure 3.9: Variations of TiO$_2$, BaO, Al$_2$O$_3$, SiO$_2$, MnO, K$_2$O, F, Na$_2$O, Cl (wt.%) versus X$_{Mg}$ (apfu) in magmatic biotite of granodiorite and diorite from the Hopper property.
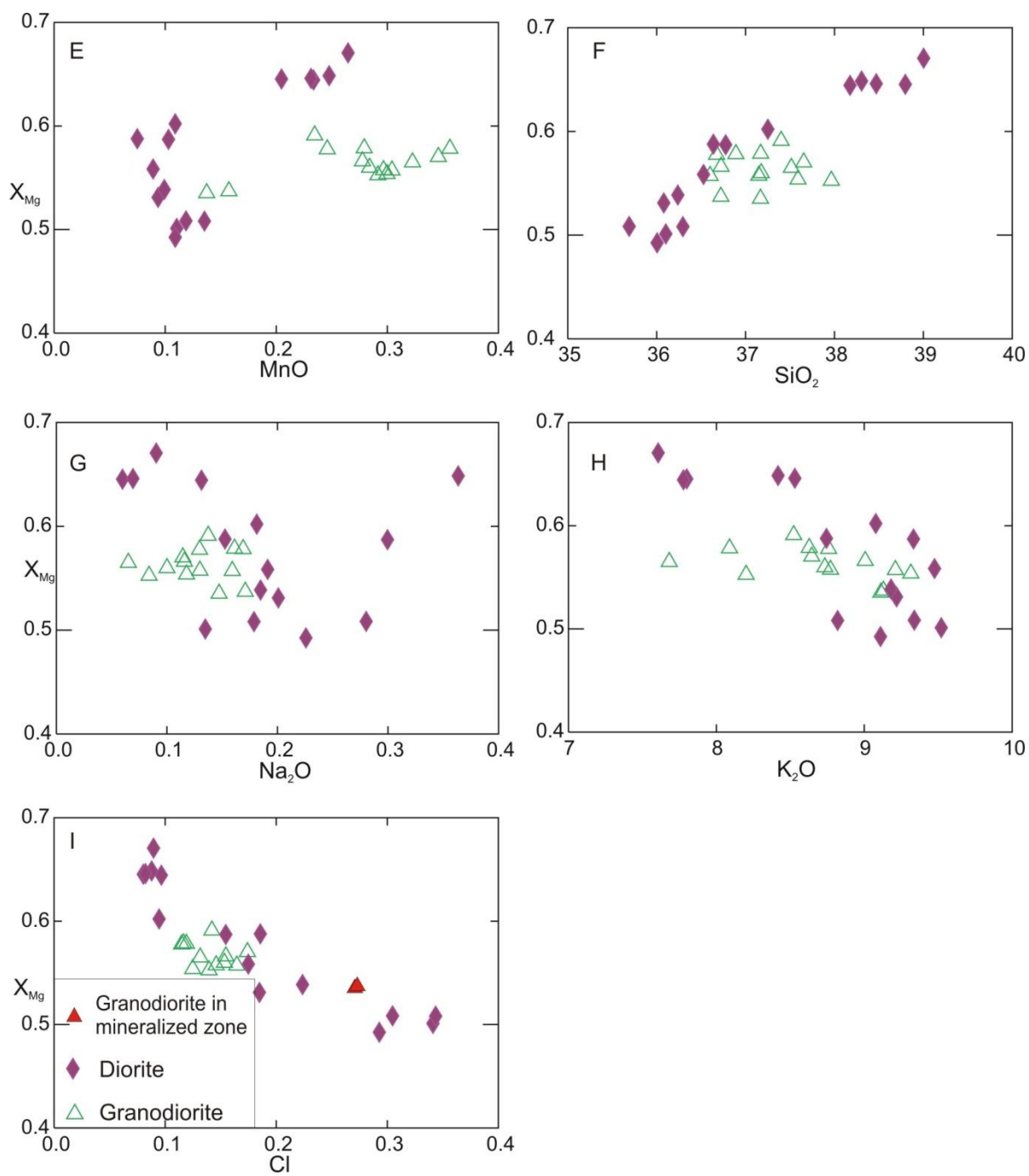
Figure 3.9 (continued…): Variations of TiO₂, BaO, Al₂O₃, SiO₂, MnO, K₂O, F, Na₂O, Cl (wt.%) versus X_Mg (apfu) in magmatic biotite of granodiorite and diorite from the Hopper property.

3.3.5 Chlorite

Chlorite is a clay mineral that is found in various environments. It is also a common alteration product of fluid-rock interaction that either precipitates from solutions or replaces ferro-magnesian minerals in different types of mineralization (Parry and Downey, 1982 and Caritat et al., 1993). The formula of chlorite is $(Mg,Al,Fe)_{12}[(Si,Al)_8O_{20}](OH)_{16.}$

The structure of chlorite can be described as alternating layers of "brucite like" sheets (hydroxide) and "talc like" sheets (2:1 sheets of tetrahedral-octahedral-tetrahedral). The structure of chlorite allows it to have many substitutions and is therefore highly variable in composition (Walshe, 1986 and Caritat et al., 1993). Because of this, the composition of chlorite has been observed to change systematically with distance from ore bodies (e.g., Parry and Downey, 1982). Substitutions occur between Si and $Al^{(IV)}$ in the tetrahedral site and $Al^{(VI)}$, Mg, Fe^{+2} and Fe^{+3} in the octahedral site (in both the "brucite like" and "talc like" layers). Cr, Ti, Ni, Mn, V, Cu and Li can also be present in the octahedral site of chlorite (Deer et al., 1966, Walshe, 1986, and Caritat et al., 1993,). Chlorite is also a useful geothermometer based on variation in its Al^{IV} that is sensitive only to temperature change and less so to other parameters such as pressure and bulk composition (e.g., Cathelineau, 1988, Caritat et al., 1993).

Representative microprobe analysis of chlorite in granodiorite, diorite, mafic dyke, QFP dyke and skarn samples are presented in Table 3.4 and complete data can be found in Appendix G. Chlorite was analyzed for Si, Al, Fe, Cu, Mg, Ca, F, Mn, Na, K and Ti. F, K, Na and Cu were mostly below the limit of detection. The stoichiometry of chlorite was calculated using an Excel spreadsheet developed by Tindle A.G (1993), which is based on 28 equivalent oxygens and classifies the chlorite types. The spreadsheet assumes full site occupancy in order to calculate the content of H_2O, Fe^{2+} and Fe^{3+}.

Table 3.4: Representative electron microprobe analysis of chlorite from the Hopper property based on 28 oxygens equivalent.

	HB119	HB076	HB151A	HB055	HB136
Classification:	pycnochlorite	pycnochlorite	diabantite	ripidolite	brunsvigite
(wt%)					
SiO_2	29.12	29.34	31.53	26.05	27.75
TiO_2	0.03	n.d	0.33	n.d	0.04
Al_2O_3	19.65	19.28	17.46	20.26	20.08
Fe_2O_3	1.50	1.35	2.46	1.09	1.17
FeO	20.46	19.13	18.94	35.85	27.94
MnO	0.68	0.40	0.37	0.20	0.37
MgO	18.00	19.45	19.01	7.53	13.22
CaO	0.08	0.03	0.08	0.05	0.09
Na_2O	0.02	n.d	0.03	0.04	0.07
K_2O	n.d	0.02	0.03	n.d	n.d
F	n.d	n.d	n.d	n.d	n.d
H_2O	11.82	11.85	12.01	11.10	11.57
Sub Total	101.44	100.95	102.31	102.28	102.33
O=F,Cl	0.03	0.03	0.03	0.03	0.02
TOTAL	89.59	89.07	90.27	91.16	90.74

Total Cations based on 28 Oxygens (apfu):
Fe^{2+}/Fe^{3+} and OH are calculated assuming full occupancy

	HB119	HB076	HB151A	HB055	HB136
Si	5.84	5.87	6.21	5.57	5.71
Al iv	2.16	2.13	1.79	2.43	2.29
Tetrahedral Site	8.00	8.00	8.00	8.00	8.00
Al vi	2.51	2.44	2.30	2.70	2.60
Ti	0.00	n.d	0.05	n.d	0.01
Fe^{3+}	0.23	0.20	0.36	0.18	0.18
Fe^{2+}	3.43	3.20	3.12	6.41	4.81
Mn	0.12	0.07	0.06	0.04	0.06
Mg	5.38	5.80	5.58	2.40	4.05
Ca	0.02	0.01	0.02	0.01	0.02
Na	0.02	n.d	0.02	0.03	0.05
K	n.d	0.01	0.02	n.d	n.d
Octahedral Site	11.70	11.73	11.53	11.77	11.79
F	n.d	n.d	n.d	n.d	n.d
OH	15.91	15.90	15.92	15.91	15.95
Total	35.61	35.63	35.45	35.68	35.74
$Fe_{tot}/(Fe_{tot}+Mg)$	0.40	0.37	0.38	0.73	0.55

The majority of chlorite is oxidized and is classified as pycnochlorite. However, it ranges from ripidolite to diabantite based on the classification system of Hey (1954; Figure 3.10).
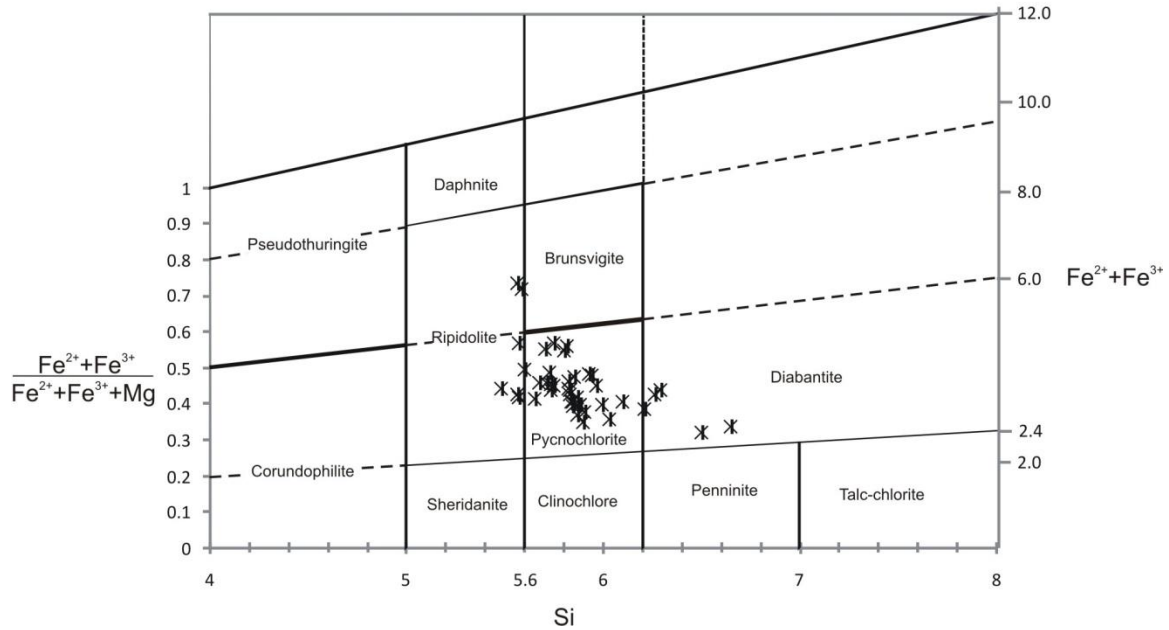
Figure 3.10: Classification of chlorite from the Hopper property (after Hey, 1954).

Fe numbers ($Fe^{tot}/(Fe^{tot}+Mg)$) are randomly distributed at Hopper and vary between 0.32-0.73 apfu where the lowest values are found in a mafic dyke and the highest values are in skarn that is distal to the mineralization. As X_{Fe} decreases Si increases in both mineralized and barren chlorite samples, unlike Al^{iv} which increases as X_{Fe} increases (Figure 3.11A and Figure 3.11B). Chlorite from mineralized granodiorite also shows more consistent and less variable values of Al^{iv} and Si, compared to barren chlorite.
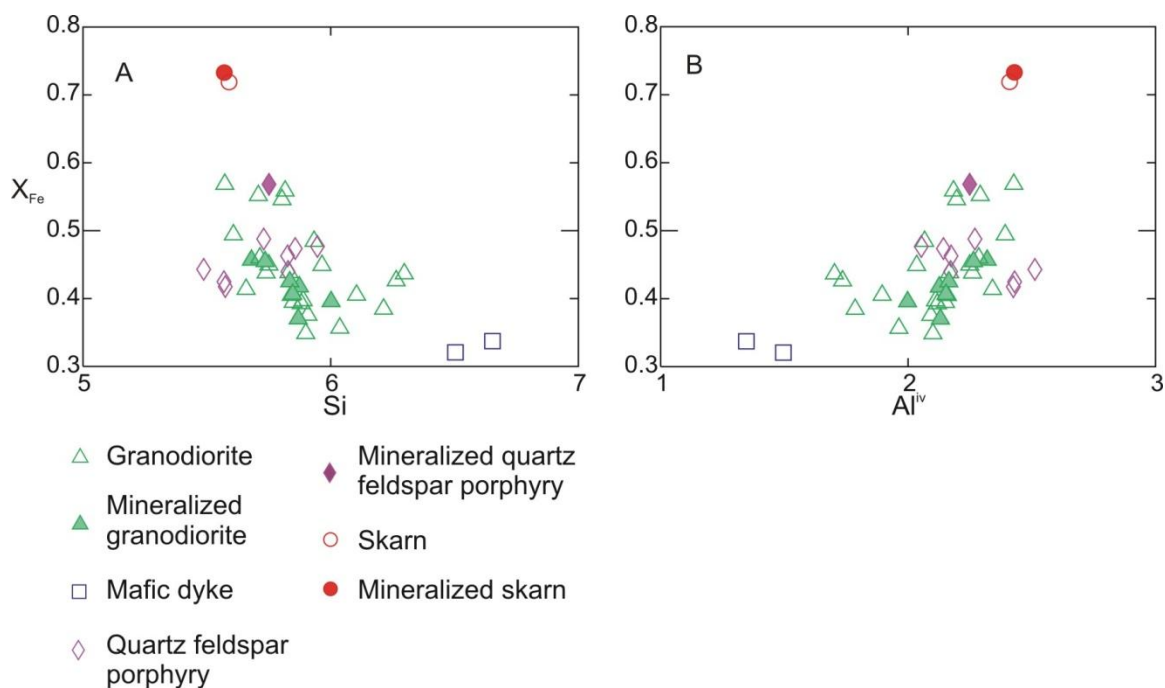
Figure 3.11: Variations in Si and Al ^{IV} (apfu) versus X_{Fe} in chlorite from the Hopper property

Previous studies have shown the composition of chlorite is related to temperature (Cathelineau, 1988, Caritat et al., 1993). Cathelineau (1988) studied the chemistry of chlorite and illite from various geothermal fields as well as fluid inclusions and found that Al in the tetrahedral site of chlorite increases linearly with temperature and that the following equation represents chlorite in many different environments.

Equation 3.1:

T (C˚)= -61.92+321.98*(Al^{IV}) (Cathelineau, 1988)

Using this equation yielded temperatures ranging between 372˚C and 747˚C. The results are summarized in Table 3.5. Both mineralized and un-mineralized granodiorite have a similar range (486˚C to 720˚C). Chlorite from a mafic dyke had the lowest temperatures ranging from 372˚C to 420˚C. Chlorite from mineralized and un-mineralized QFP dykes has a similar range in temperature of 599˚C to 747˚C, the highest temperature calculated. Un-mineralized and mineralized skarn samples yielded high temperatures of 714˚C and 720˚C consecutively. These temperatures are higher than expected for hydrothermal fluids associated with chlorite. Panigrahi et al (2008) for example, found that chlorite crystallized at temperatures ranging between 260˚C and 350˚C.

Table 3.5: Geothermometry results using chlorite (Ccp=chalcopyrite).

Rock type	T˚C (Cathelineau, 1988)	T˚C (Kranidiotis and MacLean, 1987)
Granodiorite	486-720	231-317
Granodiorite+Ccp	581-685	259-298
Mafic dyke	372-420	186-200
QFP dyke	599-747	271-317
QFP dyke+Ccp	662	299
Skarn	714	327
Skarn+Ccp	720	330

The reason for the high temperature in chlorite from the Hopper property could be that the chlorite did not fully replace the biotite and amphibole and was not pure in composition and inherited chemical features of the parent mineral (Cathelineau, 1988).

Kranidiotis and MacLean (1987) proposed a revision of the chlorite geothermometry by Cathelineau (Equation 3.2 and Equation 3.3) that takes in account an ''Al-saturated environment'' as well as the X_{Fe} that is directly related to the composition of the whole rock (Kranidiotis and MacLean, 1987, Caritat et al., 1993). The temperatures of chlorite are calculated according to both Kranidiotis and MacLean (1987) and Cathelineau (1988) and are presented in Table 3.5 and Figure 3.12.

Equation 3.2:

$Al^{IV}c = Al^{IV}+0.7X_{Fe}$

Equation 3.3:

$T(C°)=106Al^{IV}_{C}+18$

The equations by Kranidiotis and MacLean (1987) yielded chlorite temperatures of formation ranging between 186˚C and 330˚C. The highest temperatures were found in chlorite from skarn samples (Table 3.5).
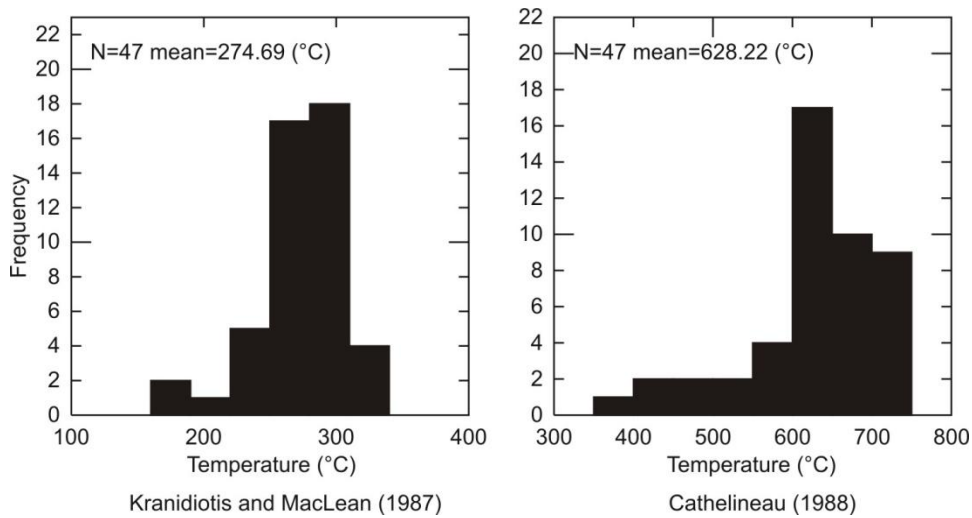
Figure 3.12: Geothermometry data of chlorite based on Kranidiotis and MacLean (1987) and Cathelineau (1988).

3.4 Discussion

The composition of plagioclase ranges between An_{33} and An_{66}, which is similar in part to magmatic plagioclase found in other porphyry copper deposits such as the Bingham porphyry copper deposit with An_{34-37} (Lanier et al., 1978). Other deposits such as the Miduk porphyry with An_{26} (Boomeri et al., 2009) and El Teniente with An_{5-32} (Stern et al., 2007) are less calcic. Fresh plagioclase, from the Ann Mason porphyry copper deposit, ranges from roughly An_{20} to An_{60} (Dilles and Einaudi, 1992), similar to plagioclase from Hopper.

Amphibole from the Hopper intrusion shows a range in composition between magnesio-hornblende and actinolite. Amphiboles with Si of 7.3 (apfu) or less are generally considered magmatic and Si higher than 7.3 (apfu) is not a truly magmatic amphibole (Chivas, 1981). Some actinlolitic amphiboles from the Hopper property have replaced hornblende, and actinolitic amphiboles that do not exhibit this texture were probably formed by re-equilibration at high temperature and are likely pseudomorphs of the original magmatic amphiboles.

There is a positive trend of X_{Mg} vs. Si in magmatic amphiboles from the Hopper property. A similar trend was observed in amphiboles from other granitic rocks of the north Chilean pre-cordillera (Agemar et al., 1999), a region generally known for large porphyry copper deposits such as the Escondida porphyry copper deposit (Garza et al., 2001).

Some authors (e.g., Chivas 1981 and Agemar 1999) have noted that amphiboles are useful in distinguishing between mineralized porphyry copper intrusions and barren intrusions. Mineralized intrusions usually have a wide range of composition placed between magnesio-hornblende to actinolite similar to the amphiboles at the Hopper property.

The results of the biotite analyses from the Hopper property resemble the values of the magmatic biotite from the Casino porphyry copper deposit in the Yukon, the largest porphyry copper occurrence in the Dawson Range west central Yukon (Selby and Nesbitt, 2000). MnO, TiO_2, BaO, and Na_2O in magmatic biotite in granodiorite from Hopper share the same range in composition as magmatic biotite from the Casino deposit reported by Selby and Nesbitt (2000). However, the SiO_2 at Casino is lower by 2 wt.% and some Cl values at Casino are higher than the values observed at the Hopper property. X_{Mg} of magmatic biotite from the Hopper intrusion (0.49-0.67 apfu) is higher than the X_{Mg} from magmatic biotite of the Casino deposit that is ranging from 0.40 to 0.47 (apfu) but is similar to X_{Mg} values of biotite from the propylitic zone in Casino (~0.6 apfu) (Selby and Nesbitt, 2000).

The magmatic biotite from both granodiorite and diorite at Hopper follows the Mg-Cl "avoidance" principle in which higher X_{Mg} values incorporate less Cl then biotite with lower X_{Mg} (Munoz, 1984). This is also in agreement with the results of magmatic biotite from the Casino deposit, published by Selby and Nesbitt (2000). The F values are variable in magmatic biotite in both granodiorite and diorite (0.26-0.65 wt.%) and do not show a linear correlation with X_{Mg}. This is unlike the samples from Casino that have two populations of magmatic biotite based on the F values (F at ~0.2 and 0.35 wt.%; Selby and Nesbitt, 2000). Biotite from both Hopper and Casino does not apply the Fe-F avoidance principle where higher X_{Mg} incorporates more F in biotite. Selby and Nesbitt (2000) suggested two possible reasons why the Fe-F principle is not observed at Casino. One possible explanation is that this principle does not apply to these specific samples. The second possible explanation is that the low X_{Mg} coexists with F rich fluid.

Chlorite in the Hopper property has X_{Fe} ranging between 0.32 and 0.73 (apfu). These values are higher than chlorite in other porphyry copper deposits such as chlorite from the Campana Mahuida porphyry copper deposit for example, where the X_{Fe} ranges between 0.17 to 0.20 (apfu) in the propylitic zone, and is classified as clinchlore (Franchini et al., 2007).

3.5 Conclusions

Mineral chemistry is a useful tool in determining the physio-chemical conditions under which minerals are formed. It can also be used in comparing between minerals associated with different ore deposits. This study found the magmatic plagioclase (An_{33} and An_{66}) has a more calcic composition compared to other porphyry copper deposits. The chemistry of biotite was similar to that of the Casino porphyry copper deposit. Biotites from both areas exhibit Mg-Cl avoidance and have other similar trends and values of MnO, TiO_2, Al_2O_3, BaO, Na_2O, and K_2O. Biotites from both occurrences do not follow the F-Fe avoidance principle according to which high Fe concentrations are associated with low F concentrations and vice versa. Amphiboles from Hopper were found to have similar composition to samples from the Chilean pre-Cordillera where many porphyry copper deposits are located. Amphiboles from both locations range between magnesio-hornblende and actinolite, a trend that is common in mineralized intrusions and is often associated with a porphyry copper type deposits. Overall, X_{Fe} in amphiboles, biotite and chlorite shows no systematic spatial variability relative to the mineralization at Hopper.

Chapter 4

Magmatic and Hydrothermal Titanites: A Geochemical Study of Titanites from the Hopper Property, Yukon Territory

4.1 Overview

The Hopper property lies in the southwestern Yukon, in the Yukon-Tanana terrane. The property contains a granodiorite-hosted copper and molybdenum mineralization that is related to late propylitic alteration and skarn occurrences. Two distinct populations of titanite were identified during a petrographic analysis of samples from the area: magmatic and hydrothermal titanites. Magmatic titanites are euhedral and are in planar contact with other magmatic phases whereas hydrothermal titanites are anhedral and in contact with alteration minerals, which are also related to the mineralization. The Hopper area provides an interesting opportunity to study both populations in the same system.

Electron microprobe analyses of titanites show that Ti is substituted by Al+Fe+Nb+Zr+Ce+Y and that the hydrothermal titanites are Ti-rich compared to the magmatic ones. Titanites from skarn in the same area have higher values of Al+Fe+Nb+Zr+Ce+Y and lower Ti values. Trace-element compositions of titanites (rare earth elements and transition metals) were also analyzed using Laser Ablation Inductively Coupled Plasma Mass Spectrometer (LA-ICP-MS). Geothermometry calculations based on Zr content suggest magmatic titanites were formed at 660-900° C, most of which show higher high field strength elements (HFSE) values than the hydrothermal ones. However, the REE (rare earth elements) signatures of most magmatic and hydrothermal titanites overlap. Most hydrothermal titanites are also characterized by higher values of Cu and Cr than the magmatic ones. Surprisingly though, the magmatic titanites have more elevated Mo values than the magmatic titanites, indicating the mineralization could be ortho-magmatic. The trace element compositions of titanites could be influenced by zoning and hydrothermal titanites could also be influenced by the composition of the parent mineral and the mobility of the elements.

4.2 Introduction

Titanite is a common accessory mineral in many different systems including different metamorphic, igneous and hydrothermal rocks (Mazdab et al., 2007; Hayden et al., 2008). Titanite's formula is $CaTi(SiO_4)(O,OH,F)$ (Deer et al., 1966) and its structure consists of chains of TiO_6 octahedra and

SiO$_4$ tetrahedra. This forms a large 7-fold coordinated polyhedra that is occupied by Ca (Harlov et al., 2006 and Cempírek et al., 2008). Calcium can be substituted by Na, Ba, Sr, Y and REE. Titanium can be replaced by Sn, Zr, Si, Al, Fe^{2+}, Fe^{3+}, Sb, V, Nb, Ta and a vacancy (denoted as □). SiO$_4$ can be replaced by Ti and □ or O, OH or F (Deer et al., 1966, Harlov et al., 2006, Broska et al., 2007 and Cempírek et al., 2008). The Substitutions are controlled by the cation size and charge. The most common substitutions observed are Al and Fe^{3+} for Ti. Al and Fe^{3+} can also be part of a coupled substitution with 5^{+} cations such as Nb (Al^{3+}+Nb^{5+}= 2Ti^{4+}; Broska et al., 2007 and Cempirek et al., 2008). Another common substitution is with Al and F that can be found in coupled substitution for Ti. Al and Fe^{3+} commonly replace Ti at low temperatures, whereas Al and F typically substitute for Ti at high temperatures and pressures (Broska et al., 2007, Tropper et al., 2002). The concentration of Al-Ti in titanite is also influenced by the bulk composition (Tropper et al., 2002). The ability of titanite to hold significant concentrations of REE and HFSE, makes it an important indicator accessory mineral (Hayden et al., 2008). In addition, titanite can be used for age dating and estimating temperature of formation based on U/Pb and Zr concentrations respectively (Hayden et al., 2008).

Previous studies have shown differences between titanites forming in different environments such as magmatic, metamorphic, hydrothermal and diagenetic (Mazdab et al., 2007, Broska, 2007). However, reports of compositions of different titanite types from the same location are rare. This study examines chemical differences between hydrothermal and magmatic titanites of the same hydrothermal system. Geochemical differences between the two populations have the potential to be used as indicators in exploration.

4.3 Geological Setting

The Hopper property is located in the Yukon Tanana terrane between the Denali and Tintina faults, in southwest Yukon. The Hopper property contains copper and molybdenum mineralization that is hosted by a granodiorite, interpreted by Johnston and Timmerman (1997) to be part of the Ruby Range batholith. This granodiorite intruded the Aishihik metamorphic suite in the Yukon Tanana terrane. The Aishihik metamorphic suite at Hopper consists of mainly brown quartzite, and small discontinuous lenses of marble and skarn, which are part of the Finlayson assemblage of the Yukon Tanana terrane.

The Jurassic Aishihik batholith and plutonic suite is composed of mostly granodiorite or quartz monzodiorite and intruded the Aishihik metamorphic suite at 186±2.8 Ma, followed by the emplacement of a pink quartz monzonite of the Long Lake Plutonic Suite at 185.6 +2.0/-2.4 Ma

(Johnston et al., 1996). During the Cretaceous and Tertiary periods the volcanic rocks of the Carmacks Group erupted and the Ruby Range plutonic suite, plutons and dykes of the Nisling Range alaskite and mount Creedon volcanic suite were all emplaced into the Aishihik metamorphic suite (Johnston et al., 1996). According to Johnston (1993), the margins of the Ruby Range batholith are 68-90 Ma and the core is about 58 Ma. The Hopper intrusion is granodiorite and diorite in composition and is intruded by younger quartz porphyry and mafic dykes.

4.4 Analytical Techniques

Scanning Electron Microscope (SEM) back scatter imaging and SEM cathodoluminescence were used to examine 33 titanites in six samples for zoning. This is to help determine if point analysis or transects are necessary in the following analyses. Sixty-one titanites were analyzed in 23 polished thin sections (30 μm) with a Cameca SX50 electron microprobe at the Department of Geology, University of Toronto, in order to compare the compositions of magmatic and hydrothermal titanites. The probe conditions were 20 kV acceleration voltage, 65 nA beam current, and 1 μm beam diameter. The titanites were analyzed for the concentrations of Si, Ti, Al, Fe, Ca, Na, Zr, Mn, Nb, Y, Ce and Cu. These elements are known to substitute Ca and Ti in titanites. The counting time was 20 seconds for Si, Fe, Na, Mn, Ce, Cu, 30 seconds for Y, Ca, Nb, 40 seconds for Zr, and 50 seconds for F, Ti and Al.

The average detection limits for all elements except F are below 0.1 wt. % where as the detection limit for F is 0.25 wt %. The percent error of titanite is less than 10 for F, Si, Ti Al, Fe and Ca and varies from 10's to 100's percent error for Na, Zr, Mn, Nb, Y Ce and Cu. The calibration standards for titanite were Cu_2O (Cu), $MnTiO_3$ (Mn), $NaNbO_3$ (Nb, Na), sphene (Ca, Si, Ti, Al and Fe), $ZrSiO_4$ (Zr), fluorite (F), YPO_4 (Y) and $CePO_4$ (Ce).

In addition, 70 titanites in 13 polished thick sections (200 μm) were analyzed using Laser Ablation Inductively Coupled Plasma Mass Spectrometer (LA-ICP-MS) in order to determine the concentration of the REE as well as the transition metals in the titanites. The samples were analyzed at the Department of Earth Sciences, Laurentian University, Sudbury, Ontario by LA-ICP-MS consisting of a New Wave Nd:YAG 213 nm laser coupled to a quadrupole Thermo X II series ICP-MS. The operating conditions were 30 μm spot size at a repetition rate of 10 Hz. The laser speed was 10 μm/s for long lines and 5 μm/s for short lines and the energy density was kept constant at roughly 8 J/cm^2. The beam width was 5 ns out of analysis time ranging between 60 and 80 seconds including 30 seconds background acquisition time. The ablated material was then carried from the ablating cell to the ICP-MS in a He atmosphere and Ar mixed carrier gas before it entered the ICP-MS. Synthetic

glass standards NIST612 and NIST611 that contain trace element abundances of about 40-50 ppm were used as the external standard for the trace element analysis and Ca was used as an internal standard with a value of 27.5 wt.% from previous analyses with the electron microprobe. The data acquisition is based on a peak jump mode with dwell time as specified in Table 4.1.

The detection limit of Sc, V, Cr, Mn, Co, Ni, Cu, Zn, Ga, Ge, As, Zr, Nb, Mo, Sn, Sb, Hf, Ta, W, Tl and Pb are less than 20 ppm. As and P have a detection limit of ~170 ppm. The detection limit of the REE could not be calculated but is assumed to be between 20 and 30 ppb based on the Nd detection limit value.

Table 4.1: Dwell time of the LA-ICP-MS.

Elements	Dwell Time (ms)
Ca, Sr, V, Mn, Ga, Ge, As, Nb, Sn, Hf	10
Sc	15
Y, La, Ce, Th, U, P, Cr, Co, Ni, Cu, Zn, Mo, Sb, Pb	20
Eu, Tb. Zr, Pr	25
Ta, W, Tl	30
Nd, Sm, Gd, Dy, Ho, Er, Tm, Yb, Lu	40

The titanites were analyzed by two parallel transects on each grain (one for the REE and one for the transition metals) unless the grain was smaller than 100 μm and/ or had inclusions, in which case the two transects were made on two separate titanites that are within up to 1 mm apart and of the same occurrence. The analyses were done in transects because zoning was observed in some titanites with back scatter SEM. Transition metals were analyzed in a separate transect due to the dwell time effect.

4.5 Results

4.5.1 Compositional variations in hydrothermal and magmatic titanites

Petrographic analysis indicated two populations of hydrothermal and magmatic titanites, based on their association with either magmatic or alteration minerals. The magmatic titanites are coarse grained, 100 μm to 1 mm across, euhedral and have planar contacts with other magmatic phases such

as hornblende and plagioclase (Figure 4.1A). One magmatic titanite crystal also contains a chalcopyrite inclusion suggesting the chalcopyrite is ortho-magmatic in origin (Figure 4.1B and Figure 4.1C). Hydrothermal titanites are anhedral, more fine-grained and range from 10 to 500 μm across. The anhedral titanites share their boundaries with alteration minerals such as chlorite and epidote-clinozoisite (Figure 4.1D), in contrast to magmatic titanite. Many hydrothermal titanites are in direct contact with chalcopyrite (Figure 4.1D and Figure 4.1E), and two hydrothermal titanite grains have chalcopyrite inclusions. There are also indirect relations between hydrothermal titanites and chalcopyrite based on the observation that both the chalcopyrite and the hydrothermal titanites occur together with chlorite and epidote-clinozoisite.
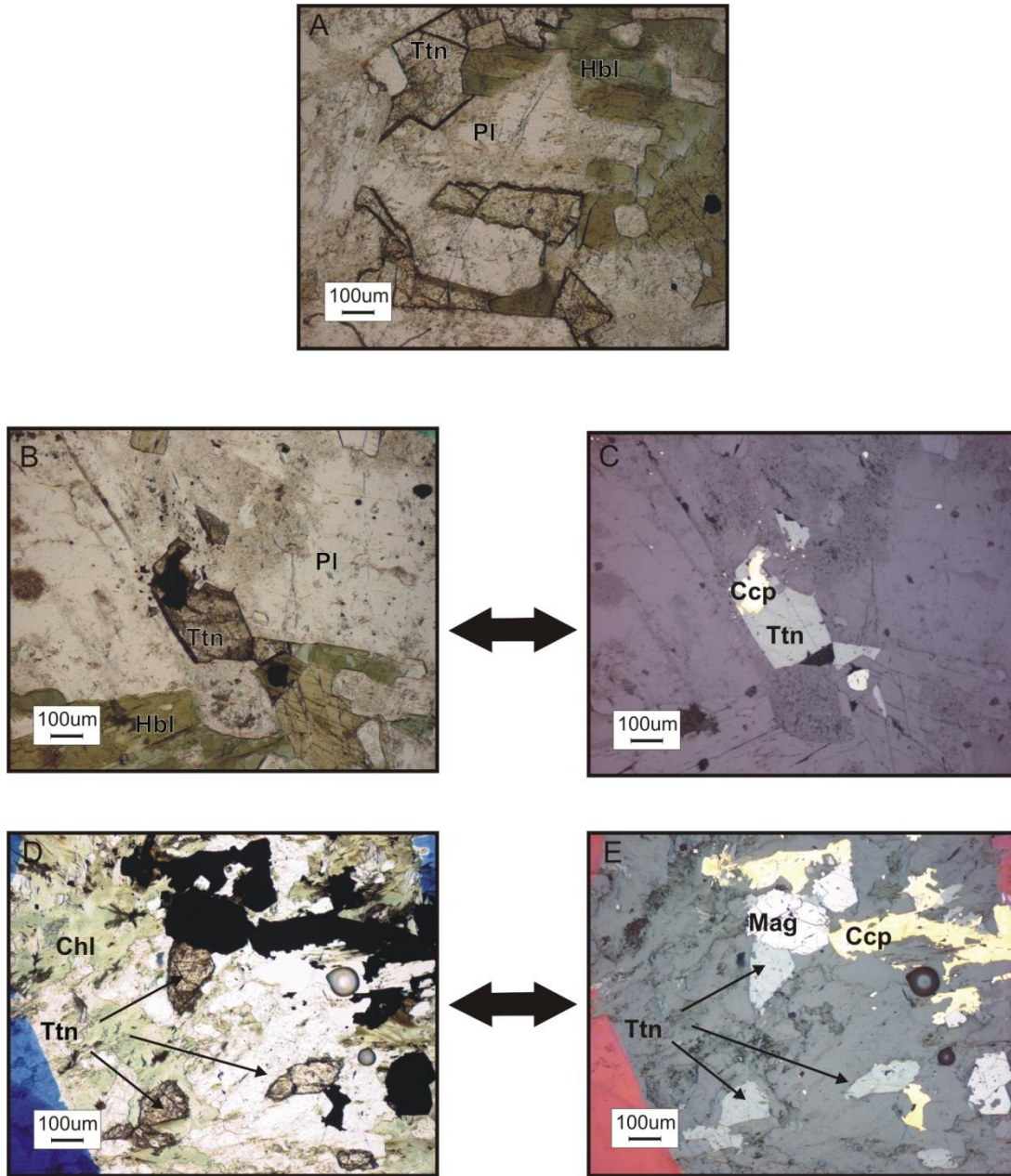
Figure 4.1: Photomicrographs of magmatic and hydrothermal titanites. A. Magmatic titanites under plain polarized light. B. A magmatic titanite with a chalcopyrite inclusion under plain polarized light. C. The same magmatic titanite with a chalcopyrite inclusion under reflected light. D. Hydrothermal titanites with chlorite and chalcopyrite under plain polarized light. E. The same hydrothermal titanites with chlorite and chalcopyrite under reflected light. Ttn=titanite, Hbl=hornblende, Pl=plagioclase, Ccp=chalcopyrite, Chl=chlorite, Mag=magnetite.

Cathodoluminesence using SEM did not show any zoning in the titanites. However, back scattered imaging using the SEM did reveal patchy zoning in most magmatic and hydrothermal titanites and oscillatory zoning in two magmatic titanites (see below).

Common substitutions in a single site in titanite include (AlNb)→2Ti and common substitutions in two sites are Na, Nb→CaTi, REE, Al→CaTi, Al(F, OH)→Ti, and □+(OH)$_4$→SiO$_4$ (Cempirek, 2008). Due to these common substitutions, the titanites are plotted as Ti versus the sum of Al, Fe, Nb, Zr, Ce and Y which yields a negative linear slope indicating there is a substitution between Ti and Al+Fe+Nb+Zr+Ce and Y. Representative titanite compositions are presented in Table 4.2 and complete data can be found in Appendix G.

Table 4.2: Representative electron microprobe analysis of titanites from the Hopper property based on 3 cations.

	HB055 skarn	HB119 Magmatic	HB140 Hydrothermal
(Wt.%):			
F	0.85	n.d	0.43
SiO_2	31.23	31.19	31.87
TiO_2	36.32	34.13	36.41
Al_2O_3	2.35	2.15	1.46
$FeO_{(total)}$	1.21	1.84	1.32
CaO	27.76	26.82	27.63
Na_2O	0.02	n.d	n.d
ZrO_2	n.d	0.10	0.04
MnO	n.d	0.12	0.06
Nb_2O_5	0.11	0.11	0.08
Y_2O_3	0.05	0.04	0.04
Ce_2O_3	0.20	0.76	0.44
Total	100.10	97.27	99.78

Calculations are based on 3 cations

	HB055	HB119	HB140
Si	1.016	1.039	1.040
Tetrahedral Site	1.016	1.039	1.040
Al	0.090	0.084	0.056
$Fe_{(total)}$	0.030	0.046	0.032
Ti	0.888	0.855	0.894
Nb	0.002	0.002	0.001
Zr	n.d	0.002	0.001
Ti Site	1.010	0.989	0.985
Mn	n.d	0.003	0.002
Na	0.002	n.d	n.d
Ca	0.967	0.958	0.967
Y	0.001	0.001	0.001
Ce	0.002	0.009	0.005
Ca Site	0.972	0.971	0.975
F	0.088	n.d	0.045

Most of the magmatic titanites (represented as squares in Figure 4.2) show lower values of Ti atom per formula unit (apfu) compared to hydrothermal titanites (represented as triangles in Figure 4.2). Hydrothermal titanites also exhibit a lower apfu sum of Al, Fe, Nb, Zr, Ce and Y. Titanites from skarn samples (represented as circles in Figure 4.2) have higher apfu values of Al, Fe, Nb, Zr, Ce and Y, and are lower in Ti. In Figure 4.3, the hydrothermal titanites have variable values of Al in contrast to the relatively constant Al values of the magmatic titanites. In addition, titanites from skarn have relatively high values of Al and F compared to most of the hydrothermal titanites.

Figure 4.2: Variations in the sum of Al, Fe(total), Nb, Zr, Ce and Y (apfu) vs. Ti (apfu) in magmatic titanites (squares), hydrothermal titanites (triangles) and skarn titanites (circles). Different petrographic characteristics are given different colors.

Figure 4.3: Variations in F (apfu) vs. Al (apfu) in magmatic titanites (squares), hydrothermal titanites (triangles) and skarn titanites (circles). Different petrographic characteristics are given different colors.

Magmatic and hydrothermal titanites analyzed with the LA-ICP-MS yielded variable results for the majority of the elements analyzed mainly due to variability in concentrations between different titanite grains that have the same petrographical characteristics and due to zoning. In magmatic titanites, Ti, Ga and Tl are less than 10 ppm. Tb, Tm, Lu, Sc, Co, Cu, Zn, Ge, As, Sb and Pb range from less than 10 to 10's of ppm. Eu, Ho, Er, Yb, Cr, Mo, Hf and W range from less than 10 to 100's of ppm. Ta ranges from less than 10 ppm to 1000's of ppm. Ni, Sn, Sr, Sm, Gd and Dy range from 10's to 100's of ppm. Y, Nb, Pr, and Th range from 10's to 1000's of ppm. La Mn, Zr, V, U and Nd vary from 100's to 1000's of ppm and Ce, varies from 100's to 10000's of ppm.

In hydrothermal titanites, Ce ranges from less than 10 ppm to 10000 ppm. Mn ranges between the 100's ppm to 10000 ppm, V ranges between the 100's and a 1000 ppm and Sn and Cr range between 10's ppm to 100's ppm. Eu, Tb, Ho, Er, Yb, Th, Sc, Co, Ga, Ta and W range from less than 10 ppm to 100's of ppm. La, Pr, Nd, Sm, Gd, Dy, Zn and Zr range from less than 10 ppm to 1000 ppm. Ni, U, and Y are between the 10's and 1000's ppm. Cu, Ta, Mo, Tm, Lu, Ge, As, Sb, Hf, and Pb have the lowest concentrations, ranging between less than 10 ppm to 10's of ppm. Tl concentration is below 10 ppm and Sr concentration is in the 10's of ppm range.

Hydrothermal titanites have Cu values ranging from 6 to 61 ppm and Mo ranging between 0 and 88 ppm. Copper in magmatic titanites ranges between 7-30 ppm and Mo ranges between 8 and 222 ppm (much higher than the values in hydrothermal titanites). Skarn titanites have copper values ranging between 10 and 88 ppm and Mo between 2 and 18 ppm. The hydrothermal and magmatic titanites that are enriched in copper or molybdenum are not petrographically different from titanites with lower concentrations of these elements. V varies from 736 ppm to 5732 ppm in hydrothermal titanites compare to magmatic titanites with V ranging from 916 to 1634 ppm. Co, Ni and Sb in hydrothermal titanite was found to be 10's to 100's of ppm higher than magmatic titanites.

Most magmatic titanites and skarn titanites are more enriched in high field strength elements (HFSE) including Zr, Hf, Nb, Ta, Y, Sc and P, compared to the hydrothermal titanites (Figure 4.4). Light rare earth elements (LREE) and heavy rare earth elements (HREE) are variable in concentrations in both hydrothermal and magmatic titanites (Figure 4.4A and Figure 4.4B consecutively). Cr is another element that is higher in most hydrothermal and skarn titanites compared to the magmatic ones and Zr is higher in most magmatic and skarn titanites compared to hydrothermal ones (Figure 4.5). This observation is in agreement with a study done by Piccoli et., al (2000) who also found elevated concentrations of Cr in hydrothermal titanites.
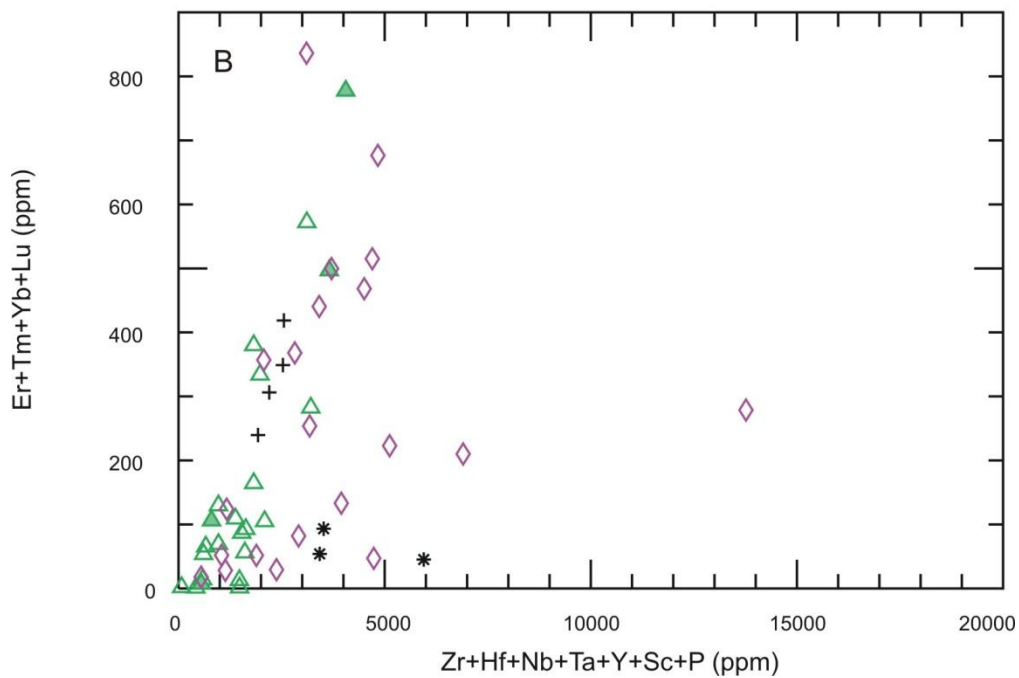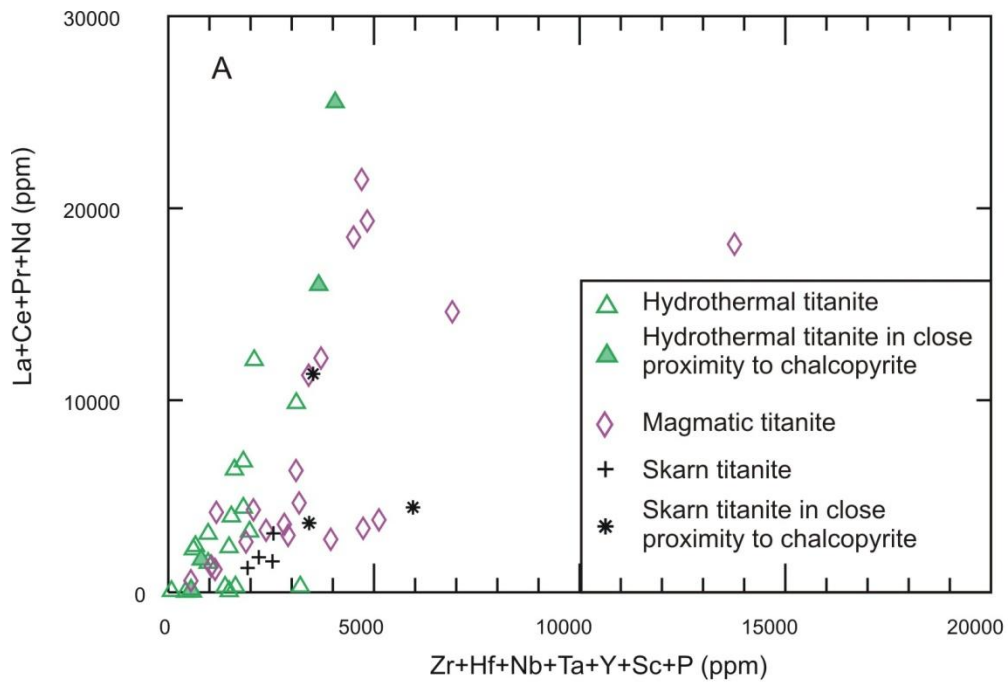
Figure 4.4: Variations between LREE (A) and HREE (B) and HFSE in magmatic, hydrothermal and skarn titanites.
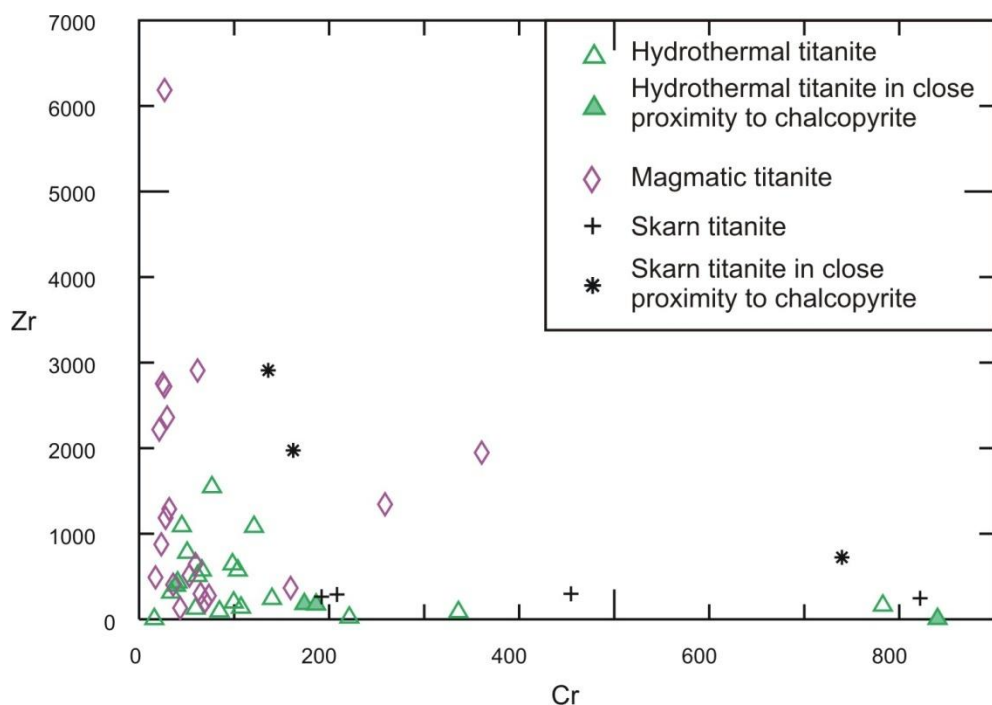
Figure 4.5: Variations between Zr and Cr in magmatic, hydrothermal and skarn titanites.

Analyses of REE in titanites with LA-ICP-MS show that magmatic and hydrothermal titanites have similar REE abundance (Figure 4.6). The magmatic titanites and most of the hydrothermal titanites have a similar REE pattern, characterized by a moderate negative slope (Figure 4.6A), except the trend between La and Ce is positive in hydrothermal titanites and it is negative in magmatic titanites (Figure 4.6A and Figure 4.6B). However, when plotted as La/Ce versus the sum of Zr and Nb (Figure 4.7) there is an overlap between hydrothermal and magmatic titanites unlike other studies such as Li et al. (2010) where there is a much larger difference in values.

The majority of the magmatic titanites also have a positive Eu anomaly and the hydrothermal titanites have either a positive or negative Eu anomaly (Figure 4.6B). One sample exhibits a stronger positive Eu anomaly than the rest of the titanites. Five hydrothermal titanites are two to three orders of magnitude more depleted in REE than the rest of the hydrothermal titanites (Figure 4.6C). Petrographically, there is no difference between hydrothermal titanites of variable REE signatures and there is also no difference in the REE signatures between hydrothermal titanites in close proximity (within 200 μm) to chalcopyrite and those that are not in close proximity to chalcopyrite. Skarn titanites in close proximity to chalcopyrite have a moderate negative slope with a positive Eu anomaly

85

unlike titanites from barren skarn that have a flat REE pattern and a minor negative Eu anomaly (Figure 4.6D).
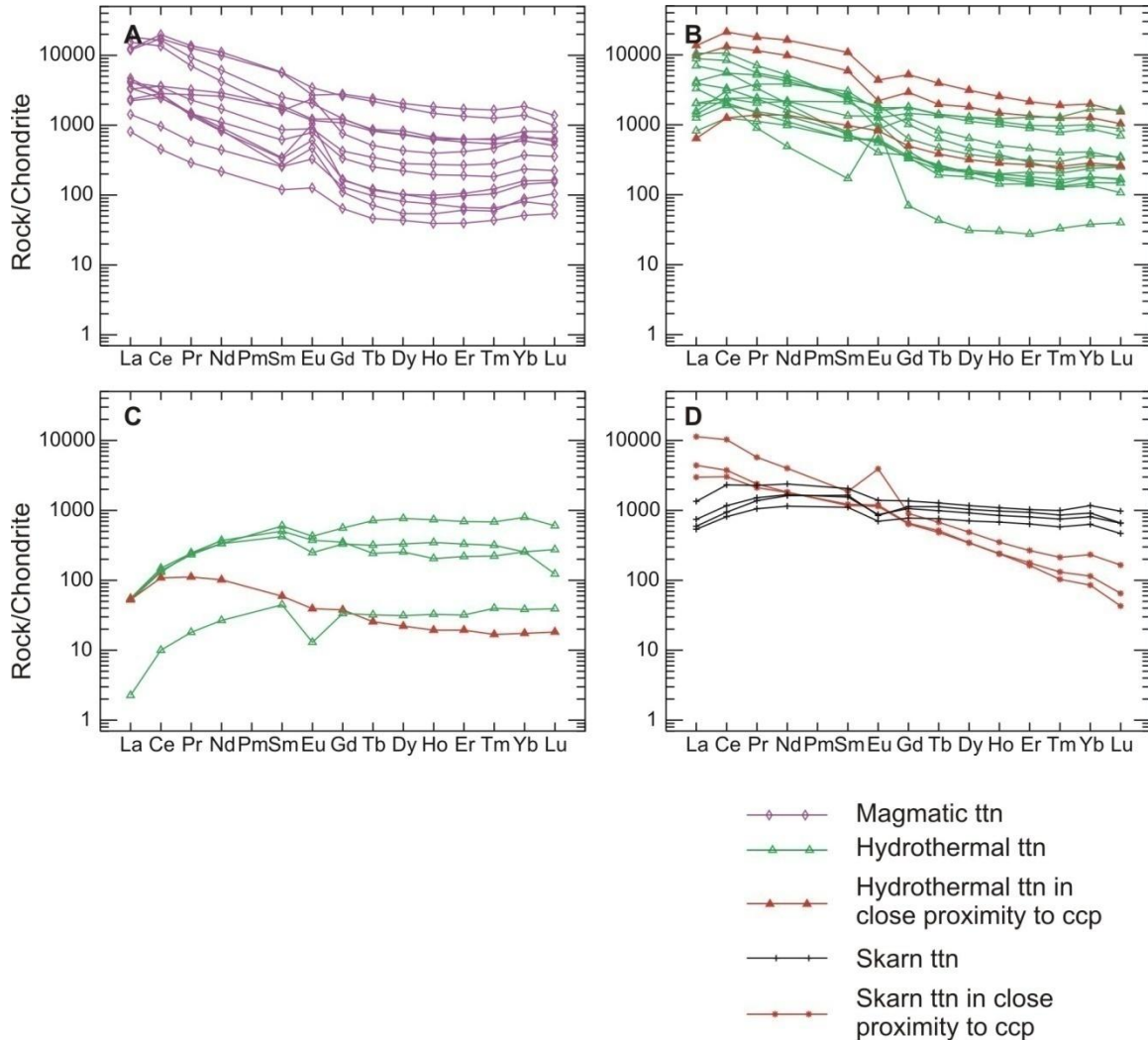
Figure 4.6: Trace element spider diagrams of magmatic, hydrothermal and skarn titanites. Hydrothermal and skarn titanites are also subdivided into barren titanites and titanites within close proximity (200 μm) to chalcopyrite (ccp). A. Magmatic titanites, B. Hydrothermal titanites, C. Hydrothermal titanites with low trace element abundances, D. Skarn titanites. Normalized values of chondrite are from Sun and McDonough (1989).
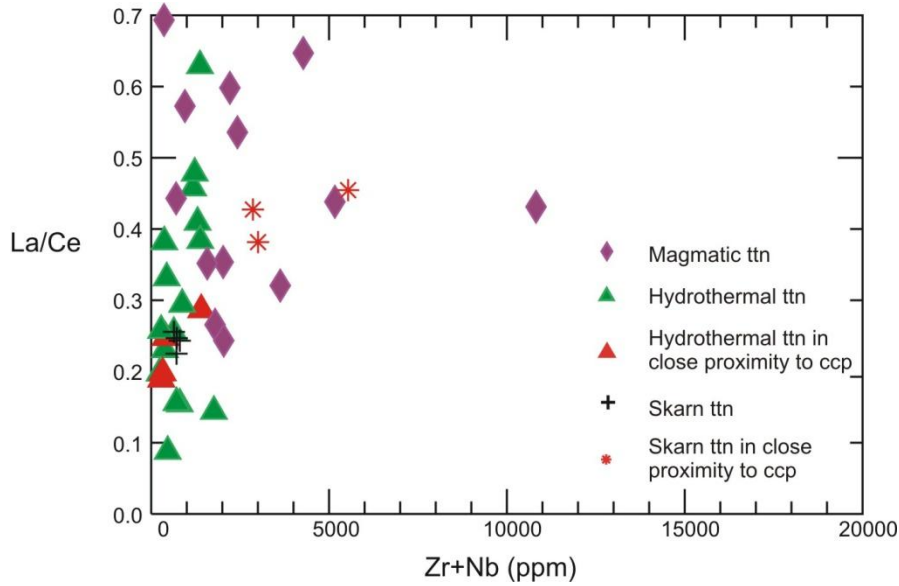
Figure 4.7: Variations between La/Ce and Zr+Nb (ppm) in magmatic, hydrothermal and skarn titanites.

Analyses using SEM back scattered imaging and LA-ICP-MS indicated that some hydrothermal and magmatic titanites have patchy zoning and two magmatic titanites show oscillatory zoning (examples for oscillatory zoning in magmatic titanite and patchy zoning in hydrothermal titanite are presented in Figure 4.8A and Figure 4.8B, respectively). This is due to specific elements that have preferentially been incorporated in a specific growth surface (Hayden et al., 2008). The zoning is characterized by high values of REE and transition metals at either the core, the rims or as more complex zoning patterns. Figure 4.9 shows variations in the trace elements concentrations along transect of the magmatic titanite from Figure 4.8A. Higher concentrations are indicated by higher counts per second (cps). The elements U, Nd, La, Pr, Ce and Th were found to be higher in the core and rim of the grain (Figure 4.9).

87
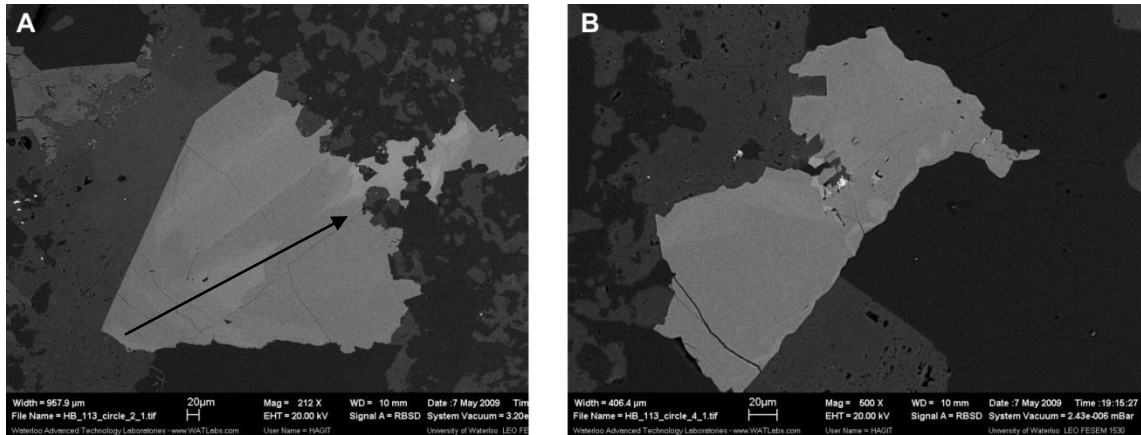
Figure 4.8: Photomicrographs of zoned titanites with back scattered electron imaging using SEM. A. Titanite exhibiting an oscillatory zoning. B. Titanite exhibiting a patchy zoning.
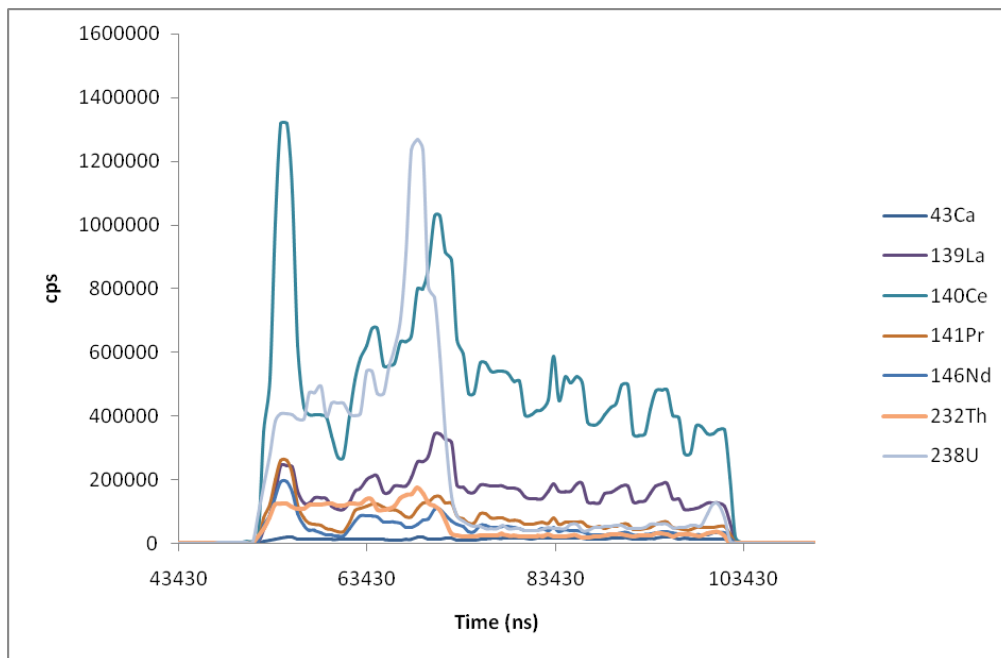
Figure 4.9: Variations in counts per second (cps) along a transect in titanite with oscillatory zoning (Figure 4.8A), ns=nano seconds.

4.5.2 Geothermometry

Due to the sensitivity of Zr concentrations to temperature and pressure and its insensitivity to the presence of REE and F-Al substitutions, results from the LA-ICP-MS analyses can further be used to

calculate the temperature (within ±20 degrees) of titanite formation based on thermobarometer experiments completed and published by Hayden et al (2008). Hayden et al (2008) based the thermobarometer on the amount of Zr substitution for Ti. They crystallized synthetic titanite from a solution with quartz, rutile and zircon (although rutile does not necessarily have to be present to apply the thermobarometer). The analytical conditions were pressure ranging between 1 and 2.4 GPa and 800˚C-1000˚C. The Zr content in the synthetic titanite was analyzed with an electron microprobe. These experiments showed log-linear relationship between the Zr concentration and pressure and temperature (Hayden et al., 2008):

Equation 4.1:

$$\log(Zr_{ttn}) = 10.52(\pm 0.10) - \frac{7708(\pm 101)}{T(K)} - 960(\pm 10)\frac{P(GPa)}{T(K)} - Log(aTiO2) - \log(aSiO2)$$

Where, $aTiO_2$ and $aSiO_2$ both equal 1.

The thermobarometer was applied to natural samples of known pressure and temperature and yielded similar results. The equation used is based on high temperature and pressure experimental data and is applicable to natural titanites that formed between 600˚-1000˚C (Hayden et al., 2008). The data presented in Figure 4.10 for magmatic titanites show the temperature of magmatic titanites is variable and dependent on the pressure. Johnston (1993) observed cordierite and andalusite in the contact metamorphic aureole of the Ruby Range intrusion, suggesting that the pressure in the area was 2 kbar (0.2 GPa) or less. For such pressure, the temperature of magmatic titanite ranges from 660˚C to 900˚C.
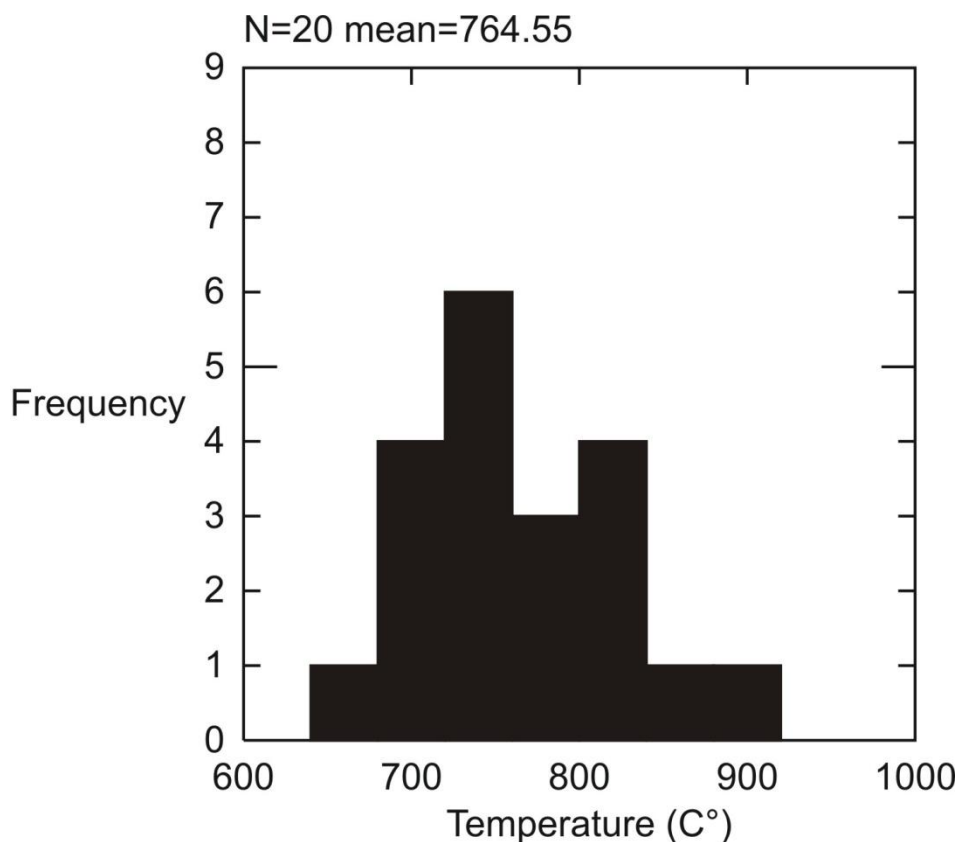
Figure 4.10: Geothermometry results of magmatic titanites based on Zr content and a pressure of 0.2 GPa.

Hayden et al. (2008) recorded Zr values of an order of magnitude difference in the same titanite grain from core to rim. Therefore it is essential not to include the peak concentration which is indicative of a disequilibrium state. Including such a zone would result in overestimates of the temperature of crystallization (Hayden et al., 2008).

Hydrothermal titanites are assumed to have formed in much lower temperature of ~350°C (Zaluski et al., 1994), and the lower Zr concentrations qualitatively agree with this assumption. However, due to the lower Zr concentrations, the equation used to calculate temperature for magmatic titanites is not applicable for the hydrothermal titanites.

4.5.3 Age dating of the Hopper intrusion

4.5.3.1 Analytical techniques

An attempt was made by Balz Kamber and Thomas Ulrich at Laurentian University, at Sudbury, Ontario, to age date titanite from the Hopper intrusion by analyzing it with LA-ICP-MS for U, Th and Pb ratios in order to determine the age of the intrusion and the copper mineralization associated with the hydrothermal titanites (Kamber and Ulrich, 2009; See Appendix B). The LA-ICP-MS used is a XSeriesII ICP MS that consist of a small orifice cone of about 0.5 GHz ppm^{-1} sensitivity. The ablation was done in ultrapure He with a 213 nm New Wave laser probe. The beam diameter was 40 μm and the laser power was maintained low (10Hz repetition rate and 15J cm^{-2}; Benn and Kamber, 2009).

One sample (HB226A) was selected to age date the intrusion, based on its lack of alteration, veins and fractures. In order to date the alteration associated with the mineralization, two highly altered and mineralized granodiorite samples were selected (HB076 and HB140) based on their lack of veins, fractures and their titanite and zircon content known by petrographic observations. Hydrothermal titanites were analyzed due to their close association with the mineralization which could potentially yield the age of mineralization. The samples were crushed, milled and passed through a Wilfley table to separate the heavy minerals. These were processed with a magnetic separator. Zircons and titanites in each sample were mounted on tape and epoxy and were analyzed with a 40 μm beam diameter. A total of 113 data point of zircons and 75 data points of titanites were analyzed in the three samples (Kamber and Ulrich, 2009).

4.5.3.2 Results

According to Kamber and Ulrich (2009) neither hydrothermal nor magmatic titanites could be used for age dating using this method due to low radiogenic Pb (206, 207 and 208) contents, a high common Pb (204) concentration and trace mercury which adds to Pb (204). Because of the low $^{206}Pb/^{204}Pb$ ratio, accurate dates could not be obtained.

4.6 Discussion

The purpose of this research was to identify geochemical differences between magmatic and hydrothermal titanites that are closely associated the copper mineralization at the Hopper property. These differences could possibly allow using titanite as an indicator mineral as an exploration tool. Geochemical results are based on the assumptions that titanites in planar contacts with magmatic

phases such as feldspars, biotite and hornblende are magmatic, and titanites in contact with secondary minerals such as chlorite are hydrothermal titanites. A possible reaction for the formation of hydrothermal titanite is suggested by Broska et al. (2007) as:

Anorthite+Ti bearing Annite=Titanite+Epidote+chlorite+Quartz

Preliminary results obtained from analyzing titanites of the different populations with an electron microprobe show substitutions occurred between Ti and Al, Fe, Nb, Zr, Ce and Y based on the negative linear trend in Figure 4.2. The lower values of Ti in magmatic titanites indicate more substitutions for Ti by other elements occurred in the magmatic titanite population compared to hydrothermal titanites. Magmatic titanites are also distinct from the hydrothermal ones according to their constant Al values compared to the variable values of Al in hydrothermal titanites Figure 4.3.

This differentiation between titanite populations is possible due to its excellent element coupled substitutions. Al and Fe^{3+} often substitute in the octahedral site of titanite and REE substitute for Ca (Broska et al., 2007). The most common substitutions are Al, Fe^{3+} and F for Ti. This result is in contrast to a study done by Horie et al. (2008), in which the alteration titanite associated with low temperature chlorite alteration had lower Ti concentrations and higher in Ca, Fe and Al compared to the magmatic titanite.

The results from the LA-ICP-MS show overall similar abundances in REE with a few minor variations in chemistry between hydrothermal titanites and magmatic ones. Hydrothermal titanites have a positive Ce anomaly that does not occur in magmatic titanites. In addition, Magmatic titanites have higher HFSE concentrations (Figure 4.4). This is because HFSE tend to be highly incompatible and are therefore less mobile. Hydrothermal titanites also incorporate more copper than the magmatic ones because they are associated with the same fluids as the mineralization. Surprisingly, magmatic titanites consist of much more elevated Mo concentrations compared to hydrothermal titanites. This suggests that the mineralization at Hopper could be ortho-magmatic in origin.

Unlike other studies that showed little to no detectable REE concentrations in hydrothermal titanites (Piccoli et al., 2000), most hydrothermal titanites in this study have comparable values to magmatic titanites, except a few grains that show concentrations of two to three orders of magnitude less than the magmatic ones (Figure 4.6C). This is in agreement with other studies showing that hydrothermal titanites have lower concentrations of REE compared to magmatic titanites and higher values of Cr and Zn (Piccoli et al., 2000). Although, Piccoli et al (2000) also noted elevated values of

Mn in hydrothermal titanite grain, whereas in this study the Mn values were lower for hydrothermal titanites. It is possible the high REE contents in hydrothermal titanites reflect a low water/rock ratio.

Hydrothermal, magmatic and skarn titanites are mostly characterized by a negative slope that they inherit from the bulk rock that is an enriched calc-alkaline rock and a few skarn titanites have a flat slope (Figure 4.6). Some of the trends are characterized with minor positive or negative Eu anomalies and some with sharper anomalies. There are a few reasons for the various Eu anomalies observed in both the hydrothermal and magmatic titanites. Positive anomalies can occur when Eu changes its oxidation state from Eu^{3+} to Eu^{2+}, this in turn allows Eu^{2+} to substitute for Ca^{2+} and form a positive anomaly in hydrothermal titanites indicating a reducing environment (Horie, 2008). Horie et al (2008) found that negative Eu anomalies are related to magmatic titanites, in contrast to this study where magmatic titanites exhibit positive anomalies of Eu. The hydrothermal titanites appear to have replaced hornblende, biotite, and plagioclase. The composition of the primary mineral could affect the composition of the following alteration mineral replacing it. Titanite replacing plagioclase was observed to have a sharp positive Eu anomaly whereas titanite replacing biotite and hornblende show both minor positive and minor negative Eu anomalies. In addition, titanite replacing plagioclase has lower overall abundances in REE compared to titanite replacing biotite and hornblende.

A few hydrothermal titanites have two to three orders of magnitude lower values of REE. This could be a result of different fluid chemistry or partitioning of REE in other minerals such as apatite or monazite or due to zoning in the titanites. Mazdab et al (2007) noted that the cores of titanites can vary dramatically in their REE values and signatures compared to other zones in the same grains related to metamorphism. Many of the hydrothermal and magmatic titanites overlap in REE signature. A few reasons could explain the resemblance between the two populations. First, Piccoli et al. (2000) noted that hydrothermal titanites commonly grow on existing primary magmatic titanites, which is difficult to detect. Therefore, it is possible the composition of some of the hydrothermal titanites is influenced by previous composition of magmatic titanites and so the REE values of the hydrothermal titanite appear to be much higher than their true concentration. Second, it is likely the REE in this system are not as mobile as they are in other hydrothermal systems resulting in a smaller difference between hydrothermal and magmatic titanites. Third, a low water/rock ratio can also be the result of high REE content.

Zr concentrations in titanite can be used as a thermobarometer. Results indicated the magmatic titanites were formed between 660˚C and 900ºC at 0.2 GPa (Figure 4.10). The high temperature

values are in agreement with previous studies (e.g. Eastoe and Eadington, 1986) that calculated temperatures of a granodiorite of up to 1000˚C from fluid inclusions. Johnston (1993) found the intrusion of the Ruby Range batholith to be associated with low pressure and high temperature (>500˚C), which is also in agreement with the geothermometry calculations presented in this study. This could be a true representation of the temperatures of the intrusion, indicating the intrusion is heterogeneous in terms of temperature, unless these titanites have re-equilibrated. The variability could also be a result of zoning in the titanites.

4.7 Conclusions

The Hopper intrusion contains two populations of titanites: magmatic and hydrothermal. Magmatic titanite is recognized by its planar contacts with other magmatic phases such as feldspars, hornblende and biotite. Hydrothermal titanite is anhedral and is intergrown with alteration minerals such as chlorite.

Electron microprobe analysis and LA-ICP-MS indicates a few minor differences in composition between the two populations. Both populations allow coupled substitutions between Ti and Al, Fe, Nb, Zr, Ce and Y. The hydrothermal titanites in this system are characterized by a higher Ti and lower Al, Fe, Nb, Zr, Ce and Y contents, in contrast to other system where magmatic titanites have higher Ti. Hydrothermal titanites also have higher Cu and Cr and lower values of HFSE compared to magmatic titanites although they also have lower Mo values compare to magmatic titanites suggesting the mineralization is ortho-magmatic. The total REE content in both titanite populations in this system is similar except a few hydrothermal titanites that have much lower REE content. It is possible there is only a small difference in REE content between the two populations because the hydrothermal titanites have overgrown magmatic ones and therefore their REE composition is higher than true hydrothermal titanites. It is also possible there is only a small difference in REE content because of zoning or because the REE are not as mobile as in other hydrothermal systems. Geothermometry calculations suggest the temperature of the magmatic titanites for 0.2 GPa varies from 660˚C to 900˚C. In summary, hydrothermal titanites can be distinguished from magmatic ones based on the HFSE and metal contents.

Chapter 5
Conclusions

5.1 Conclusions of the three chapters

The copper and molybdenite mineralization at the Hopper property is hosted in a granodiorite intrusion interpreted by Johnston and Timmerman (1997) to be part of the Ruby Range batholith. Age dates of the Hopper intrusion indicate that it was emplaced between 76.0±1.1 Ma and 83.7±1.9 Ma (Kamber and Ulrich, 2009), which is consistent with this interpretation. The mineralization is closely related to propylitic alteration and it occurs as disseminations and along fractures and shear surfaces.

The occurrence at Hopper resembles a porphyry type mineralization in a few ways. First, the Hopper intrusion is of late Cretaceous age like other deposits found in the Yukon. Most porphyry deposits are related to subduction zones and have a calc-alkaline affinity as found at Hopper. Second, the mineral chemistry of amphiboles and biotites is also similar to other porphyry occurrences. Biotites exhibit the "Mg-Cl avoidance" principle and have the same range of concentrations of MnO, TiO_2, Al_2O_3, BaO, Na_2O and K_2O as found in biotites from the Casino porphyry copper deposit. Amphiboles from Hopper also resemble amphiboles from other porphyry systems due to their range in composition from magnesio-hornblende to actinolite. Investigations of hydrothermal and magmatic titanites from the intrusion revealed they are distinct from one another based on their HFSE and metal content. Third, S isotopes from the Hopper mineralization have values indicating a magmatic source as expected in a porphyry system. However, due to the association of the mineralization with propylitic alteration, desilicification and a loss in potassium, it is concluded the mineralization has been remobilized. Another possible model is that the mineralization is shear related and is much younger than the intrusion.

5.2 Recommendations for future research

Additional analyses are recommended in order to further determine the nature of the fluids associated with the mineralization, the origin of the mineralization, and the conditions under which they were formed such as temperature and pressure. A fluid inclusion study is ideal for determining the composition and origin of the fluids as well as the temperature and pressure under which they were trapped, although none of the samples examined in this study contained suitable fluid inclusions.

Additional age dating of the mineralization could answer the question as to whether or not it is the same age as the intrusion and if the ortho-magmatic model is likely. This may be possible by using hydrothermal titanites that are closely associated with the mineralization. Using a different method other than LA-ICP-MS such as TIMS or SIMS could be more successful at dating the titanites and placing time constraint on the mineralization.

References

Agemar, T., Wörner, G., and Heumann, A., 1999, Stable isotopes and amphibole chemistry on hydrothermal altered granitoids in the Northern Chilean Precordillera: a limited role for meteoric water?, Contrib Mineral Petrl, v. 136, p. 331-344.

Appleyard, E. C., 1980, A preliminary metasomatic assessment of laminated siltstones at the Silverfields Mine, Cobalt, Ontario; Grant 70, p. 1-10 in Geoscience Research Grant Programme, Summary of Research, 1979-1980, edited by E. G. Pye, Ontario Geological Survey, MP93, 262 p.

Appleyard, E. C., 1990, Mass balance corrections applied to lithogeochemical data in mineral exploration, In Beck, L. S. and Harper, C. T. (eds), Modern exploration techniques, Special Publication - Saskatchewan Geological Society, v. 10, p. 27-40.

Appleyard, E. C., and Memarian, M., 2003, SOMA- A program for calculating mass exchange in metasomatic and altered rocks, University of Waterloo, unpublished document.

Benn, K., and Kamber, B. S., 2009, In situ U/Pb granulite-hosted zircon dates, Kapuskasing structural zone, Ontario: A late Archean Large Igneous Province (LIP) as a substrate for juvenile crust, Journal of Geology, v. 117, p. 519-541.

Boiron, M. C., Cathelineau, M., and Trescases, J. J., 1989, Conditions of gold- bearing arsenopyrite crystallization in the Villeranges basin, Marche- Combrailles shear zone, France: A mineralogical and fluid inclusion study, Economic Geology, v. 84, p. 1340-1362.

Boomeri, M., NaKashima, K., and Lentz, D. R., 2009, The Miduk porphyry Cu deposit, Kerman, Iran: A geochemical analysis of the potassic zone including halogen element systematics related to Cu mineralization processes, Journal of Geochemical Exploration, v. 103, p. 17-29.

Broska, I., Harlov, D., Tropper, P., and Siman, P., 2007, Formation of magmatic titanite and titanite–ilmenite phase relations during granite alteration in the Tribeč Mountains, Western Carpathians, Slovakia, Lithos, v. 95, p. 58-71.

Caritat, P. D., Hutcheon, I., and Walshe, J. L., 1993, Chlorite geothermometry: a review, Clays and Clay Minerals, v. 41, p. 219-239.

Cathelineau, M., 1988, Cation site occupancy in chlorites and illites as a function of temperature, Clay Minerals, v. 23, p. 471-485.

Cempírek, J., Houzar, S., and Novák, M., 2008, Complexly zoned niobian titanite from hedenbergite skarn at Písek, Czech Republic, constrained by substitutions $Al(Nb,Ta)Ti_{-2}$, $Al(F,OH)(TiO)_{-1}$ and $SnTi_{-1}$, Mineralogical Magazine, v. 72, p. 1293-1305.

Chivas, A. R., 1981, Geochemical evidence for magmatic fluids in porphyry copper mineralization, part 1: Mafic silicates from the Koloula igneous complex, Contributions to Mineralogy and Petrology, v. 78, p. 289-403.

Colpron, M., Nelson, J. L., and Murphy, D. C., 2006, A tectonostratigraphic framework for the pericratonic terranes of the northern Canadian Cordillera, In: Colpron, M., and Nelson, J. L., eds., Paleozoic evolution and metallogeny of the pericratonic terranes at the ancient pacific margin of north America, Canadian and Alaskan Cordillera, Geological Association of Canada, special paper 45, p.1-23.

Colpron, M., Nelson, J. L., and Murphy, D. C., 2007, Northern Cordillera terranes and their interactions through time, GSA Today, v. 17, p. 4-10.

Deer, W. A., Howie, R. A., and Zussman, J., 1966, An introduction to the rock forming minerals, Longman, London, 528 p.

Deksissa, D. J. and Koeberl, C., 2004, Geochemistry, alteration and genesis of gold mineralization in the Okote area, southern Ethiopia, Geochemical Journal, v. 38, p. 307-331.

Dilles, J. H. and Einaudi, M. T., 1992, Wall-rock alteration and hydrothermal flow paths about the Ann-Mason porphyry copper deposit, Nevada- A 6 Km vertical reconstruction, Economic Geology, v. 87, p. 1963-2001.

Eastoe, C. J., Eadington, P. J., 1986, High-temperature fluid inclusions and the role of the biotite granodiorite in the mineralization at the Panguna porphyry copper deposit, Bougainville, Papua New Guinea, Economic Geology, v. 81, p. 478-483.

Erdmer, P., and Mortensen, J. K., 1993, A 1200-km-long Eocene metamorphic-plutonic belt in the northwestern Cordillera: Evidence from southwest Yukon, Geology, v. 21, p. 1039-1042.

Franchini, M., Impiccini, A., Meinert, L., Grathoff, G., and Schalamuk, I. B. A., 2007, Clay mineralogy and zonation in the Campana Mahuida porphyry Cu deposit, Neuquén, Argentina: Implications for porphyry Cu exploration, Economic Geology, v. 102, p. 27-54.

Garza, R. A. P., Titley, S. R., and Pimentel, F. B., 2001, Geology of the Escondida porphyry copper deposit, Antofagasta region, Chile, Economic Geology, v. 96, p. 307-324.

Goddard, J. V. and Evans, J. P., 1995, Chemical and fluid-rock interaction in faults of crystalline thrust sheets, northwestern Wyoming, U.S.A., Journal of Structural Geology, v. 17, p. 533-547.

Grant, J.A., 1986, The Isocon Diagram- A simple solution to Gresen's equation for metasomatic alteration, Economic Geology, v. 81, p. 1976-1982.

Gresens, R. L., 1967, Composition- volume relations in metasomatism, Chemical Geology, v. 2, p. 47-65.

Gustafson, L.B., and Hunt, J.P., 1975, The porphyry copper deposit at El Salvador, Chile: Economic Geology, v. 70, p. 857-912.

Harlov, D., Tropper, P., Seifert, W., Nijland, T., Förster, H. J., 2006, Formation of Al-rich titanite ($CaTiSiO_4O$–$CaAlSiO_4OH$) reaction rims on ilmenite in metamorphic rocks as a function of fH_2O and fO_2, Lithos, v. 88, p. 72-84.

Hart, C., 2008, The geological framework of the Yukon Territory, Yukon Geological Survey, www.geology.gov.yk.ca/geology_metallogeny, p. 1-11.

Hayden, L. A., Watson, E. B., and Wark, D. A., 2008, A thermobarometer for sphene (titanite), Contrib Mineral Petrol, v. 155, p. 529-540.

Hey, M. H., 1954, A new review of the chlorites, Mineralogical Magazine, v. 30, p. 277-292.

Horie, K., Hidaka, H., and Gauthier-Lafaye, F., 2008, Elemental distribution in apatite, titanite and zircon during hydrothermal alteration: Durability of immobilization mineral phases for actinides, Physics and Chemistry of the Earth, v. 33, p. 962–968.

Hoskin, P.W.O., and Schaltegger, U., 2003, The composition of zircon and igneous and metamorphic petrogenesis, In Hanchar, J.M. and Hoskin, P.W.O. (eds.) Zircon, Reviews in Mineralogy and Geochemistry, Mineralogical Society of America, v. 53, p. 27-62.

Irvine, T. N., and Baragar, W. R. A., 1971, A guide to the chemical classification of the common volcanic rocks, Canadian Journal of Earth Sciences, v. 8, p. 523-548.

Johnston, S. T., 1993, The geologic evolution of Nisling Assemblage and Stikine terrane in the Aishihik Lake area, Southwest Yukon, PhD thesis, University of Alberta.

99

Johnston, S. T., and Canil, D., 2007, Crustal architecture of SW Yukon, northern Cordillera: Implications for crustal growth in a convergent margin orogen, Tectonics, v. 26, TC1006.

Johnston, S.T., and Erdmer, P., 1995, Hot-side-up aureole in the southwest Yukon and limits on terrane assembly of the northern Canadian cordillera, Geology, v. 23, p. 419-422.

Johnston, S.T., Mortensen, J. K., and Erdmer, P., 1996: Igneous and metaigneous age constraints for the Ashihik metamorphic suite, Southwest Yukon, Canadian Journal of Earth Sciences, v. 33, p. 1543-1555.

Johnston, S.T., and Timmerman, J. R., 1994: Geology of the Aishihik Lake and Hopkins Lake areas (115H/6,7), southwest Yukon. In: Yukon Exploration and Geology, 1993. Exploration and Geological Services Division, Yukon, Indian and Northern Affairs, Canada, p. 93-110.

Johnston, S.T., and Timmerman, J. R., 1997: Geology of Hopkins Lake map area, Yukon (NTS 115H/7), Exploration Services Division, Yukon, Indian and Northern Affairs, Canada, Geoscience map.

Kamber, B. S., and Ulrich, T., 2009, Report on U/Pb zircon and titanite geochronology of samples HB076, HB140 and HB226a, Laurentian University, unpublished document.

Kranidiotis, P., Maclean, W. H., 1987, Systematics of chlorite alteration at the Phelps Dodge massive sulfide deposit, Matagami, Quebec, Economic Geology, v. 82, p. 1898-1911.

Lanier, G., Raab, W. J., Folsom, R. B., and Cone, S., 1978, Alteration of equigranular monzonite, Bingham mining district, Utah, Economic Geology, v. 73, p. 1270-1286.

Leake, B. E., 1978, Nomenclature of amphiboles, American Mineralogist, v. 63, p. 1023-1052.

Lesher, C.M., Gibson, H.L., and Campbell, I. H., 1986, Composition-volume changes during hydrothermal alteration of andesite at Buttercup Hill, Noranda District, Quebec: Geochimica et Cosmochimica Acta, v. 50, p. 2693-2705.

Li, J. W., Deng, X. D., Zhou, M. F., Liu, Y. S., Zhao, X. F., and Guo, J. L., 2010, Laser ablation ICP-MS titanite U–Th–Pb dating of hydrothermal ore deposits: A case study of the Tonglushan Cu–Fe–Au skarn deposit, SE Hubei Province, China, Chemical Geology, v. 270, p. 56-67.

Love, D. A. and Roberts, R. G., 1991, The geology and geochemistry of gold mineralization and associated alteration at the rundle gold deposit, Abitibi Subprovince, Ontario, Economic Geology, v. 86, p. 644-666.

Mazdab, F.K., Wooden, J.L., and Barth, A.P., 2007, Trace-element variability in titanite from diverse geologic environments, Geological Society of America, Abstracts with Programs, v. 39, p. 406.

Mezger, J.E., 1997, Tectonomorphic evolution of the Kluane Metamorphic Assemblage, SW Yukon: evidence for late Cretaceous eastward subduction of oceanic crust underneath north America, PhD thesis, University of Alberta.

Mortensen, J. K., 1992, Pre-mid Mesozoic tectonic evolution of the Yukon-Tanana terrane, Yukon and Alaska, Tectonics, v. 11, p. 836-853.

Munoz, J. L., 1984, F-OH and Cl-OH exchange in micas with applications to hydrothermal ore deposits, In: Bailey, S. W. (Ed.), Micas, Rev. Mineral., v. 13, p. 469-494.

Ohmoto, H. and Rye, R.O. 1996, Geochemistry of Hydrothermal Ore Deposits. 2nd Edition, H.L. Barnes, Ed., Elsevier, p. 21-23.

Panigrahi, M. K., Naik, R. K., Pandit, D., and Misra K. C., 2008, Reconstructing physico-chemical parameters of hydrothermal mineralization of copper at the Malanjkhand deposit, India, from mineral chemistry of biotite, chlorite and epidote, Geochemical Journal, v. 42, p. 443- 460.

Parry, W. T. and Downey, L. M., 1982, Geochemistry of hydrothermal chlorite replacing igneous biotite, Clays and Clay Minerals, v. 30, no. 2, p. 81-90.

Piccoli, P., Candela, P., and Rivers, M., 2000, Interpreting magmatic processes from accessory phases: titanite- a small-scale recorder of large-scale process, Geological Society of America, v. 350, p. 257-267.

Selby, D. and Nesbitt, B. E., 1998, Biotite chemistry of the Casino Porphyry Cu-Mo-Au occurrence, Dawson Range, Yukon, In: Yukon Exploration and Geology, 1997, Exploration and Geological Services Division, Yukon, Indian And Northern Affairs Canada, p. 83-88.

Selby, D., and Nesbitt B. E., 2000, Chemical composition of biotite from the Casino porphyry Cu–Au–Mo mineralization, Yukon, Canada: evaluation of magmatic and hydrothermal fluid chemistry, Chemical Geology, v. 171, p. 77–93.

Sillitoe, R.H., 1972, A plate tectonic model for the origin of porphyry copper deposits: Economic Geology, v. 67, p. 184-197.

Smith, H., 2007: Assessment report describing prospecting, geological mapping and soil geochemistry at the Hopper property, Assessment report, Archer Cathro and Associates, p. 1-8.

Stern, C. R., Funk, J. A., Skewes, M. A., and Arévalo, A., 2007, Magmatic anhydrite in plutonic rocks at the El Teniente Cu-Mo depost, Chile, and the role of sulfur- and copper-rich magmas in its formation, Economic Geology, v. 102, p. 1335-1344.

Streckeisen, A. L., 1973, Plutonic rocks, classification and nomenclature recommended by the IUGS subcommission on the systematic of igneous rocks, Geotimes, v. 18, p. 26-30.

Sun, S. S., and McDonough, W. F., 1989, Chemical and isotopic systematic of oceanic basalts: Implications for mantle composition and processes, In: Saunders, A. D., and Nory M. J. (eds), Magmatism in the ocean basins, Geological Society of London, Spec. Pub, v. 42, p. 313-345.

Tafti, R., and Mortensen, J.K., 2004, Early Jurassic porphyry(?) copper(-gold) deposits at Minto and Williams Creek, Carmacks copper belt, western Yukon, In: Emond, D.S. and Lewis, L.L., eds., Yukon Exploration and Geology 2003: Yukon Geological Survey, p. 289-303.

Tempelman-Kluit, D. J., 1981, Geology and mineral deposits of southern Yukon, In: Yukon Geology and Exploration 1979-80, Exploration and Geological Services Division, Yukon, Indian and Northern Affairs Canada, p. 7-31.

Tindle, A. G., 1993, Chlorite formula unit calculator and variety namer Excel spreadsheet, the Open University, United Kingdom, unpublished document.

Tropper, P., Manning, C. E., and Essene, E. J., 2002, The substitution of Al and F in titanite at high pressure and temperature: Experimental constraints on phase relations and solid solution properties, v. 43, p. 1787-1814.

Ulrich, T., and Heinrich C. A., 2001, Geology and alteration geochemistry of the porphyry Cu- Au deposit at Bajo de la Alumbrera, Argentina, Economic Geology, v. 96, p. 1719-1742.

Walshe, J. L., 1986, A six-component chlorite solid solution model and the conditions of chlorite formation in hydrothermal and geothermal systems, Economic Geology, v. 81, p. 681-703.

Wheeler, J. O., and McFeely, P., 1991, Tectonic assemblages map of the Canadian Cordillera, Geological Survey of Canada Map 1712A, 1:2,000,000 scale with legend.

Zaluski, G., Nesbitt, B., and Muehlenbachs, K., 1994, Hydrothermal alteration and stable isotope systematics of the Babine porphyry Cu deposits, British Columbia: Implications for fluid evolution of porphyry systems, Economic Geology, v. 89, p. 1518-1541.

          ,2007, Copper, Government of Yukon, Departments of Economic Development & Energy, Mines and Resources, www.geology.gov.yk.ca.

Appendix A
Sample Descriptions

Samples from Hopper and Janisiw properties: Analyses summary

Samples:	UTM Zone 8, NAD 83		Rock Type	Analyses												
	Eastings	Northings		XRF	IMC	EPMA					LA-ICP-MS	Kfs staining	S isotopes	SEM	Age dating
						Pl	Am	Bt	Chl	Ttn	Ttn				
HB008	397591	6798147										X			
HB009	397486	6798208										X			
HB010	397486	6798208										X			
HB013	397433	6798276										X			
HB015	397396	6798113										X			
HB017	397452	6798025										X			
HB029	397230	6797349										X			
HB030A	397148	6797423													
HB030B	397148	6797423										X			
HB032	397114	6797481										X			
HB035	397082	6797549										X			
HB036	397070	6797570													
HB036B	397070	6797570										X			
HB037	397064	6797584										X			
HB043A	397034	6797419	Metasediments									X			
HB043B	397034	6797419										X			
HB101	397033	6797441										X			
HB102	397033	6797441										X			
HB109	397011	6797355										X			
HB122	397642	6797889										X			
HB124	397622	6797968										X			
HB125	397636	6797968										X			
HB126	397632	6797980										X			
HB128	397695	6798503										X			
HB163	397415	6798084										X			
HB169	397450	6797810										X			
HB201	397117	6798078										X			
HB210	396372	6797491										X			
HB211B	396426	6797461										X			

Samples:	UTM Zone 8, NAD 83		Rock Type	Analyses												
	Eastings	Northings		XRF	IMC	EPMA					LA-ICP-MS	Kfs staining	S isotopes	SEM	Age dating
						Pl	Am	Bt	Chl	Ttn	Ttn				
HB001	397622	6797853										X			
HB018	397447	6798005		X	X							X			
HB018B	397447	6798005										X			
HB019	397461	6797957										X			
020	397658	6797071										X			
HB024	399706	6796777										X			
HB025	399711	6796745										X			
HB065	396747	6796961		X	X							X			
HB069	396841	6796752										X			
HB072	397348	6796107		X	X	X	X	X				X			
HB073	397610	6796295		X	X							X			
HB075	397588	6797243										X			
HB076	397660	6797263							X	X	X	X	X	X	X
HB081	397675	6797268		X	X				X	X	X	X			
HB082	397678	6797271									X	X			
HB083A	397678	6797271	Granodiorite						X			X			
HB084	397684	6797273								X		X			
HB085	397688	6797273										X			
HB086	397701	6797254		X	X							X			
HB088	397646	6797195										X			
HB090	397714	6797249		X	X	X	X	X				X			
HB090A	397714	6797249										X			
HB094	397742	6797235							X			X			
HB098A	397770	6797220		X	X				X		X	X			
HB098C	397770	6797220										X			
HB100	398040	6797255								X		X			
HB104	397040	6797391		X	X				X			X			
HB106	397062	6797361										X			
HB113	396904	6797366								X	X	X		X	
HB115	397100	6797333								X		X			
HB116A	397133	6797335										X		X	
HB116B	397133	6797335										X		X	

Samples from Hopper and Janisiw properties: Analyses summary (continued…)

Samples:	UTM Zone 8, NAD 83		Rock Type	Analyses											
	Eastings	Northings		XRF	IMC	EPMA					LA-ICP-MS	Kfs staining	S isotopes	SEM	Age dating
						Pl	Am	Bt	Chl	Ttn	Ttn				
HB119	397249	6797222		X	X				X	X	X	X		X	
HB120	397253	6797229								X	X	X			
HB127	397705	6797987										X			
HB134	398022	6798324										X			
HB136	397852	6798028		X	X				X			X			
HB137	397820	6797918		X	X					X	X	X			
HB139	397691	6797273										X			
HB140	397692	6797270							X	X	X	X			X
HB141B	397696	6797262										X			
HB142	397722	6797248										X			
HB143	397727	6797246										X			
HB145	397734	6797240							X			X			
HB145B	397734	6797240										X			
HB147	397746	6797234										X			
HB148	397750	6797230										X			
HB149	397753	6797230		X	X							X			
HB151A-1	397756	6797230		X	X				X	X					
HB151A-2	397756	6797230	Granodiorite												
HB151B	397756	6797230										X			
HB153	397778	6797215										X			
HB154	397778	6797213									X	X		X	
HB155	397838	6797178		X	X					X		X			
HB157	397612	6797818										X			
HB159	397539	6797867										X			
HB162	397481	6797992		X	X	X						X			
HB172	397437	6797709										X			
HB173	397433	6797586										X			
HB175	397440	6797523										X			
HB176	397589	6797747										X			
HB177	398025	6797542								X		X			
HB178	398049	6797468		X	X	X						X			
HB179	398050	6797340		X	X							X			
HB180	397810	6797038		X	X							X			
HB181	397785	6797040								X	X	X			
HB182	397689	6797005		X	X		X					X			
HB183	397672	6797084							X	X	X	X			
HB184	397661	6796877		X	X		X	X				X			

Samples from Hopper and Janisiw properties: Analyses summary (continued…)

Samples:	Eastings	Northings	Rock Type	XRF	IMC	Pl	Am	Bt	Chl	Ttn	Ttn (LA-ICP-MS)	Kfs staining	S isotopes	SEM	Age dating
	UTM Zone 8, NAD 83			Analyses		EPMA					LA-ICP-MS				
HB187	397681	6796546										X			
HB189	397596	6796399					X					X		X	
HB192	398036	6795920		X	X		X	X				X			
HB193	398048	6795276										X			
HB205	396551	6798024										X			
HB212	396462	6797411		X	X							X			
HB216	396698	6797218		X	X		X	X				X			
HB217	396717	6797184		X	X							X			
HB218A	398375	6797543								X	X	X			
HB218B	398375	6797543										X			
HB219	398688	6797545										X			
HB220	398997	6797528		X	X							X			
HB221	400070	6797653	Granodiorite									X			
HB222	400350	6797577		X	X	X						X			
HB223	400340	6797107										X			
HB224	398094	6797169										X			
HB227	397620	6797869										X			
HB228	397635	6797722		X	X				X	X		X			
HB229	397690	6797673										X			
HB230B	397685	6797596										X			
HB231A	397532	6797203										X			
HB231B	397532	6797203		X	X					X		X			
HB232	397446	6797199										X			
HB233	397522	6797136		X	X	X						X			
HB236	397436	6797547										X			
HB044	400466	6796131		X	X	X		X				X			
HB045	400544	6795905		X	X	X		X				X			
HB046	400202	6795350	Diorite									X			
HB047	400312	6796049		X	X	X		X				X			
HB048	400327	6796524		X	X							X			
HB049	401878	6796534		X	X	X		X				X			

Samples from Hopper and Janisiw properties: Analyses summary (continued…)

Samples:	UTM Zone 8, NAD 83		Rock Type	Analyses											
	Eastings	Northings		XRF	IMC	EPMA					LA-ICP-MS	Kfs staining	S isotopes	SEM	Age dating
						Pl	Am	Bt	Chl	Ttn	Ttn				
HB012	397433	6798199	QFP Dyke	X	X				X			X			
HB026	398708	6797217							X	X		X			
HB070	396882	6796691								X	X	X			
HB090B	397714	6797249										X			
HB110	396993	6797312										X			
HB130	397716	6798738							X			X			
HB132	397718	6798636										X			
HB164	397476	6797875		X	X							X			
HB164B	397476	6797875										X			
HB167	397472	6797859										X			
HB170	397449	6797779										X			
HB225	398053	6797174										X			
HB080	397675	6797268	Aplite Dyke									X			
HB089	397708	6797247										X		X	
HB144A	397742	6797238										X		X	
HB144B	397742	6797238										X			
HB230A	397685	6797596										X			
HB230C	397685	6797596										X			
HB230D	397685	6797596										X			
HB152	397762	6797225	Vein									X	X		

Appendix B
Age Dating Report

This appendix includes a pdf file of an age dating report by Kamber and Ulrich (2009), and excel files containing raw data of zircon and titanite analyses using Laser Ablation Inductively Coupled Plasma Mass Spectrometer.

The file names are: Age Dating Report.pdf, Titanite raw data_Kamber and Ulrich 2009.xlsx, and Zircon age dating_Kamber and Ulrich 2009.xlsx.

If you accessed this thesis from a source other than the University of Waterloo, you may not have access to this file. You may access it by contacting the author at vhblumen@sciborg.uwaterloo.ca.

Appendix C
Alteration Summary

This is an excel file containing a summary of the alteration based on petrography.

The file name is: Alteration summary based on petrography.xlsx.

If you accessed this thesis from a source other than the University of Waterloo, you may not have access to this file. You may access it by contacting the author at vhblumen@sciborg.uwaterloo.ca.

Appendix D
Specific Gravity

This is an excel file containing specific gravity raw data.

The file name is: Specific gravity.xlsx.

If you accessed this thesis from a source other than the University of Waterloo, you may not have access to this file. You may access it by contacting the author at vhblumen@sciborg.uwaterloo.ca.

Appendix E
Whole Rock Geochemistry

This is an excel file containing whole rock geochemistry raw data.

The file name is: Whole rock geochemistry.xlsx.

If you accessed this thesis from a source other than the University of Waterloo, you may not have access to this file. You may access it by contacting the author at vhblumen@sciborg.uwaterloo.ca.

Appendix F
Mass Balance Calculations

This appendix contains excel files of mass balance calculations data based on Grant's and Gresens' methods.

The file names are: Mass balance calculations_Grant method.xlsx and Mass balance calculations_Gresens method.xlsx.

If you accessed this thesis from a source other than the University of Waterloo, you may not have access to this file. You may access it by contacting the author at vhblumen@sciborg.uwaterloo.ca.

Appendix G
Electron Microprobe Results

This appendix contains excel files of electron microprobe analyses raw data of amphiboles, biotites, chlorites, plagioclase and titanites.

The file names are:

Amphibole analyses with EPMA.xlsx

Biotite analyses with EPMA.xlsx

Chlorite analyses with EPMA.xlsx

Plagioclase analyses with EPMA.xlsx

Titanite analyses with EPMA.xlsx

If you accessed this thesis from a source other than the University of Waterloo, you may not have access to this file. You may access it by contacting the author at vhblumen@sciborg.uwaterloo.ca.

Appendix H

Laser Ablation Inductively Coupled Plasma Mass Spectrometer Results

This appendix is an excel file of Laser ablation inductively coupled plasma mass spectrometer analyses raw data of titanites.

The file name is: Titanite analyses with LA ICP MS.xlsx.

If you accessed this thesis from a source other than the University of Waterloo, you may not have access to this file. You may access it by contacting the author at vhblumen@sciborg.uwaterloo.ca.

Appendix I

Scanning Electron Microscope Imaging and Analytical Results

This appendix contains JPEG and TIF files of images and analyses of hydrothermal and magmatic titanites using a scanning electron microscope.

The file names are:

HB_076_5_hydrothermal titanite_using Cl_not showing zoning.tif

HB_113_1_hydrothermal titanite_using BSE_patchy zoning.tif

HB113_3_magmatic titanite analyzed with BSE.jpg

HB_113_3_magmatic titanite_using BSE_patchy zoning.tif

HB113_4_hydrothermal titanite analyzed with BSE.jpg

HB_113_4_hydrothermal titanite_using BSE_patchy zoining.tif

HB113_5_magmatic titanite analyzed with BSE.jpg

HB_113_5_magmatic titanite_using BSE_oscillatory zoning.tif

HB113_6_hydrothermal titanite analyzed with BSE.jpg

HB_113_6_hydrothermal titanite_using BSE_patchy zoning.tif

HB117_3_magmatic titanite with patchy zoning_using BSE.tif

HB_119_4b_magmatic titantie_using Cl_not showing zoning.tif

HB_119_4c_magmatic titanite_using Cl_not showing zoning.tif

HB_119_4_magmatic titanite_using Cl_not showing zoning.tif

HB154_3_magmatic titanite analyzed with BSE.jpg

HB_154_3_magmatic titanite_using BSE_patchy zoning.tif

HB154_5_magmatic titanite analyzed with BSE.jpg

HB_154_5_magmatic titanite_using BSE_patchy zoning.tif

HB189_1_magmatic titanite analyzed with BSE.jpg

HB_189_1_magmatic titanite_using BSE_patchy zoning.tif

HB189_3_magmatic titanite analyzed with BSE.jpg

HB_189_3_magmatic titanite_using BSE_patchy zoning.tif

HB189_4_magmatic titanite analyzed with BSE.jpg

HB_189_4_magmatic titanite_using BSE_patchy zoning.tif

If you accessed this thesis from a source other than the University of Waterloo, you may not have access to this file. You may access it by contacting the author at vhblumen@sciborg.uwaterloo.ca.

Appendix J

Slab Photographs of Samples with Stained K-Feldspar

This appendix contains JPEG files of photographs of samples with stained K-Feldspar.

The file names are:

020.JPG	HB043B.JPG	HB089.JPG	HB126.JPG	HB159.JPG	HB201.JPG	HB232.JPG
HB001.JPG	HB044.JPG	HB090A.JPG	HB127.JPG	HB162.JPG	HB205.JPG	HB233.JPG
HB002.JPG	HB045.JPG	HB090B.JPG	HB128.JPG	HB163.JPG	HB210.JPG	HB234.JPG
HB003.JPG	HB046.JPG	Hb090.JPG	HB130.JPG	HB164B.JPG	HB211B.JPG	HB236.JPG
HB008.JPG	HB047.JPG	HB094.JPG	HB132.JPG	HB164.JPG	HB211.JPG	
HB009.JPG	HB048.JPG	HB098A.JPG	HB134.JPG	HB167.JPG	HB212.JPG	
HB010.JPG	HB049.JPG	HB098C.JPG	HB136.JPG	HB169.JPG	HB216.JPG	
HB011.JPG	HB055.JPG	HB100.JPG	HB137.JPG	HB170.JPG	HB217.JPG	
HB012.JPG	HB065.JPG	HB101.JPG	HB139.JPG	HB172.JPG	HB218A.JPG	
HB013.JPG	HB069.JPG	HB102.JPG	HB140.JPG	HB173.JPG	HB218B.JPG	
HB015.JPG	HB070.JPG	HB104.JPG	HB141B.JPG	HB175.JPG	HB219.JPG	
HB017.JPG	HB072.JPG	HB106.JPG	HB142.JPG	HB176.JPG	HB220.JPG	
HB018B.JPG	HB073.JPG	HB107A.JPG	HB143.JPG	HB177.JPG	HB 221.JPG	
HB018.JPG	HB075.JPG	HB107.JPG	HB144A.JPG	HB178.JPG	HB222.JPG	
HB019.JPG	HB076.JPG	HB109.JPG	HB144B.JPG	HB179.JPG	HB223.JPG	
HB024.JPG	HB078.JPG	HB110.JPG	HB145B.JPG	HB180.JPG	HB224.JPG	
HB025.JPG	HB079.JPG	HB113.JPG	HB145.JPG	HB181.JPG	HB225.JPG	
HB026.JPG	HB080.JPG	HB115.JPG	HB147.JPG	HB182.JPG	HB227.JPG	
HB027B.JPG	HB081.JPG	HB116A.JPG	HB148.JPG	HB183.JPG	HB228.JPG	
HB027.JPG	HB082.JPG	HB116B.JPG	HB149.JPG	HB184.JPG	HB229.JPG	
HB029.JPG	HB083A.JPG	HB117.JPG	HB151B.JPG	HB186.JPG	HB230A.JPG	
HB030B.JPG	HB084.JPG	HB119.JPG	HB152.JPG	HB189.JPG	HB230B.JPG	
HB032.JPG	HB085.JPG	HB120.JPG	HB153.JPG	HB192.JPG	HB230C.JPG	
HB036B.JPG	HB086.JPG	HB122.JPG	HB154.JPG	HB193.JPG	HB230D.JPG	
HB037.JPG	HB087.JPG	HB124.JPG	HB155.JPG	HB194.JPG	HB231A.JPG	
HB043A.JPG	HB088.JPG	HB125.JPG	HB157.JPG	HB196.JPG	HB231B.JPG	

If you accessed this thesis from a source other than the University of Waterloo, you may not have access to this file. You may access it by contacting the author at vhblumen@sciborg.uwaterloo.ca.